

2009

Dynamic Contrast Enhanced Computed Tomography Measurement of Perfusion in Hepatic Cancer

Errol E. Stewart

Follow this and additional works at: <https://ir.lib.uwo.ca/digitizedtheses>

Recommended Citation

Stewart, Errol E., "Dynamic Contrast Enhanced Computed Tomography Measurement of Perfusion in Hepatic Cancer" (2009). *Digitized Theses*. 3943.
<https://ir.lib.uwo.ca/digitizedtheses/3943>

This Thesis is brought to you for free and open access by the Digitized Special Collections at Scholarship@Western. It has been accepted for inclusion in Digitized Theses by an authorized administrator of Scholarship@Western. For more information, please contact wlsadmin@uwo.ca.

Dynamic Contrast Enhanced Computed Tomography Measurement of Perfusion in
Hepatic Cancer

(Spine title: CT measurement of hepatic perfusion)

(Thesis format: Integrated-Articles)

By

Errol E. Stewart

Graduate Program
in
Medical Biophysics

A thesis submitted in partial fulfillment
of the requirement for the degree of
Doctor of Philosophy

Dynamic Contrast Enhanced Computed Tomography Measurement of Perfusion in
Hepatic Cancer

(Spine title: CT measurement of hepatic perfusion)

(Thesis format: Integrated-Articles)

By

Errol E. Stewart

Graduate Program
in
Medical Biophysics

A thesis submitted in partial fulfillment
of the requirement for the degree of
Doctor of Philosophy

The School of Graduate and Postdoctoral Studies
the University of Western Ontario
London, Ontario, Canada
October 15, 2009

© Errol E. Stewart 2009

ABSTRACT

In recent years, the incidence and mortality rate for hepatocellular carcinoma (HCC) have increased due to the emergence of hepatitis B, C and other diseases that cause cirrhosis. The progression from cirrhosis to HCC is characterized by abnormal vascularization and by a shift from a venous to an arterial blood supply. A knowledge of HCC vascularity which is manifested as alterations in liver blood flow may distinguish among different stages of liver disease and can be used to monitor response to treatment. Unfortunately, conventional diagnostic imaging techniques lack the ability to accurately quantify HCC vascularity. The purpose of this thesis was to validate and assess the diagnostic capabilities of dynamic contrast enhanced computed tomography (DCE-CT) and perfusion software designed to measure hepatic perfusion.

Chapter 2 described a study designed to evaluate the accuracy and precision of hepatic perfusion measurement. The results showed a strong correlation between hepatic artery blood flow measurement with DCE-CT and radioactive microspheres under steady state in a rabbit model for HCC (VX2 carcinoma). Using repeated measurements and Monte Carlo simulations, DCE-CT perfusion measurements were found to be precise; with the highest precision in the tumor rim.

In Chapter 3, we used fluorine-18 fluoro-2-deoxy-D-glucose (FDG) positron emission tomography and DCE-CT perfusion to determine an inverse correlation between glucose utilization and tumor blood flow; with an R^2 of 0.727 ($P < 0.05$). This suggests a limited supply of oxygen (possibly hypoxia) and that the tumor cells were surviving via anaerobic glycolysis.

In Chapter 4, hepatic perfusion data showed that thalidomide caused a reduction of tumor perfusion in the responder group during the first 8 days after therapy, $P < 0.05$; while perfusion in the partial responder and control group remained unchanged, $P > 0.05$. These changes were attributed to vascular remodeling and maturation resulting in a more functional network of endothelial tubes lined with pericytes.

The results of this thesis demonstrate the accuracy and precision of DCE-CT hepatic perfusion measurements. It also showed that DCE-CT perfusion has the potential to enhance the functional imaging ability of hybrid PET/CT scanners and evaluate the efficacy of anti-angiogenesis therapy.

Keywords: Hepatocellular carcinoma, hepatic blood flow, angiogenesis, thalidomide, dynamic contrast enhanced computed tomography, positron emission tomography, fluorine-18 fluoro-2-deoxy-D-glucose, imaging, CT Perfusion

vascular normalization”, which was submitted for publication to the journal *Clinical Cancer Research* in October 2009 by Errol E. Stewart, Hongtao Sun, Peter Schafer, Yong Chen, Bertha Garcia, Ting-Yim Lee. I was responsible for designing the study, performing the experiments, collecting and analyzing the data and writing the manuscript. Ting-Yim Lee assisted with the design of this study, provided supervision throughout the project and reviewed the manuscript. Hongtao Sun and Bertha Garcia assisted in the histological analysis. Peter Schafer and Yong Chen were responsible for thalidomide blood concentration analysis.

ACKNOWLEDGEMENTS

This thesis could not have been accomplished without the efforts and support from many individuals. First, I would like to thank my thesis supervisor, Dr. Ting-Yim Lee. His dedication to research and his ability to foster independent thinking made my graduate work one of the most rewarding experience of my life. Ting's favorite quotes are "don't put the cart before the horse" and "can't see the forest for the trees". Simple quotes, but they speak volumes about answering tough questions one piece at a time, while at the same time recognizing the impact of your research. His enthusiasm for teaching and learning is infectious and I know these lessons will stay with me for a life time.

I would also like to thank my advisory committee members Dr Keith St. Lawrence and Dr Terry Thompson. Special thanks to Jennifer Hadway, who made my life and work so much easier by being so dedicated to her work. Without her and her willingness to sacrifice her weekends and time away from her family none of this work would be successful. Additionally, I would like to thank Claire Poppe and Dominique Ouimet for their assistance with the animal experiments. I would also like to thank Kelly Galloway-Kay for her assistance with the histological studies.

Additionally, I would like to thank the other members of Ting's research group past and present especially Anne Leaist for their assistance, friendship and support over the years. I would like to thank Dr. Xiaogang Chen for programming the software used to analysis the DCE-CT data and for always willing to implement some of my unconventional design ideas.

Finally, I would like to thank my family and my girlfriend Jia 'Clara' Jun for always believing in me even when the way ahead was not so clear.

TABLE OF CONTENTS

Certificate of Examination	ii
Abstract.....	iii
Co-Authorship.....	v
Acknowledgements	vii
Table of Contents	ix
List of Tables	xiv
List of Figures and Illustrations	xv
List of Appendices.....	xvi
List of Symbols, Abbreviations and Nomenclatures.....	xvii
1. CHAPTER 1: INTRODUCTION.....	1
1.1 LIVER CANCER.....	1
1.2 ETIOLOGY OF MALIGNANT PRIMARY LIVER CANCER.....	2
1.3 HEPATOCELLULAR CARCINOMA (HCC).....	3
1.3.1 Cirrhosis.....	3
1.3.2 Hepatocarcinogenesis	5
1.4 TUMOR ANGIOGENESIS.....	8
1.4.1 Hypoxia and the Angiogenic Switch	9
1.4.2 Sprouting Angiogenesis.....	10
1.4.3 Intussusceptive Microvascular Growth (IMG)	13
1.5 SCREENING FOR HCC	15
1.6 IMAGING EVALUATION OF HCC	15
1.6.1 Ultrasound.....	16
1.6.2 Magnetic Resonance (MR) Imaging.....	18
1.6.3 Computed Tomography (CT)	21
1.6.4 Positron Emission Tomography (PET).....	23

1.7	TREATMENT OF HEPATIC TUMORS.....	25
1.8	ADVANCE FUNCTIONAL IMAGING.....	28
1.8.1	Tracer Kinetic Model Selection.....	28
1.8.2	Measuring Blood Flow Using the Johnson and Wilson Model.....	30
1.8.3	Measuring Hepatic Blood Flow.....	31
1.9	RESEARCH GOAL AND OBJECTIVES.....	33
1.10	THESIS OUTLINE.....	34
1.10.1	Validation of Dynamic Contrast Enhance Computed Tomography Measurement of Hepatic Perfusion (<i>Chapter 2</i>).....	34
1.10.2	Assessment of the Relationship between Hepatic Tumor Blood Flow and Glucose Utilization using <i>in vivo</i> PET/CT (<i>Chapter 3</i>).....	34
1.10.3	Investigating the Effect of Thalidomide on Hepatic Perfusion and Vascular Remodeling (<i>Chapter 4</i>).....	35
1.10.4	Conclusion and Future Work (<i>Chapter 5</i>).....	35
1.11	REFERENCES.....	36
2	CHAPTER 2: HEPATIC PERFUSION IN A TUMOR MODEL USING DCE- CT: A ACCURACY AND PRECISION STUDY.....	51
2.1	INTRODUCTION.....	51
2.2	MATERIALS AND METHODS.....	53
2.2.1	Study Protocol.....	53
2.2.2	Surgical Preparation.....	53
2.2.3	DCE-CT Scanning Protocol.....	54
2.2.4	Precision Study.....	55
2.2.5	Calculation of Parametric Maps.....	55
2.2.6	Accuracy Study.....	58
2.2.7	Data Analysis.....	59
2.2.8	Monte Carlo Simulation.....	60

2.2.9	Statistical Analysis.....	60
2.3	RESULTS	61
2.4	DISCUSSION	73
2.5	REFERENCES	80
3	CHAPTER 3: CORRELATION BETWEEN HEPATIC TUMOR BLOOD FLOW AND GLUCOSE UTILIZATION IN A RABBIT LIVER TUMOR MODEL	84
3.1	INTRODUCTION	84
3.2	MATERIALS AND METHODS.....	86
3.2.1	Study Protocol.....	86
3.2.2	DCE-CT Scanning Protocol.....	87
3.2.3	[¹⁸ F] FDG-PET Acquisition and Image Reconstruction.....	88
3.2.4	Functional Parameters Calculation	89
3.2.5	Data Analysis.....	90
3.2.6	Statistical Analysis.....	91
3.3	RESULTS	91
3.3.1	Hepatic Blood Flow and Volume	95
3.3.2	Permeability Surface-Area Product and Hepatic Arterial Fraction	98
3.3.3	Glucose uptake vs. Hepatic Blood Flow.....	100
3.4	DISCUSSION	104
3.5	REFERENCES	109
4	CHAPTER 4: DCE-CT PERFUSION IDENTIFY DIFFERENTIAL HEPATIC BLOOD FLOW RESPONSE DURING THALIDOMIDE INDUCED TUMOR VASCULAR NORMALIZATION.....	112

4.1	INTRODUCTION	112
4.2	MATERIALS AND METHOD	114
4.2.1	Animal Model	114
4.2.2	Treatment Protocol.....	115
4.2.3	CT Scanning Protocol.....	115
4.2.4	Immunohistochemical Staining	116
4.2.5	Data Analysis.....	117
4.2.6	Statistical Analysis.....	120
4.3	RESULTS	120
4.4	DISCUSSION	129
4.5	ACKNOWLEDGEMENT	134
4.6	REFERENCE.....	135
5.	CHAPTER 5: CONCLUSION.....	139
5.1	THESIS OVERVIEW.....	139
5.2	VALIDATION OF DYNAMIC CONTRAST ENHANCED COMPUTED TOMOGRAPHY MEASUREMENT OF HEPATIC PERFUSION	140
5.3	RELATIONSHIP BETWEEN HEPATIC TUMOR BLOOD FLOW AND GLUCOSE UTILIZATION.....	141
5.4	THE EFFECT OF THALIDOMIDE ON HEPATIC PERFUSION AND VASCULAR REMODELING.....	142
5.5	EXPERIMENTAL AND CLINICAL RELEVANCE.....	143
5.5.1	Experimental Relevance of VX2 Carcinoma as a Model for Hepatocellular Carcinoma	143
5.5.2	Limitations of the VX2 Carcinoma Model	144

5.5.3	Clinical Relevance of Dynamic Contrast Enhanced Computed Tomography Perfusion.....	146
5.6	FUTURE WORK.....	147
5.6.1	Optimizing Angiogenesis Inhibitor Therapy and Adjuvant Radiotherapy	147
5.6.2	Evaluating Radiation Therapy of Hepatocellular Carcinoma.....	148
5.6.3	Relationship between Hepatic Arterial Blood Flow and Glucose Utilization	150
5.7	REFERENCES	152
A.	APPENDIX A.....	155
B.	APPENDIX B.....	156
B.1	TRACER KINETIC MODELING	156
B.2	REFERENCES	159
	Curriculum Vitae.....	160

LIST OF TABLES

Table 2.1: Physiological parameters at different capnic levels	62
Table 2.2: Hepatic perfusion measured with DCE-CT and microsphere under three capnic levels in the normal tissue	64
Table 2.3: The coefficient of variation for all the functional parameters	67
Table 2.4: GEE and Bland-Altman analysis between the first and second measurement for each functional parameter.	69

LIST OF FIGURES AND ILLUSTRATIONS

Figure 1.1: Sprouting Angiogenesis	11
Figure 1.2: Basal-luminal polarity	12
Figure 1.3: Intussuceptive Microvascular Growth.....	14
Figure 2.1: Time enhancement curves and IRF	56
Figure 2.2: Perfusion Weighted Map.....	58
Figure 2.3: DCE-CT perfusion maps	63
Figure 2.4: Precision of DCE-CT perfusion measurement.....	68
Figure 2.5: Monte Carlo Simulation	70
Figure 2.6: Validation of DCE-CT perfusion against radioactive microsphere	72
Figure 3.1: CT-measured contrast concentration (enhancement) curves.....	93
Figure 3.2: Comparison of CT and PET functional images.....	94
Figure 3.3: Changes in HBF and HBV measurement as the tumor develops.....	97
Figure 3.4: Changes in PS and HAF as the tumor develops.....	99
Figure 3.5: Change in HBF and glucose utilization in tumors and normal tissue	101
Figure 3.6: Relationship between tumor SUV and HBF	102
Figure 3.7: Development of hypo-vascular region in the tumor core.....	103
Figure 4.1: Dynamic Contrast Enhanced CT Perfusion Maps.....	119
Figure 4.2: Tumor Progression and Survival of Animals with Hepatic Tumors	122
Figure 4.3: Hepatic Perfusion in Animals Treated With Thalidomide.....	124
Figure 4.4: Immunohistochemical Staining of Pericytes.....	126
Figure 4.5: Immunohistochemical Staining of CD31 and Vessel Analysis.....	127
Figure 4.6: Hemorrhage Fraction and Nuclei Density in the Hepatic Tumor	128
Figure 5.1: Measurement of Portal Hypertension with DCE-CT Perfusion.....	150

LIST OF APPENDICES

Appendix A – Animal experimentation ethics approval for the work contained in this thesis..... 155

Appendix B – An overview of the Johnson and Wilson model and a description of the tracer kinetic model used to measurement hepatic perfusion..... 156

LIST OF SYMBOLS, ABBREVIATIONS AND NOMENCLATURES

Symbol	Definition	Units
α	Hepatic arterial fraction	%
AFP	α -fetoprotein	-
ANOVA	Analysis of variance	-
Ang-2	Angiopoietin 2	-
A(t)	Time-enhancement curve from the aorta	HU
bFGF	basic Fibroblast growth factor	-
B_w	Rate of blood withdrawal	$\text{ml}\cdot\text{min}^{-1}$
CEUS	Contrast-enhanced ultrasound	-
CV	Coefficient of variation	%
DCE-CT	Dynamic contrast-enhanced Computed Tomography	-
DN	Dysplastic nodule	-
E	extraction fraction	-
ECM	Extracellular matrix	-
FDG	Fluorine-18 fluoro-2-deoxy-D-glucose	-
GEE	Generalized Estimating Equation	-
GRE	Gradient-echo-recalled	-
$H_A\text{BF}$	Hepatic arterial blood flow	$\text{ml}\cdot\text{min}^{-1}\cdot(100\text{ g})^{-1}$
HBV	Hepatitis B virus	-
HCC	Hepatocellular carcinoma	-
HIF-1	Hypoxia-inducible factor-1	-
HR	Heart rate	min^{-1}
HSC	Hepatic stellate cell	-
H(t)	Impulse residue function	-
$H_T\text{BF}$	Total hepatic blood flow	$\text{ml}\cdot\text{min}^{-1}\cdot(100\text{ g})^{-1}$
$H_T\text{BV}$	Total hepatic blood volume	$\text{ml}\cdot(100\text{ g})^{-1}$
HVC	Hepatitis C virus	-
I(t)	The weighted summation of A(t) and V(t)	HU
k	Rate constant of the washout of contrast from tissue	min^{-1}
LCD	Large cell dysplasia	-
MAC	Minimum alveolar concentration	-
MAP	mean arterial pressure	mmHg

N_t	Activity of the tissue sample	counts
P_aCO_2	Partial arterial carbon dioxide tension	mmHg
PDGF- β	Platelet-derived growth factor- β	-
PET	Positron Emission Tomography	-
PS	Permeability surface area product	$ml \cdot min^{-1} \cdot (100 g)^{-1}$
P_vBF	Portal venous blood flow	$ml \cdot min^{-1} \cdot (100 g)^{-1}$
PW	Perfusion-weighted	-
$Q(t)$	Time-enhancement curves from the normal liver or tumor	HU
R	Activity in the volume of blood extracted	counts
ROI	Region of interest	cm^2
SCD	Small cell dysplasia	-
T_0	Arrival time of contrast at the liver relative to the aorta	s
t	Time	s
T_c	Capillary transit time	s
TGF- β	Transforming growth factor- β	-
VEGF	Vascular endothelial growth factor	-
$V(t)$	Time-enhancement curve from the portal vein	HU

CHAPTER 1: INTRODUCTION

1.1 LIVER CANCER

Cancer is a major public health problem in North America and many other parts of the world and is the leading cause of death among men and women under age 85 years. Currently, one in 4 deaths in the North America is due to cancer. In 2008, an estimated 1,603,580 new cancer cases are projected, with 639,450 estimated deaths in the United States and Canada (1, 2). The incidence rates for all cancer sites combined have stabilized in men from 1995 through 2004 and in women from 1999 through 2004. The overall mortality rate has continued to decrease since 1990 in men and since 1991 in women (1). Moreover, between 1990 and 2004 the overall death rate for cancer in both sexes has decreased by 14%, conversely the death rate from primary liver cancer has increased by 34%. Additionally, in 2008 there is expected to be a 12% rise in the estimated number of new cases of primary liver cancer and 30 % rise in the estimated number of deaths over the levels in 2004 (1). The trend for increasing incidence of liver cancer is alarming especially since the downward projection of new cancer patients is expected to reverse and more than double from 1.36 million in 2000 to almost 3.0 million in 2050 (3). The higher incidence of liver cancer has been attributed to the increase in infection rate from hepatitis B virus (HBV) and hepatitis C virus (HVC), which leads to higher incidence of hepatocellular carcinoma (HCC) (4).

Liver cancers are among the most difficult to diagnose and to eradicate. Early detection of liver cancer is less common than for other cancers; the overall 5-year relative

survival rate between 1996 and 2004 was 11.7% (5). Hence, liver cancer patients have some of the poorest survival rates for all malignancies.

1.2 ETIOLOGY OF MALIGNANT PRIMARY LIVER CANCER

Most epidemiologic studies of malignant liver cancer have focused on HCC, the histologic type that represents more than 90 percent of all cases of primary liver cancer worldwide (6-8). Forty years ago the etiology of HCC was originally identified as a consequence of alcoholic cirrhosis, hemochromatosis, some metabolic disorders, certain types of drug injury (such as from oral contraceptives), or exposure to environmental toxins (such as aflatoxin) (7). This view slowly changed with the discovery of the HBV in the mid 1960s by Blumberg *et al.* (9) and its role in the development of HCC by Beasley *et al.* in 1981 (6). Several other factors have been shown to be causally related to HCC, in conjunction with or independently of HBV. There is strong evidence that HCV can also cause HCC, and there is limited evidence suggesting an interaction between HBV and HCV in the origin of the tumor (7, 10). There is converging evidence that tobacco smoking can cause HCC independently of HBV or HCV and that alcohol drinking can cause HCC only when it leads to clinical or subclinical cirrhosis (11). Other forms of cirrhosis also appear to be causally related to HCC, although it is based mainly on animal studies and population correlations rather than on epidemiological investigations (11).

The etiology of the more rare histologic types of liver cancers has also been successfully explored; angiosarcoma is frequently caused by thorotrast, and occasionally through exposure to vinyl chloride monomer and inorganic arsenic (12, 13); whereas,

cholangiocarcinoma has been linked convincingly to recurrent pyogenic cholangitis and liver fluke infestation, choledochal cysts, and thorotrast exposure (14). The pathogenesis of hepatic adenoma remains disputed, but the strong association with oral contraceptive use has been documented (15).

1.3 HEPATOCELLULAR CARCINOMA (HCC)

HCC is the most common form of primary liver cancer worldwide (16, 17). More than 1 million new cases are diagnosed each year; HCC has a dismal prognosis, with a median life expectancy of 6 – 9 months (16, 18-20). More than 80% of patients with HCC have underlying cirrhosis, and only 10 – 15% of patients with HCC are candidates for liver resection (17, 18). We believe that the greatest impact on the prognosis for patient with primary liver cancer will be made with improved diagnostic tools and treatment options for HCC. Hence, the remainder of this thesis will focus on HCC.

1.3.1 Cirrhosis

Cirrhosis is the strongest and the most common known risk factor for HCC, particularly cirrhosis related to HCV and HBV infections (21, 22). There are conflicting reports as to the rate at which chronic HCV infection can progress to liver fibrosis and the subsequent development of cirrhosis, liver failure, and HCC. Some published reports suggest that the prognosis of HCV is benign; with only 2%-3% developing cirrhosis at 20 years after infection (23, 24). Other reports suggest that the prognosis is much worse, with 51% of patients developing cirrhosis at 22 years (25). The evolution of HCV and HBV infected hepatic tissue to cirrhosis is associated with a progressive disruption of

normal anatomy and physiology, which leads to both regional and global perfusion changes. The progression is mediated through a process known as fibrogenesis.

Fibrosis can be classified as a wound-healing response to a variety of chronic stimuli. Aside from HCV and HBV infections these chronic stimuli may include alcohol abuse, drugs, metabolic diseases due to overload of iron or copper, autoimmune attack of hepatocytes or bile duct epithelium, or congenital abnormalities (7). In many ways, the liver's response to injury is an angiogenic one, with evidence of new blood vessel formation, sinusoidal remodeling, and pericyte (hepatic stellate cell) expansion (26). The process is characterized by an excessive deposition of extracellular matrix (ECM) proteins which includes three large families of proteins: glycoproteins, collagens, and proteoglycans (27). Following liver injury (fibrogenic stimulus), the hepatic stellate cell (HSC) undergoes a complex transformation or activation process where the cell changes from a quiescent, vitamin A-storing cell to that of an activated, myofibroblast-like cell (28). HSC are liver pericytes, which embrace with thorn-like micro-projections the endothelial cell layer of the sinusoids providing physical contact not only to sinusoidal endothelial cells, but also with the cell body to the hepatocytes (29). The similarities between the activation of HSC and tumor angiogenesis are demonstrated during fibrogenesis, these similarities includes: increased synthesis and secretion of ECM proteins, increased cell proliferation and migration through transforming growth factor- β (TGF- β), platelet-derived growth factor- β (PDGF- β) and oxidative stress mediated signaling pathways (30).

The overall net effect of a rapid increase in ECM synthesis, in combination with increased tissue levels of inhibitors of metalloproteinases activity, is formation of the

fibrotic scar. This is further exacerbated by the rearrangements of the sinusoidal architecture and the inability of the liver to degrade the ECM accumulation. The basement membrane-like ECM is replaced by a more fibrillar latticework, with increased levels of type I and III collagens, as cells in the sinusoid such as endothelial cells undergo phenotypic changes in a process referred to as “sinusoid capillarization” (31). As a result, portal venous blood flow (P_VBF) decreases and begins to bypass the liver parenchyma via small portosystemic venous shunts, this is counteracted by an increase in hepatic arterial blood flow (H_ABF), a process known as the hepatic arterial buffer response (32). In contrast, the normal liver receives approximately two-thirds of the blood flow via the portal vein; the remaining one-third is supplied by the common and proper hepatic arteries (33).

1.3.2 Hepatocarcinogenesis

Hepatocarcinogenesis is a multistep process; the majority of HCC cases arise in a background liver disease of either chronic hepatitis or cirrhosis, although HCC can arise in normal liver. Only a small proportion of HCC arises in non-cirrhotic livers, the majority of which show fibrosis ranging from mild fibrosis to septal or bridging fibrosis (34). However, the prevalence of small and large cell dysplastic foci is higher in cirrhotic liver with HCC than in those without HCC (35). Small cell dysplasia (SCD) in chronic liver disease are highly proliferative lesions that are seen as an early precursor lesion to HCC (36). Only a small minority will eventually evolve into a HCC, either directly or via the formation of a dysplastic nodule (DN). Conversely, large cell dysplasia (LCD) is not seen as a precursor lesion of HCC (37).

DNs are precancerous lesions in hepatocarcinogenesis and arise from a cirrhotic background (38). They are divided into high- and low-grade DNs, based on the histological features including cellular architecture, presence or absence of portal tracts and cytological features (38). The hepatocytes in low-grade DNs may appear normal or may show minimal nuclear atypia and slightly increased nucleocytoplasmic ratio and the absence of mitosis (39, 40). The cytoplasmic features may be different from those of the surrounding hepatic parenchyma because of the presence of a clonal cell population, the accumulation of fat, hemosiderin or copper (39). High-grade DNs may have any of the features of low-grade DNs along with evidence of cytological or structural atypia (41). Cytological atypia may be diffuse or focal and may be manifested as nuclear hyperchromasia, mild nuclear contour irregularities, cytoplasmic basophilia or clear cell change, high nucleo-cytoplasmic ratio and the presence of occasional mitotic figures (39, 41).

The number of portal tracts in low-grade DNs is usually greater and more regularly distributed than in high-grade DNs (42). In addition to portal vessels, DNs have been found to contain isolated arteries unaccompanied by bile ducts. Park *et al.* have identified a stepwise increase in the number of unpaired arteries with significant difference between cirrhotic and DNs (43). They also showed a gradual increase from cirrhotic nodules through low-grade and high-grade DNs, with the greatest numbers of unpaired arteries in HCC (43). In another study, Hayashi *et al.* correlated blood supply and histologic grade of precancerous and cancerous nodules in cirrhosis, and found that the intranodular portal supply relative to the surrounding liver parenchyma observed by CT during arterial portography was decreased (44). Conversely, the intranodular arterial

supply revealed by CT during hepatic arteriography was first decreased during the early stage of hepatocarcinogenesis and then increased in accordance with elevation of the grade of malignancy of the nodules (44). Therefore, quantitative assessment of unpaired arteries holds promise as a diagnostic criterion for nodule classification (45). We believe that the development of new methods to evaluate hepatic blood flow could lead to improve diagnosis and may lead to more effective means of differentiating various grades of the nodules.

In addition to the growth of unpaired arteries, DNs exhibit a variable degree of sinusoidal capillarization. Sinusoidal capillarization involves the transformation of fenestrated hepatic sinusoids into continuous capillaries, coupled with collagenization of the extravascular space of Disse and deposition of basement membranes near the endothelial cells and hepatocytes (46). Along with capillarization there is a progressive increase in proliferative activity and apoptotic activity have been noted from regenerative nodules to DNs to HCC (47). Tsuda *et al.* confirmed the clonal evolution of DN to HCC by demonstrating an identical pattern of integration of hepatitis B virus DNA in both DN and sub-nodule of HCC (48). Activation of cellular oncogenes, inactivation of tumor suppressor genes, genomic instability, including DNA mismatch repair defects and impaired chromosomal segregation, overexpression of growth and angiogenic factors, and telomerase activation may contribute to the development of HCC (49).

Small HCCs often consist of cells with high nucleo-cytoplasmic ratio and cell density at least two times greater than that of the surrounding hepatic parenchyma (41). They are up to about 2 cm in diameter and are classified into two major types: small HCC of distinctly nodular type and small HCC of indistinctly nodular type (50). Although it is

well known that HCC receives an exclusively arterial blood supply, the majority of well-differentiated HCCs of indistinctly nodular type receive a portal blood supply in addition to the arterial blood supply because they contain portal tracts within the tumor (41).

Whereas most small HCCs of distinctly nodular type show hyper-vascularity with the development of arterial tumor vessels (unpaired). Hence, there is progressive increase in hepatic artery blood supply with the progression of HCC. Non-invasive diagnosis tool that measures H_{ABF} maybe well suited to monitor the progression of DNs to HCC; especially in patients awaiting liver transplantation.

1.4 TUMOR ANGIOGENESIS

Like normal tissues, tumors require an adequate supply of oxygen, metabolic substrates and an effective way to remove metabolites. The initial requirements are met through simple diffusion up to a distance of 100 to 200 μm from the blood vessels. As metabolic demand increases blood vessels are recruited through a process known as angiogenesis. This process is regulated by a balance between pro- and anti-angiogenic molecules, and plays an important role in cancer from the initial stage of carcinogenesis to the end stage of metastatic disease (51). In fact, the growth of solid neoplasm is always accompanied by neovascularization. In the absence of neovascularization, most solid tumors stop growing when they are 2 to 3 mm in diameter and enter a dormant though viable state (52). Hence, new blood vessels arise from either the preexisting host vessels that are incorporated into the tumor; or microvessels arising from neovascularization (53).

1.4.1 Hypoxia and the Angiogenic Switch

The initiation of angiogenesis in a nascent tumor is often referred to as the “angiogenic switch,” a term initially coined by Folkman and Hanahan (54). The angiogenic switch is due to an imbalance between pro- and anti-angiogenic factors triggered by environmental and genetic factors, which includes: hypoxia, alterations in oncogene (eg. ras) or tumor suppressor gene function (eg p53) (55, 56). Once angiogenesis has been established, hypoxia persists as a result of aberrations in tumor microvascular geometry and function leading to imbalances between oxygen consumption and supply. Hypoxia-inducible factor-1 (HIF-1) transcription factor mediates adaptive responses to decrease in tissue oxygenation below normal levels and is activated directly by hypoxia as well as by hyperactivity of signaling pathways such as the human epidermal growth factor receptor 2 gene activation of phosphatidylinositol-3 kinase/Akt (56, 57).

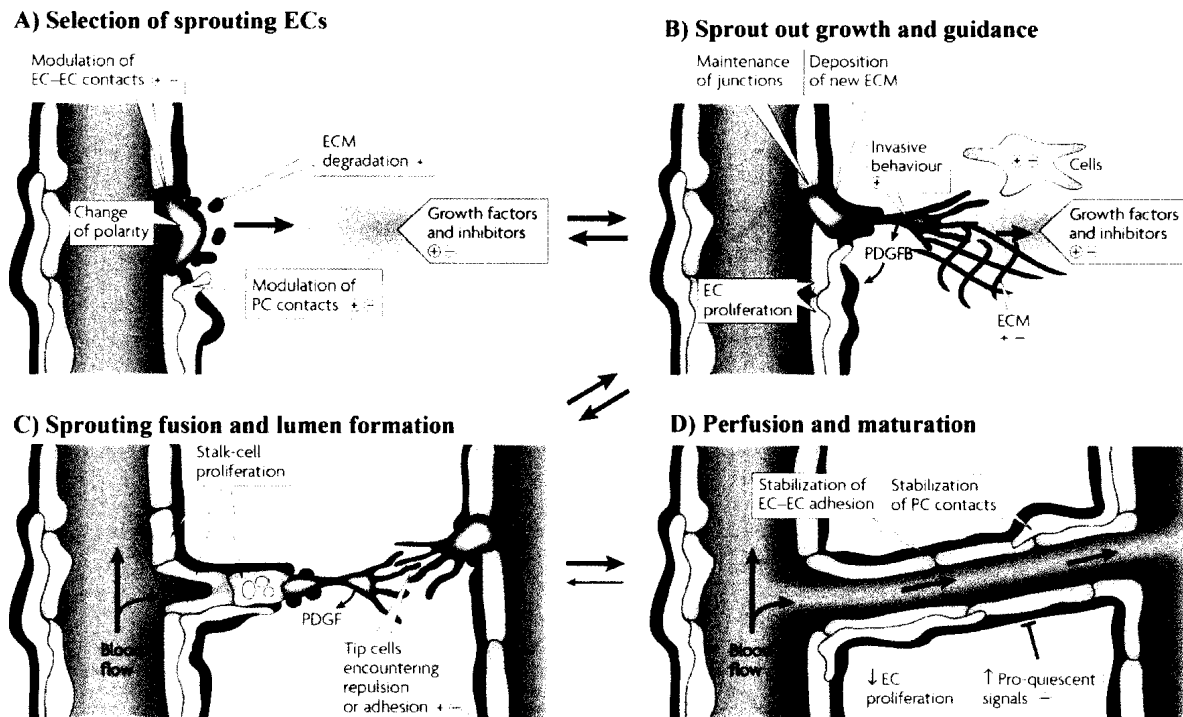
Tumors tend to have elevated levels of reactive oxygen/nitrogen species. Reactive oxygen species formation may in fact be stimulated by hypoxia-reoxygenation injury, which may occur in tumors with intermittent perfusion (58). Hence, reactive oxygen may serve as another source of proangiogenic stimulus in tumors. HIF-1 will also mediate the upregulation of several proangiogenic compounds such as basic fibroblast growth factor (bFGF), PDGF- β , vascular endothelial growth factor (VEGF), TGF- β , and angiopoietin 2 (Ang-2) and others (59, 60). These proangiogenic compounds leads to the formation of new blood vessels through at least two different mechanisms: sprouting angiogenesis or intussusceptive microvascular growth (51, 61).

1.4.2 Sprouting Angiogenesis

Sprouting angiogenesis is the growth of new capillary vessels out of preexisting ones; it involves several sequential steps that is mediated primarily by VEGF and begins with vasodilation of existing vessels (62). Ang-2 (a mediator of tyrosine kinase (Tie-2) signaling) is involved in the detachment of pericytes and loosening of the matrix (51). The basement membrane is locally degraded on the side situated closest to the angiogenic stimulus, interendothelial contacts are weakened, and endothelial cells (ECs) emigrate into the connective tissue, toward the angiogenic stimuli, Figure 1.1 (A) (51, 62). The migrating ECs maintain their basal-luminal polarity, Figure 1.2, where polarity refers to the subdivision of the plasma membrane into apical and basolateral domains and the distribution of the apical Na^+ channels and the basolateral $\text{Na}^+ - \text{K}^+ - \text{ATPase}$ (63). The migrating ECs form a slit-like lumen, the process takes place continuously with the lumen of the parent vessel and sealed by intact interendothelial junctions (64). For many years, the new blood vessels have been presumed to originate from the parent vessel's ECs. More recently, Asahara *et al.* suggested that some neovessels in tumors may be derived from circulating precursor ECs that originate from the bone-marrow (65). During angiogenic growth, some ECs within the capillary vessel wall are selected for sprouting. These ECs are known as tip cells and basement membrane is deposited continuously on them by the polarized ECs, Figure 1.1 (B-C) (64). If all cells were to react indiscriminately, the affected section of the vascular network might disintegrate and thereby compromise tissue perfusion. Proliferating pericytes migrate from the parent vessel along the basement membrane of the capillary bud, resulting in pericyte coverage of the new vessel, Figure 1.1 (D) (51). During maturation of nascent vessels, PDGF- β

recruits pericytes, whereas TGF-1 and Ang-1 stabilize the interaction between endothelial and pericytes (66).

Figure 1.1: Sprouting Angiogenesis*

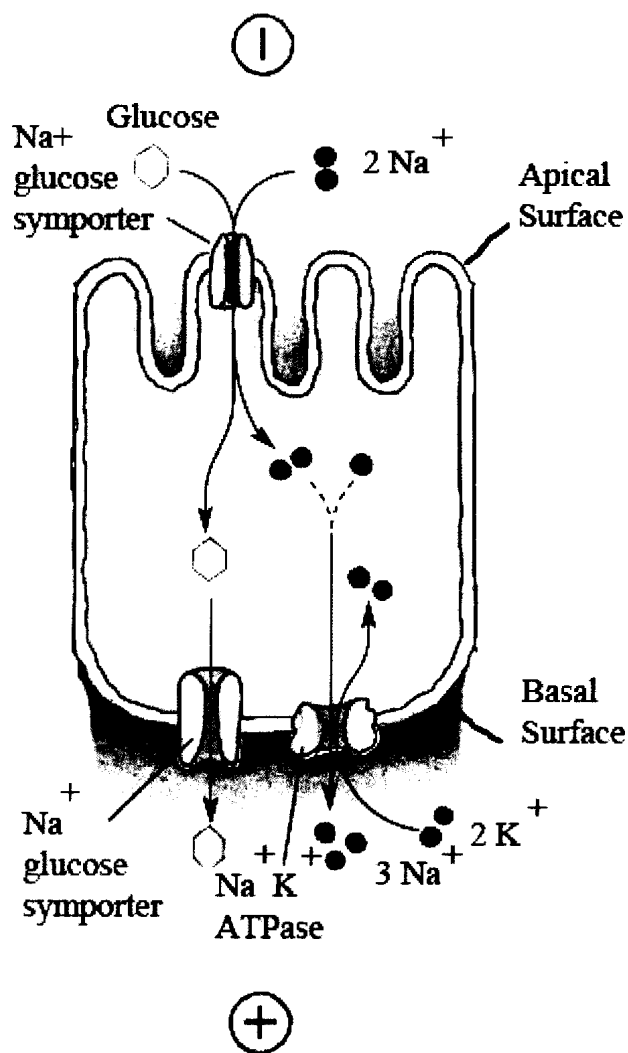


Sprouting is controlled by the balance between pro-angiogenic signals such as VEGF. **A)** In conditions that favor angiogenesis, some endothelial cells (ECs) can sprout (green), whereas others fail to respond (grey). Sprouting requires the flipping of apical-basal polarity, the modulation of cell-cell contacts and local matrix degradation. **B)** The growing EC sprout is guided by VEGF gradients. Release of PDGF- β by the tip cells promotes the recruitment of pericytes (PCs) to new sprouts. **C)** Adhesive or repulsive interactions on tip cells regulate the fusion of adjacent sprouts and vessels. **D)** Fusion processes at the EC-EC interfaces establish a continuous lumen. Blood flow improves

* Figure adapted from: Adams and Alitalo. Nat Rev Mol Cell Biol 2007; 8:464-478.

oxygen delivery and thereby reduces pro-angiogenic signals that are hypoxia-induced. Perfusion also promotes maturation processes and tight PC attachment.

Figure 1.2: Basal-luminal polarity



Basal-luminal polarity refers to the subdivision of the plasma membrane of EC into apical and basolateral domains and the distribution of the apical Na⁺ channels and the basolateral Na⁺-K⁺-ATPase. The apical surface of ECs faces the vessel lumen; therefore apical-basal polarity needs to be reversed when new sprouts emerge from the outer (basal) side of the endothelium.

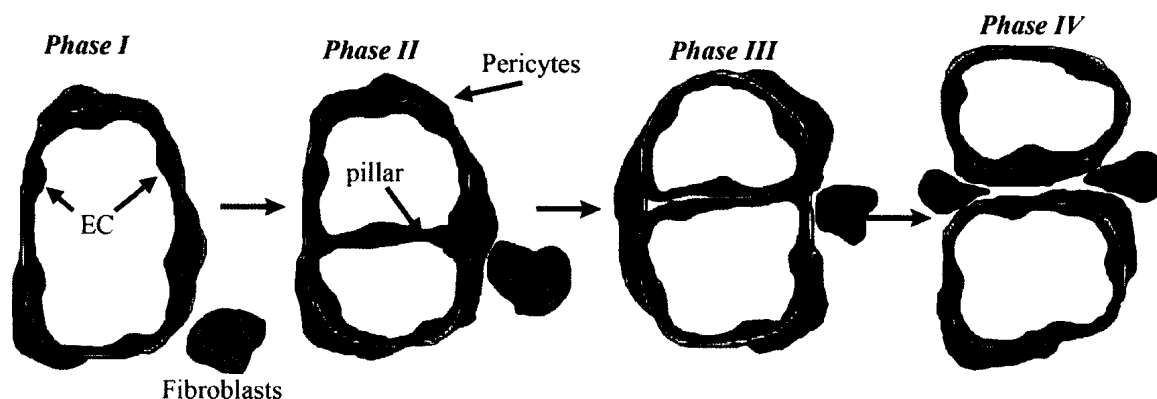
1.4.3 Intussusceptive Microvascular Growth (IMG)

IMG refers to vessel network formation by insertion of connective tissue columns, called tissue pillars, into the vessel lumen; the growth of these pillars result in partitioning of the vessel lumen (61). Pillar formation follows four sequential steps: phase I, a zone of contact is created between opposing capillary walls, Figure 1.3. Phase II is characterized by the reorganization of the inter-endothelial cell junctions and by central perforation of the bilayer. During phase III, an interstitial pillar core is formed that is invaded by pericytes and myofibroblasts that then lay down collagen fibrils, Figure 1.3. By this stage, transluminal pillars have a diameter of $\leq 2.5 \mu\text{m}$. During the final phase (phase IV), the pillars increase in girth without undergoing any further change in their basic structure after being invaded by fibroblasts and pericytes (67). This type of angiogenesis, which has been observed in a wide variety of normal and malignant tissues, is faster and more economical than sprouting. It occurs within hours or even minutes and does not primarily depend on EC proliferation, basement membrane degradation, and invasion of the connective tissue as in sprouting angiogenesis, Figure 1.1 (68).

Angiopoietins and their Tie-receptors, PDGF- β are believed to be involved in the induction of sprouting angiogenesis (62). The same factors and receptors could likewise mediate the endothelial-to-pericyte and endothelial-to-endothelial interactions observed during IMG, particularly with respect to Ang-2 and PDGF- β , both of which are essential for pericyte recruitment (69). Vascular shear stress has also been implicated in the initiation of IMG (68). Shear stress has been reported to involve interactions between pericytes, macrophages, and endothelial cells (70). Moreover, Djonov *et al.* showed that pericytes and/or periendothelial cells are recruited during the initial and final phases of

vascular pillar formation (71). It is also believed that the recruitment of pericytes contributes either to the synthesis and mechanical stabilization of the transcapillary pillar core or to the maintenance of a low vascular permeability during intussusceptions (72).

Figure 1.3: Intussusceptive Microvascular Growth[†]



Schematic representation of intussusceptive microvascular growth. The first step of the process is the development of the transluminal endothelial bridge. The division of the vessel is completed by the development of a connective tissue pillar through the vessel lumen. The pillar formation process is relatively unknown, but four different morphologies (phases I to IV) have been identified. Red cells are endothelial cells; brown cells are pericytes; gray, basement membrane; and blue fibroblast.

[†] Figure adapted from: Dome *et al.* Am J Pathol 2007; 170:1-15

1.5 SCREENING FOR HCC

The current screening tests clinically available for patients with cirrhosis are α -fetoprotein (AFP) level testing and ultrasound (73). AFP (normal reference range < 20 ng/ml) is the most widely used serum biomarker in HCC (74). It is a glycoprotein highly expressed in hepatocytes during fetal development. Pathological elevation of AFP expression is seen in hepatocytes regeneration and hepatocarcinogenesis (75). Serum levels greater than 400 ng/ml occurs in about 50% of symptomatic cases, it is particularly useful for both diagnosis of HCC and monitoring of treatment response (75). However, AFP is secreted in only about 70% of HCC; hence, it has low sensitivity (25% to 65%) for detecting HCC (76). Furthermore, false-positive AFP test results may be seen with cirrhosis and with flares of active hepatitis and false-negative test results are common with small tumors (77, 78). Hence, AFP is considered inadequate as the sole screening test for HCC; current guidelines advocate the use of ultrasound and AFP at 6–12 months frequency in high-risk patients (79).

1.6 IMAGING EVALUATION OF HCC

Non-invasive diagnosis of HCC is most beneficial for patients with cirrhosis and a focal hepatic mass > 2 cm. In early cirrhosis, the liver may appear normal in non-invasive imaging (CT, MRI, and ultrasound). With disease progression, nodularity of the liver surface and heterogeneity of the hepatic parenchyma can be seen more easily. The porta hepatis and interlobar fissure may appear widened due to shrinkage of the right lobe and enlargement of the caudate lobe and the lateral segment of the left lobe. However, the most important clinical manifestations of cirrhosis are related to the development of

portal hypertension (31). HCC derives its blood supply predominantly from the hepatic artery, whereas the normal liver parenchyma receives blood from both the hepatic arterial and portal vein (44). The hallmark of HCC in CT or MR is the presence of arterial enhancement followed by delayed hypointensity of the tumor in the portal venous and delayed phases (80). These alterations in hepatic morphology can be detected with most imaging modalities.

1.6.1 Ultrasound

Ultrasound has been used in medical imaging for over half a century. Ultrasound is currently one of the most important, widely used, and versatile imaging modalities in medicine. Ultrasound is performed primarily by using a pulse-echo approach with a brightness mode (B-mode) display (81). This involves transmitting small pulses of ultrasound into the body, detecting echo signals resulting from reflections from structures lying along the path length of the pulse, and then combining the echo signals from many sequential, coplanar pulses into an image (81). Ultrasound images are tomographic and are acquired at “real-time” rates. The technology is relatively inexpensive and portable, especially when compared with modalities such as MRI and CT. As mentioned above, the current screening tests clinically available for patients with cirrhosis are α -fetoprotein (AFP) level testing and ultrasound (73).

In ultrasound images small nodules of HCC tend to be homogeneous and hypoechoic, whereas large masses are usually heterogeneous (82). Small nodules of well-differentiated HCC sometimes have a hyperechoic pattern, which is suggestive of fat deposition (82). In more advanced cases of HCC, portal vein thrombosis, hepatic and

portal vein invasion, and biliary obstruction may occur (82). Ultrasound has been shown to have low sensitivity but high specificity in revealing HCCs and DN in patients with a cirrhotic liver (83). Colli *et al.* reviewed the accuracy of ultrasound in diagnosing HCC in patients with chronic liver disease and found a heterogeneous sensitivity and specificity of 30–100% and 73–100% respectively (84).

The introduction of phase-inversion harmonic contrast-enhanced ultrasound (CEUS) is believed to significantly improve lesion detection (85, 86). CEUS is a dynamic real-time scanning sequence performed with intravascular micro-bubble contrast agents that contain either air or other gases. The US images are based on the interactions between micro-bubbles and US beam. Contrast-specific techniques suppress linear US signals coming from tissues and use the non-linear response of micro-bubbles to enhance signals from the contrast agent over the background (87). CEUS has the potential to combine information about the tumor vessel morphology and the direction of filling of the contrast. The resulting image can often differentiate one lesion from another (87). However, Lencioni *et al.* suggest that CEUS has not resulted in any significant improvement in the ability of ultrasound to detect tumor foci smaller than 10 mm (88). He suggests that CT or MR imaging is still mandatory for proper intrahepatic staging of the disease. Other improvement has been made with the use of color Doppler ultrasound (89). Color Doppler ultrasound provides an estimate of the mean velocity of flow within a vessel; flow direction is arbitrarily assigned the color red or blue, indicating flow towards or away from the transducer respectively (90). The contrast enhancement at the liver-specific phase is crucial for the differential diagnosis of liver tumors and for the assessment of tumor vascularity (89, 91). The liver-specific phase reflects the period

during which micro-bubbles are visible after injection, usually 5 min in healthy liver. To differentiate HCC from hepatic metastasis the hepatic tumor index is calculated, which is the ratio of the tumoral peak systolic velocity to the peak systolic velocity of the right or left hepatic artery, on color Doppler ultrasound. A hepatic tumor index ≥ 1.0 is associated with 76% sensitivity, 92% specificity and 82% accuracy in distinguishing HCCs from hepatic metastases (89).

1.6.2 Magnetic Resonance (MR) Imaging

MR imaging plays an increasingly important role in non-invasive imaging of different pathologic disorders and their response to treatment. Advances in MR imaging software and hardware, including the use of parallel imaging and surface phased array coils, provide faster sequences covering the entire liver that can be acquired within a breath-hold, decreasing motion and respiratory artifacts (92). New volumetric sequences have enabled three-dimensional serial dynamic imaging of the liver with very high spatial and temporal resolution, reducing section misregistration and motion artifacts while improving multiplanar reformations (93).

Even with the new improvement to MR imaging the detection and characterization of hepatic nodules in the multistage development of HCC in a cirrhotic liver represent a challenge. In MR imaging, a typical focal HCC shows slightly high signal intensity on non-enhanced T2-weighted images, and a hyper-intense signal intensity in comparison with the surrounding normal liver during the arterial phase of contrast enhanced imaging owing to the tumor's predominantly arterial supply (94). Conversely, the standard non-enhanced T1-weighted sequence is often not helpful in the

differentiation of HCC because it ranges from low to iso- or even hyperintense (94). Regenerative nodules are also iso-intense relative to background liver parenchyma on T1 and T2-weighted MR images. However, in fast imaging techniques using gradient-echo-recalled (GRE) sequences non-DN may also appear hyperintense on T1-weighted images without signal loss in the opposed-phase in cirrhotic livers (95). The opposed-phase or out-of-phase image is a gradient echo image where the processing of water and fat spins are 180° out of phase when the echo to be measured occurs. It is commonly used to identify tissues containing a significant proportion of intracellular microscopic triglycerides, such as fatty liver (96). Hence, the use of intravenous contrast material with multiphasic imaging is essential to accurately identify and characterize focal hepatic lesions.

Gadolinium (Gd) chelates are the most common MR contrast medium. They are optimally used when administered as a rapid bolus, and imaging is performed with a T1-weighted spoiled GRE sequence that is repeated in a dynamic serial fashion (97). Gd chelates are typically used to capture the capillary bed enhancement also termed the hepatic arterial–dominant phase (98). Although Gd enhancement is present in portal veins, the majority of the contrast materials in hepatic tumors are delivered primarily by the hepatic arteries (99). On hepatic arterial–dominant phase T1-weighted spoiled GRE images, various types of liver lesions have distinctive enhancement patterns: hemangiomas show peripheral nodules of enhancement in a discontinuous ring, focal nodular hyperplasia show intense uniform enhancement, metastases show ring enhancement, and HCC show diffuse heterogeneous enhancement (97, 100, 101).

More recently, hepatocytes targeted compounds like gadobenate dimeglumine, gadolinium ethoxybenzyl diethyl-lene-triamine-pentaacetic acid and mangafodipir trisodium have been developed as MR contrast medium (102-104). Hepatocyte selective contrast agents are taken up by hepatocytes and eliminated through the biliary system. The normal liver and focal hepatic lesions that contain hepatocytes take up these agents, and lesions devoid of hepatocytes do not take up these agents. Most studies showed that delayed phase imaging of hepatocytes targeted compounds ranging from 20 to 120 min contributes to improved detection of small metastases (102-104).

Despite technical improvements, MR imaging remains relatively insensitive for the detection of tiny HCC nodules (smaller than 10 mm) and for the identification of tumor vascular invasion into peripheral portal vein branches. Lesion by lesion analysis of MR imaging findings correlated with histopathologic results shows sensitivity and positive predictive values varying between 33 – 84.7% and 54 – 97.4% respectively (105-109).

Attempts to improve the sensitivity and the performance of MRI revolved around the development of hepatic perfusion imaging techniques (110-113). Annet *et al.* showed that hepatic perfusion measurement made with MRI correlated with the severity of cirrhosis and portal hypertension (114). This suggest that the measurement of hepatic perfusion; namely, the portal perfusion fraction can be used to determine grades of cirrhosis. MRI hepatic perfusion has also been shown to differentiate between liver metastases from metastatic colorectal cancer and HCC (115). However, evaluation of the diagnostic accuracy of MRI perfusion over conventional contrast enhanced MRI is still needed in order to determine the value of the perfusion measurements. The major

obstacle to the use of MRI hepatic perfusion is the nonlinearity between the MRI signal and contrast agent. The non-linearity of the MRI signal is due to the saturation of the MRI signal at high concentration of gadolinium. Saturated signal leads to the underestimation of the vascular input function and the over estimation of the hepatic perfusion. Dynamic contrast enhanced (DCE) – computed Tomography (CT) offers the opportunity to overcome this problem, because there is a linear relationship between the concentration of iodinated contrast and signal intensity in CT images, measured in Hounsfield Units (HU).

1.6.3 Computed Tomography (CT)

Over the past few years, multi-detector row computed tomography (CT) technology has been introduced into clinical practice; however, the first successful clinical scanner developed in 1972 by Godfrey Hounsfield was single slice (116). The next major breakthrough occurred with the introduction of slip-ring technology in the 1980s; this allowed for the continuous data acquisition over many rotations and dynamic measurements of contrast distribution in the body (117). Today multi-detector row CT scanners use 4, 16, 64, 128, 256 and 320 contiguous rows of detectors to decrease scanning time, without consequent loss of spatial resolution along the axis of scanning. These scanners allow thin sections in a single breath-hold, greatly improving longitudinal resolution without compromising scan time, which results in nearly isotropic image resolution of about 1 mm. CT is now the most commonly used imaging modality in diagnosing HCC in the United States and Canada (118). In patients undergoing HCC screening while awaiting liver transplantation, screening with CT is associated with the

greatest gain in life expectancy and is possibly cost-effective at \$101, 100 per life year saved (LY) vs. \$74, 000 per LY for ultrasound combined with AFP (119).

The current practice in many medical centers for scanning cirrhotic livers suspected of having HCC include non-enhanced, arterial and portal venous scans. The non-enhanced phase is essential to ensure that small siderotic (iron filled) regenerative nodules that appear as more attenuating than the liver are not mistaken for enhancing nodules in the arterial phase (120). In non-enhanced CT images HCC appears predominantly hypo-attenuated; however, small well-differentiated tumors are often isoattenuating to liver parenchyma (121).

Dual-phase imaging in the arterial and portal venous phases is necessary to detect small tumors with helical scanning on multi-detector scanners. Arterial phase and portal venous scans are obtained 20 and 60 seconds after the start of intravenous injection of contrast material respectively (122). Vascular hepatic tumors, such as HCC, receive their blood supply predominantly from the hepatic artery; early arterial phase CT images show intense hepatic arterial enhancement, minimal portal venous enhancement and essentially no hepatic venous or parenchymal enhancement (123). Late arterial phase images demonstrate substantial portal venous and hepatic artery, slight parenchymal, and no hepatic venous enhancement. In theory, HCC are best detected during a phase of maximal tumor enhancement and minimal hepatic parenchymal enhancement. HCC has a variable vascularity with varying degree of hepatic artery and portal vein supply, due to its histological tumor grade and underlying liver damage. The late arterial phase images depict more hypervascular lesions than the early arterial phase (124). Assessment of both early and late arterial phase images produces the greatest sensitivity and positive

predictive value (123). A further evolution of the scanning protocol includes triple arterial phase scanning, with the middle arterial phase imaging being claimed as the most sensitive for HCC detection (125). In contrast to HCC, regenerative and dysplastic nodules are difficult to visualize because they do not enhance in the arterial phase but enhance homogeneously and similar to the surrounding parenchyma in the portal venous phase (126).

The reported sensitivities of CT in the detection of HCC vary. An analysis of CT imaging findings correlated with histopathologic results from explanted livers shows sensitivity and positive predictive values varying between 59 – 78.8% and 59 – 95.1% respectively (106, 107, 109, 127, 128).

1.6.4 Positron Emission Tomography (PET)

PET imaging relies on the nature of the positron decay. After emission, the positron loses energy through interactions with the surrounding tissue until it annihilates with an electron. The gamma ray pairs from positron annihilation are captured in coincidence by opposing PET detectors. Positron emitters such as fluorine 18 (^{18}F) are used to label substrates like deoxyglucose to create the radiopharmaceutical, Fluorine-18 fluoro-2-deoxy-D-glucose (FDG). FDG is a glucose analog that competes with glucose at transport sites on the cell membrane and participates only in the first step, phosphorylation by hexokinase to deoxy-D-glucose -6-phosphate, of the glycolytic pathway, after which it is trapped in cells. In general there is an increased uptake of glucose in malignant cells. Anaerobic glycolysis are increased in general in malignant

tumors, possibly related to the increased energy demands of more frequent cellular division in tumor expansion and not enough blood flow to deliver oxygen required (129).

FDG-PET imaging has been evaluated in the detection of HCC; it has a poor sensitivity between 0 and 55% (109, 130, 131). However, it has demonstrated high sensitivity (96%) and specificity (99%) in the detection of hepatic metastasis from colorectal cancer (132). Khan *et al.* showed that glucose metabolism assessed by FDG-PET reflects the degree of differentiation of HCC (130). They showed that well-differentiated HCCs have a low detection rate by FDG PET because their metabolic activity is similar to that of the surrounding liver parenchyma. However, large moderately or poorly differentiated HCC are more likely to be detected with FDG because of the increased metabolic activity.

Improvements in PET technology have led to the development of scanners with improved temporal and spatial resolution and the ability to perform dynamic PET scans. These technological improvements have led to various attempts to design a hepatic perfusion imaging technique using ^{13}N -ammonia (half-life 20 minutes) and ^{15}O -labeled water (half-life 2 minutes) (133-136). However, there are limitations to the techniques that may limit their availability; mainly the use of short lived radio-isotopes and the need to have a cyclotron on site. Also, the measurement of the hepatic artery and the portal vein input functions are difficult with PET, because of the limited spatial resolution. In contrast, DCE-CT has high spatial and temporal resolution, allowing for separate measurement of the arterial and portal-venous input functions. The use of PET to measure hepatic perfusion has shown promising results, Koh *et al.* showed that hepatic perfusion measuring can be useful in predicting the preferential delivery of drugs to

hepatic cancers (137). Likewise, Fukuda *et al.* showed that the measurement of HBF and the metabolic rate of oxygen can be used to identify the disparity between the supply and demand of oxygen in tumors (138). Prolong disparity between the supply and demand of oxygen increases the likelihood that the tumors would develop hypoxia, which is known to impede therapy and stimulate more aggressive behavior in tumors. Hybrid PET/CT scanners has an advantage over conventional PET scanner because the glucose metabolic activity can be measured using FDG (110 minutes half-life) and the hepatic perfusion can be measured using DCE-CT. This would eliminate the need to have the on-site production of short-lived radio-isotopes, hence expanding the availability and use of PET scanners.

1.7 TREATMENT OF HEPATIC TUMORS

Treatments for HCC have been conventionally divided into palliative and curative. Palliative treatments do not aim to cure, but in some cases can achieve good response rates and even improve survival. Curative treatments, such as resection, liver transplantation, and percutaneous ablation, induce complete responses in a high proportion of well selected patients and are expected to improve survival. Unfortunately, because of late discovery and selection criteria only 10 – 15% of patients with HCC are candidates for liver resection (17, 18). The 5 years survival rate in hepatic resection patients who have one asymptomatic HCC and extremely well preserved liver function is 70%, whereas survival is 50% among patients with portal hypertension and their recurrence rate exceeds 70% at 5 years after resection (139-141). We believe that monitoring blood flow disturbance using a non-invasive perfusion imaging could give

greater insight on the extent of portal hypertension and use this information as part of the surgical selection criteria.

Theoretically, transplantation might simultaneously cure the tumor and the underlying cirrhosis. Currently, the Conventional Milan selection criteria for liver transplantation are candidates that have one HCC smaller than 5 cm or up to three nodules smaller than 3 cm (142). The 5 years survival rate for these transplant patients is 70%, with a recurrence rate lower than 15% (139, 143, 144). However, the shortage of donor organs and long waiting period leads to the progression of both the tumor and the underlying liver disease. Several issues, including optimal selection criteria, the role of living donor liver transplantation, and the benefit of preoperative adjuvant treatment, remain unresolved.

Palliative treatments are given to patient with advanced stages of HCC (145). Arterial embolisation is the most widely used treatment for unresectable HCC (79). As the tumor grows the blood supply becomes progressively arterialized; hence, acute arterial obstruction with chemotherapy agents induces ischemic tumor necrosis with a high rate of objective responses (79). Arterial embolisation achieves partial responses in 16–55% of patients and substantially delays tumor progression and vascular invasion (146). Vascular invasion, i.e. the shedding of tumor cells into blood vessels is a major predictor of recurrence and survival (144).

Historically, radiation therapy has not played a major role in the management of patients with unresectable liver cancer; primarily because of the low tolerance of whole liver to high dose above 25 – 30 Gy and the induction of hepatitis at that level (147).

Recent advances that allow for the safe delivery of higher dose are: CT guided 3-dimensional radiation planning techniques, to deliver high radiation doses that conform tightly to the tumor; organ tracking, to account for organ motion because of breathing; and improved knowledge of the partial volume tolerance of the liver to radiation (148). More recently, Cao *et al.* has demonstrated that measurement of P_vBF can be used as a predictive measure of liver function after fractionated radiotherapy and that perfusion imaging has the potential to create individualized radiotherapy (149).

The vascularity of HCC makes it an excellent candidate for the action of angiogenesis inhibitors. In recent years there has been tremendous interest in using inhibitors such as thalidomide; which inhibits VEGF and bFGF (150-152). Unfortunately, preliminary results from clinical trials suggest that single-agent angiogenesis inhibitor therapy in advanced solid tumors have poor efficacy (153). In contrast, angiogenesis inhibitors with adjuvant chemo- or radiation therapy have produced synergistic beneficial response in both animal and clinical trials (154-157). Ansiaux *et al.* showed that angiogenesis inhibitors increases tumor oxygenation, blood flow and radio-sensitizes tumors (154, 158). The exact mechanisms for this synergistic benefits are still unknown, however Jain (159) postulates that angiogenesis inhibitors selectively prune away sprouting vasculature leading to a transient normalization of the tumor vasculature that improves pericyte coverage and perfusion and sensitize tumors to both chemo- and radiation therapy. Lin and Sessa (160) argue that knowledge of the 'normalization window' in which vessels become normalized is required to optimize adjuvant cytotoxic therapies with angiogenesis inhibitors. During this period tumor blood flow and oxygenation transiently increases, making chemo- or radiation therapy more effective

(160). Hence monitoring hepatic tumor blood flow after treatment with angiogenesis inhibitors may be useful in identifying which patient will experience vascular normalization.

1.8 ADVANCE FUNCTIONAL IMAGING

HCC is a hypervascular tumor mainly supplied by hepatic arteries, whereas normal liver parenchyma and dysplastic nodules are supplied by both the hepatic artery and portal vein (41). This difference in blood supply has been exploited in order to develop diagnostic techniques (86, 89, 98-100). As a result, a variety of imaging modalities have shown that knowledge of tumor vascularity can be used to differentiate various grades of HCC (44, 161, 162). Furthermore, Ebied *et al.* used triple-phase helical CT to show that patients with hypervascular tumors had improved survival after transcatheter arterial chemoembolization (163). Unfortunately, there has been no established quantitative or even a semi-quantitative grading system for HCC vascularity. Pandharipande *et al.* suggest that existing diagnostic imaging techniques provide limited evaluation of tissue characteristics beyond morphology and that perfusion imaging of the liver has potential to overcome this limitation (45). Hence, we embarked on a research goal to develop a non-invasive imaging technique that can measure hepatic perfusion.

1.8.1 Tracer Kinetic Model Selection

Tracer kinetic models are used to estimate tissue perfusion from dynamic contrast enhanced CT data. They are usually described as linear compartmental models of homogeneous (well mixed) compartments (HC) or distributed parameter as in the

Johnson and Wilson model (164). An important consideration in the development of these models is the properties of the CT based contrast agents. CT contrast agents are hydrophilic; hence they are excluded from the intracellular space. They are also inert, so compartment models describe the flow of contrast through two compartments, which are the intravascular and extravascular space. In the HC model the tracer is assumed to be distributed instantaneously upon arrival and the concentration gradient of the tracer within the compartments is zero. The compartments are separated by a semi-permeable membrane and passage of contrast between the compartments is governed by the blood flow (F) and extraction efficiency (E), also known as the transfer constant (F•E). E is the fraction of contrast agent arriving at the tissue that leaks into the extravascular space in a single passage through the vasculature (165). It is related to the capillary permeability surface area product (PS) and blood flow (F) via the following equation (165):

$$E = 1 - e^{-\left(\frac{PS}{F}\right)} \quad (1.1)$$

The advantage of the HC model is its numeric simplicity, a variety of nonlinear regression methods have been used to estimate F•E. The disadvantage with the HC model is that F and E cannot be estimated separately, because they are determined together as the transfer constant.

Materne *et al.* further simplified the HC model in order to estimate hepatic blood flow (166). They assume the instantaneous diffusion of contrast between the fenestrated liver sinusoid and the extravascular space of Disse (167); hence, the two compartment model converges to a one compartment model. This allowed for the estimation of hepatic

blood flow from $F \cdot E$ by assuming that the E of contrast agent in the liver is equal to one. However, that assumption in the normal liver is highly improbable. In order for E to be equal to one, PS must be orders of magnitude larger than F (equ 1.1); since, PS of CT contrast agent is driven by passive diffusion it is unlikely to be greater than F . A more likely scenario is that PS is equal to F , in which case it is impossible to separate F and E using Materne's model. Another drawback is that the liver sinusoids become capillarized during fibrosis (cirrhosis) (168), which may further reduce E of contrast agent heterogeneously in the affected liver parenchyma. Larson *et al.* published a general critique of the homogeneous two compartment model; their result suggest that the assumptions of instantaneous distribution of the contrast agent and zero concentration gradient in the vascular compartment over simplifies the complexity of brain tissue perfusion and leads to the overestimation of flow (169). The Johnson and Wilson model accounts for the concentration gradient in the vascular compartment by defining tracer concentration as a function of both time and space (170).

1.8.2 Measuring Blood Flow Using the Johnson and Wilson Model

There are a number of in-vivo dynamic contrast-enhanced (DCE) CT methods that have been developed to measure hepatic perfusion (166, 171-173). Unfortunately, they lack the advantages provided by the Johnson and Wilson model (170). The Johnson and Wilson model assumes that as far as modeling the distribution of inert contrast in tissue, the latter can be divided into capillaries and intersititial space only. However, individual capillaries are beyond the resolution limit of conventional imaging technology including CT. Hence, all the capillaries within an image voxel can be summed together as

a single cylinder, with length L and blood volume V_b . There is a concentration gradient that changes with time along the length of the cylinder from the arterial to the venous end. Within the same image voxel the interstitial tissue is modeled as a homogenous compartment (cylinder) around the capillaries that only changes with respect to time (170). The advantage of the model is that it allows for the separation estimation of F from E rather than estimation of their product as in HC models (170). The disadvantage of the model is that the solution is complex, being in the Laplace domain and a simple time domain solution of the model remained elusive for many years. This disadvantage was overcome by St. Lawrence and Lee who derived a closed form time domain solution using the adiabatic approximation (174). Subsequently, Cenic *et al.* developed and validated a CT base method that relies on the adiabatic approximation and deconvolution to compute F , blood volume (BV) and mean transit time (MTT) in brain tumor (175).

1.8.3 Measuring Hepatic Blood Flow

To calculate parametric maps, DCE CT images are acquired at a stationary couch location in the tissue of interest after a pulse injection of iodinated contrast. The rate of input of contrast agent into the tissue is $F \cdot I(t)$, where F is the blood flow in the tissue and $I(t)$ is the arterial concentration of contrast over time in an input artery. The technique relies on representing the arterial input curve as a series of delta or impulse functions (injections). The passage of contrast through the tissue from each of the delta injection was described by the Johnson-Wilson model (170) with the adiabatic approximation (174) and gives a closed-form solution for the impulse residue function (176), $H(t)$, of the tissue as:

$$H(t) = \begin{cases} 1 & 0 \leq t \leq T_c \\ E e^{-k(t-T_c)} & t > T_c \end{cases} \quad (1.2)$$

where T_c is the capillary transit time, k is the rate constant of the washout of contrast from the tissue.

We modified the Cenic *et al.* (175) model, as discussed above, to account for the liver's dual blood supply. The input $I(t)$ is modified to include the input from hepatic artery (aorta) $A(t)$ and portal vein $V(t)$:

$$I(t) = \alpha A(t) + (1 - \alpha)V(t) \quad (1.3)$$

where α is the fraction of liver blood flow contributed by the hepatic artery.

If the concentration (enhancement) of contrast input to the liver, $I(t)$, is known, then the measured liver parenchymal time enhancement curve, $Q(t)$, can be calculated as the convolution of $I(t)$ and $H(t)$:

$$\begin{aligned} Q(t) &= F \cdot I(t - T_0) * H(t) \\ &= F \cdot I(t) * H(t - T_0) \end{aligned} \quad (1.4)$$

where $*$ is the convolution operator, F is H_TBF and T_0 is the start time of the liver parenchyma time enhancement curve relative to that of $I(t)$.

The validity of equation (1.4) assumes that liver blood flow is constant and $Q(t)$ is linear with respect to $I(t)$. With $A(t)$ and $V(t)$ measured, the estimated values of α (equ. 1.3), F (equ. 1.4), E , T_c and k (equ. 1.2) are changed iteratively in the deconvolution process to

achieve an optimum fit by (equ. 1.4) to the measured parenchymal time enhancement curve.

1.9 RESEARCH GOAL AND OBJECTIVES

The goal of this thesis is to develop a non-invasive imaging technique that can measure hepatic perfusion. This was accomplished by completing three main objectives:

- i. The first objective of the thesis is to use the Johnson and Wilson model along with the adiabatic approximation to create a more realistic model of hepatic perfusion. This thesis also aims to validate this new hepatic perfusion technique against the gold standard radioactive microsphere and determine the precision using Monte Carlo simulations.
- ii. The second objective is to show that DCE-CT hepatic perfusion measurement can be used to enhance the functional imaging capabilities of hybrid PET/CT scanners by providing perfusion image to the already established FDG PET imaging protocol. Furthermore, to demonstrate that monitoring hepatic perfusion and glucose metabolism can be used to identify the disparity between the supply and demand of oxygen in hepatic tumors.
- iii. The third objective is to demonstrate the effectiveness of DCE-CT in providing meaningful information about tumor vasculature following therapy. Angiogenesis inhibitors like thalidomide has been know to inhibit blood vessel formation and

induce vascular normalization in tumors. We monitor hepatic tumor blood flow following thalidomide therapy to identify tumor vascular normalization.

1.10 THESIS OUTLINE

1.10.1 Validation of Dynamic Contrast Enhance Computed Tomography

Measurement of Hepatic Perfusion (*Chapter 2*)

The accuracy of hepatic perfusion measured with DCE-CT was validated against the gold standard of radioactive microspheres and the precision was determined by repeated measurements in the same subject and Monte Carlo simulations. The chapter is based on the paper entitled “Hepatic perfusion in a tumor model using DCE-CT: A accuracy and precision study”, published in the journal *Physics in Medicine and Biology* vol. 53 (16): pp. 4249 – 4267 (2008) by Stewart EE, Chen X, Hadway J, Lee TY.

1.10.2 Assessment of the Relationship between Hepatic Tumor Blood Flow and

Glucose Utilization using *in vivo* PET/CT (*Chapter 3*)

As tumors grow their glucose utilization (metabolic demand) increases, an equivalent increase in oxygen supply via increased blood flow is necessary to maintain aerobic respiration. The uncoupling of the relationship between tumor blood flow and glucose utilization may lead to tumor hypoxia. In this chapter we investigated whether PET/CT can identify the uncoupling of this relationship. The chapter is based on the paper entitled “Correlation between hepatic tumor blood flow and glucose utilization in a rabbit liver tumor model”, published in the journal *Radiology* vol. 239 (3): pp. 740 – 750 (2006) by Stewart EE, Chen X, Hadway J, Lee TY.

1.10.3 Investigating the Effect of Thalidomide on Hepatic Perfusion and Vascular Remodeling (*Chapter 4*)

Thalidomide has been shown to inhibit VEGF and prevent the formation of new tumor blood vessels (anti-angiogenesis), thus inhibiting tumor growth. In addition, recent preclinical studies support the concept of a transient normalization of the tumor vasculature improving perfusion and sensitizing tumor to adjuvant chemo- and radiation therapy during the early stage of treatment. This chapter investigates whether DCE-CT hepatic perfusion measurements can be used to identify vascular normalization. The chapter is based on the paper entitled “DCE-CT perfusion identify differential hepatic blood flow response during thalidomide induced tumor vascular normalization”, which was submitted for publication to the journal *Clinical Cancer Research* in October 2009 by Stewart EE, Sun H, Chen X, Schafer P, Chen Y, Garcia B, Lee TY.

1.10.4 Conclusion and Future Work (*Chapter 5*)

In the final chapter, the major results of the thesis were summarized along with a discussion of their clinical and experimental relevance. Research interests for future work pertaining to the measurement of hepatic perfusion were discussed and the main conclusion of the thesis was outlined.

1.11 REFERENCES

1. Jemal A, Siegel R, Ward E, et al. Cancer statistics, 2008. 58 ed, 2008; 71-96.
2. Canadian Cancer Statistics. Canadian Cancer Society/National Cancer Institute of Canada: Toronto, Canada; ISSN 0835-2976, 2008.
3. Hayat MJ, Howlader N, Reichman ME, Edwards BK. Cancer statistics, trends, and multiple primary cancer analyses from the Surveillance, Epidemiology, and End Results (SEER) Program. *Oncologist* 2007; 12:20-37.
4. Di Bisceglie AM. Epidemiology and clinical presentation of hepatocellular carcinoma. *J Vasc Interv Radiol* 2002; 13:S169-S171.
5. Ries LAG, Melbert D, Krapcho M, et al. SEER Cancer Statistics Review, 1975-2005. National Cancer Institute. Bethesda, MD, 2008.
6. Beasley RP, Hwang LY, Lin CC, Chien CS. Hepatocellular carcinoma and hepatitis B virus. A prospective study of 22 707 men in Taiwan. *Lancet* 1981; 2:1129-1133.
7. Seeff LB, Hoofnagle JH. Epidemiology of hepatocellular carcinoma in areas of low hepatitis B and hepatitis C endemicity. *Oncogene* 2006; 25:3771-3777.
8. Sumithran E, MacSween RN. An appraisal of the relationship between primary hepatocellular carcinoma and hepatitis B virus. *Histopathology* 1979; 3:447-458.
9. Blumberg BS, Alter HJ, Visnich S. Landmark article Feb 15, 1965: A "new" antigen in leukemia sera. By Baruch S. Blumberg, Harvey J. Alter, and Sam Visnich. *JAMA* 1984; 252:252-257.
10. Di Bisceglie AM. Hepatitis C and hepatocellular carcinoma. *Hepatology* 1997; 26:34S-38S.
11. Trichopoulos D, Day NE, Kaklamani E, et al. Hepatitis B virus, tobacco smoking and ethanol consumption in the etiology of hepatocellular carcinoma. *Int J Cancer* 1987; 39:45-49.
12. Block JB. Angiosarcoma of the liver following vinyl chloride exposure. *JAMA* 1974; 229:53-54.
13. Falk H, Telles NC, Ishak KG, Thomas LB, Popper H. Epidemiology of thorotrast-induced hepatic angiosarcoma in the United States. *Environ Res* 1979; 18:65-73.

14. Yachimski P, Pratt DS. Cholangiocarcinoma: natural history, treatment, and strategies for surveillance in high-risk patients. *J Clin Gastroenterol* 2008; 42:178-190.
15. Reddy KR, Schiff ER. Approach to a liver mass. *Semin Liver Dis* 1993; 13:423-435.
16. Kashef E, Roberts JP. Transplantation for hepatocellular carcinoma. *Semin Oncol* 2001; 28:497-502.
17. Strong RW. Transplantation for liver and biliary cancer. *Semin Surg Oncol* 2000; 19:189-199.
18. Hemming AW, Cattral MS, Reed AI, Van Der Werf WJ, Greig PD, Howard RJ. Liver transplantation for hepatocellular carcinoma. *Ann Surg* 2001; 233:652-659.
19. Lau WY. Primary liver tumors. *Semin Surg Oncol* 2000; 19:135-144.
20. Marsh JW, Dvorchik I, Subotin M, et al. The prediction of risk of recurrence and time to recurrence of hepatocellular carcinoma after orthotopic liver transplantation: a pilot study. *Hepatology* 1997; 26:444-450.
21. Velazquez RF, Rodriguez M, Navascues CA, et al. Prospective analysis of risk factors for hepatocellular carcinoma in patients with liver cirrhosis. *Hepatology* 2003; 37:520-527.
22. Tsukuma H, Hiyama T, Tanaka S, et al. Risk factors for hepatocellular carcinoma among patients with chronic liver disease. *N Engl J Med* 1993; 328:1797-1801.
23. Kenny-Walsh E. Clinical outcomes after hepatitis C infection from contaminated anti-D immune globulin. Irish Hepatology Research Group. *N Engl J Med* 1999; 340:1228-1233.
24. Wiese M, Grungriff K, Guthoff W, Lafrenz M, Oesen U, Porst H. Outcome in a hepatitis C (genotype 1b) single source outbreak in Germany--a 25-year multicenter study. *J Hepatol* 2005; 43:590-598.
25. Tong MJ, el Farra NS, Reikes AR, Co RL. Clinical outcomes after transfusion-associated hepatitis C. *N Engl J Med* 1995; 332:1463-1466.
26. Lee JS, Semela D, Iredale J, Shah VH. Sinusoidal remodeling and angiogenesis: a new function for the liver-specific pericyte? *Hepatology* 2007; 45:817-825.
27. Friedman SL. Molecular regulation of hepatic fibrosis, an integrated cellular response to tissue injury. *J Biol Chem* 2000; 275:2247-2250.

28. Eng FJ, Friedman SL. Fibrogenesis I. New insights into hepatic stellate cell activation: the simple becomes complex. *Am J Physiol Gastrointest Liver Physiol* 2000; 279:G7-G11.
29. Rockey DC. Hepatic blood flow regulation by stellate cells in normal and injured liver. *Semin Liver Dis* 2001; 21:337-349.
30. Marra F, Choudhury GG, Pinzani M, Abboud HE. Regulation of platelet-derived growth factor secretion and gene expression in human liver fat-storing cells. *Gastroenterology* 1994; 107:1110-1117.
31. McGuire RF, Bissell DM, Boyles J, Roll FJ. Role of extracellular matrix in regulating fenestrations of sinusoidal endothelial cells isolated from normal rat liver. *Hepatology* 1992; 15:989-997.
32. Richter S, Mucke I, Menger MD, Vollmar B. Impact of intrinsic blood flow regulation in cirrhosis: maintenance of hepatic arterial buffer response. *Am J Physiol Gastrointest Liver Physiol* 2000; 279:G454-G462.
33. Schenk WG Jr, McDonald JC, McDonald K, Drapanas T. Direct measurement of hepatic blood flow in surgical patients: with related observations on hepatic flow dynamics in experimental animals. *Ann Surg* 1962; 156:463-471.
34. Grando-Lemaire V, Guettier C, Chevret S, Beaugrand M, Trinchet JC. Hepatocellular carcinoma without cirrhosis in the West: epidemiological factors and histopathology of the non-tumorous liver. Groupe d'Etude et de Traitement du Carcinome Hepatocellulaire. *J Hepatol* 1999; 31:508-513.
35. Le Bail B, Bernard PH, Carles J, Balabaud C, Bioulac-Sage P. Prevalence of liver cell dysplasia and association with HCC in a series of 100 cirrhotic liver explants. *J Hepatol* 1997; 27:835-842.
36. Watanabe S, Okita K, Harada T, et al. Morphologic studies of the liver cell dysplasia. *Cancer* 1983; 51:2197-2205.
37. Lee RG, Tsamandas AC, Demetris AJ. Large cell change (liver cell dysplasia) and hepatocellular carcinoma in cirrhosis: matched case-control study, pathological analysis, and pathogenetic hypothesis. *Hepatology* 1997; 26:1415-1422.
38. Ferrell LD, Crawford JM, Dhillon AP, Scheuer PJ, Nakanuma Y. Proposal for standardized criteria for the diagnosis of benign, borderline, and malignant hepatocellular lesions arising in chronic advanced liver disease. *Am J Surg Pathol* 1993; 17:1113-1123.

39. Nascimento C, Bottino A, Nogueira C, Pannain V. Analysis of morphological variables and arterialization in the differential diagnosis of hepatic nodules in explanted cirrhotic livers. *Diagn Pathol* 2007; 2:51.
40. Theise ND, Park YN, Kojiro M. Dysplastic nodules and hepatocarcinogenesis. *Clin Liver Dis* 2002; 6:497-512.
41. Kojiro M, Roskams T. Early hepatocellular carcinoma and dysplastic nodules. *Semin Liver Dis* 2005; 25:133-142.
42. Nakanuma Y, Terada T, Terasaki S, et al. 'Atypical adenomatous hyperplasia' in liver cirrhosis: low-grade hepatocellular carcinoma or borderline lesion? *Histopathology* 1990; 17:27-35.
43. Park YN, Yang CP, Fernandez GJ, Cubukcu O, Thung SN, Theise ND. Neoangiogenesis and sinusoidal "capillarization" in dysplastic nodules of the liver. *Am J Surg Pathol* 1998; 22:656-662.
44. Hayashi M, Matsui O, Ueda K, et al. Correlation between the blood supply and grade of malignancy of hepatocellular nodules associated with liver cirrhosis: evaluation by CT during intraarterial injection of contrast medium. *AJR Am J Roentgenol* 1999; 172:969-976.
45. Pandharipande PV, Krinsky GA, Rusinek H, Lee VS. Perfusion imaging of the liver: current challenges and future goals. *Radiology* 2005; 234:661-673.
46. Schaffner F, Poper H. Capillarization of hepatic sinusoids in man. *Gastroenterology* 1963; 44:239-242.
47. Park YN, Chae KJ, Kim YB, Park C, Theise N. Apoptosis and proliferation in hepatocarcinogenesis related to cirrhosis. *Cancer* 2001; 92:2733-2738.
48. Tsuda H, Hirohashi S, Shimosato Y, Terada M, Hasegawa H. Clonal origin of atypical adenomatous hyperplasia of the liver and clonal identity with hepatocellular carcinoma. *Gastroenterology* 1988; 95:1664-1666.
49. Moradpour D, Blum HE. Pathogenesis of hepatocellular carcinoma. *Eur J Gastroenterol Hepatol* 2005; 17:477-483.
50. Kojiro M, Nakashima O. Histopathologic evaluation of hepatocellular carcinoma with special reference to small early stage tumors. *Semin Liver Dis* 1999; 19:287-296.
51. Carmeliet P, Jain RK. Angiogenesis in cancer and other diseases. *Nature* 2000; 407:249-257.
52. Folkman J. Tumor angiogenesis: therapeutic implications. *N Engl J Med* 1971; 285:1182-1186.

53. Vaupel P, Kallinowski F, Okunieff P. Blood flow, oxygen and nutrient supply, and metabolic microenvironment of human tumors: a review. *Cancer Res* 1989; 49:6449-6465.
54. Folkman J, Hanahan D. Switch to the angiogenic phenotype during tumorigenesis. *Princess Takamatsu Symp* 1991; 22:339-347.
55. Rak J, Mitsushashi Y, Bayko L, et al. Mutant ras oncogenes upregulate VEGF/VPF expression: implications for induction and inhibition of tumor angiogenesis. *Cancer Res* 1995; 55:4575-4580.
56. Semenza GL. Targeting HIF-1 for cancer therapy. *Nat Rev Cancer* 2003; 3:721-732.
57. Li YM, Zhou BP, Deng J, Pan Y, Hay N, Hung MC. A hypoxia-independent hypoxia-inducible factor-1 activation pathway induced by phosphatidylinositol-3 kinase/Akt in HER2 overexpressing cells. *Cancer Res* 2005; 65:3257-3263.
58. Kimura H, Braun RD, Ong ET, et al. Fluctuations in red cell flux in tumor microvessels can lead to transient hypoxia and reoxygenation in tumor parenchyma. *Cancer Res* 1996; 56:5522-5528.
59. Forsythe JA, Jiang BH, Iyer NV, et al. Activation of vascular endothelial growth factor gene transcription by hypoxia-inducible factor 1. *Mol Cell Biol* 1996; 16:4604-4613.
60. Ravi R, Mookerjee B, Bhujwala ZM, et al. Regulation of tumor angiogenesis by p53-induced degradation of hypoxia-inducible factor 1alpha. *Genes Dev* 2000; 14:34-44.
61. Burri PH, Tarek MR. A novel mechanism of capillary growth in the rat pulmonary microcirculation. *Anat Rec* 1990; 228:35-45.
62. Bergers G, Benjamin LE. Tumorigenesis and the angiogenic switch. *Nat Rev Cancer* 2003; 3:401-410.
63. Bazzoni G, Dejana E. Endothelial cell-to-cell junctions: molecular organization and role in vascular homeostasis. *Physiol Rev* 2004; 84:869-901.
64. Paku S, Paweletz N. First steps of tumor-related angiogenesis. *Lab Invest* 1991; 65:334-346.
65. Asahara T, Masuda H, Takahashi T, et al. Bone marrow origin of endothelial progenitor cells responsible for postnatal vasculogenesis in physiological and pathological neovascularization. *Circ Res* 1999; 85:221-228.
66. Jain RK. Molecular regulation of vessel maturation. *Nat Med* 2003; 9:685-693.

67. Burri PH, Hlushchuk R, Djonov V. Intussusceptive angiogenesis: its emergence, its characteristics, and its significance. *Dev Dyn* 2004; 231:474-488.
68. Djonov VG, Kurz H, Burri PH. Optimality in the developing vascular system: branching remodeling by means of intussusception as an efficient adaptation mechanism. *Dev Dyn* 2002; 224:391-402.
69. Thurston G, Suri C, Smith K, et al. Leakage-resistant blood vessels in mice transgenically overexpressing angiopoietin-1. *Science* 1999; 286:2511-2514.
70. van Royen N, Piek JJ, Buschmann I, Hofer I, Voskuil M, Schaper W. Stimulation of arteriogenesis; a new concept for the treatment of arterial occlusive disease. *Cardiovasc Res* 2001; 49:543-553.
71. Djonov V, Schmid M, Tschanz SA, Burri PH. Intussusceptive angiogenesis: its role in embryonic vascular network formation. *Circ Res* 2000; 86:286-292.
72. Djonov V, Baum O, Burri PH. Vascular remodeling by intussusceptive angiogenesis. *Cell Tissue Res* 2003; 314:107-117.
73. Marrero JA. Screening tests for hepatocellular carcinoma. *Clin Liver Dis* 2005; 9:235-51, vi.
74. Sherman M, Peltekian KM, Lee C. Screening for hepatocellular carcinoma in chronic carriers of hepatitis B virus: incidence and prevalence of hepatocellular carcinoma in a North American urban population. *Hepatology* 1995; 22:432-438.
75. Johnson PJ, Williams R. Serum alpha-fetoprotein estimations and doubling time in hepatocellular carcinoma: influence of therapy and possible value in early detection. *J Natl Cancer Inst* 1980; 64:1329-1332.
76. Zhou L, Liu J, Luo F. Serum tumor markers for detection of hepatocellular carcinoma. *World J Gastroenterol* 2006; 12:1175-1181.
77. Collier J, Sherman M. Screening for hepatocellular carcinoma. *Hepatology* 1998; 27:273-278.
78. Trojan J, Raedle J, Zeuzem S. Serum tests for diagnosis and follow-up of hepatocellular carcinoma after treatment. *Digestion* 1998; 59 Suppl 2:72-74.
79. Bruix J, Sherman M. Management of hepatocellular carcinoma. *Hepatology* 2005; 42:1208-1236.

80. Marrero JA, Hussain HK, Nghiem HV, Umar R, Fontana RJ, Lok AS. Improving the prediction of hepatocellular carcinoma in cirrhotic patients with an arterially-enhancing liver mass. *Liver Transpl* 2005; 11:281-289.
81. Hangiandreou NJ. AAPM/RSNA physics tutorial for residents. Topics in US: B-mode US: basic concepts and new technology. *Radiographics* 2003; 23:1019-1033.
82. Dodd GD, III, Miller WJ, Baron RL, Skolnick ML, Campbell WL. Detection of malignant tumors in end-stage cirrhotic livers: efficacy of sonography as a screening technique. *AJR Am J Roentgenol* 1992; 159:727-733.
83. Bennett GL, Krinsky GA, Abitbol RJ, Kim SY, Theise ND, Teperman LW. Sonographic detection of hepatocellular carcinoma and dysplastic nodules in cirrhosis: correlation of pretransplantation sonography and liver explant pathology in 200 patients. *AJR Am J Roentgenol* 2002; 179:75-80.
84. Colli A, Fraquelli M, Casazza G, et al. Accuracy of ultrasonography, spiral CT, magnetic resonance, and alpha-fetoprotein in diagnosing hepatocellular carcinoma: a systematic review. *Am J Gastroenterol* 2006; 101:513-523.
85. Kisaka Y, Hirooka M, Kumagi T, et al. Usefulness of contrast-enhanced ultrasonography with abdominal virtual ultrasonography in assessing therapeutic response in hepatocellular carcinoma treated with radiofrequency ablation. *Liver Int* 2006; 26:1241-1247.
86. Rahbin N, Siosteen AK, Elvin A, et al. Detection and characterization of focal liver lesions with contrast-enhanced ultrasonography in patients with hepatitis C-induced liver cirrhosis. *Acta Radiol* 2008; 49:251-257.
87. Takayama T, Makuuchi M, Kojiro M, et al. Early hepatocellular carcinoma: pathology, imaging, and therapy. *Ann Surg Oncol* 2008; 15:972-978.
88. Lencioni R, Piscaglia F, Bolondi L. Contrast-enhanced ultrasound in the diagnosis of hepatocellular carcinoma. *J Hepatol* 2008; 48:848-857.
89. Numata K, Tanaka K, Kiba T, et al. Correlation between hepatic tumor index on color Doppler sonography and tumor vessels on arteriography in large hepatocellular carcinomas. *Cancer Detect Prev* 1999; 23:496-505.
90. Boote EJ. AAPM/RSNA physics tutorial for residents: topics in US: Doppler US techniques: concepts of blood flow detection and flow dynamics. *Radiographics* 2003; 23:1315-1327.
91. Ando E, Kuromatsu R, Tanaka M, et al. Surveillance program for early detection of hepatocellular carcinoma in Japan: results of specialized department of liver disease. *J Clin Gastroenterol* 2006; 40:942-948.

92. Jacobs MA, Ibrahim TS, Ouwerkerk R. AAPM/RSNA physics tutorials for residents: MR imaging: brief overview and emerging applications. *Radiographics* 2007; 27:1213-1229.
93. Keogan MT, Edelman RR. Technologic advances in abdominal MR imaging. *Radiology* 2001; 220:310-320.
94. Kadoya M, Matsui O, Takashima T, Nonomura A. Hepatocellular carcinoma: correlation of MR imaging and histopathologic findings. *Radiology* 1992; 183:819-825.
95. Krinsky GA, Israel G. Nondysplastic nodules that are hyperintense on T1-weighted gradient-echo MR imaging: frequency in cirrhotic patients undergoing transplantation. *AJR Am J Roentgenol* 2003; 180:1023-1027.
96. Levenson H, Greensite F, Hoefs J, et al. Fatty infiltration of the liver: quantification with phase-contrast MR imaging at 1.5 T vs biopsy. *AJR Am J Roentgenol* 1991; 156:307-312.
97. Whitney WS, Herfkens RJ, Jeffrey RB, et al. Dynamic breath-hold multiplanar spoiled gradient-recalled MR imaging with gadolinium enhancement for differentiating hepatic hemangiomas from malignancies at 1.5 T. *Radiology* 1993; 189:863-870.
98. Oi H, Murakami T, Kim T, Matsushita M, Kishimoto H, Nakamura H. Dynamic MR imaging and early-phase helical CT for detecting small intrahepatic metastases of hepatocellular carcinoma. *AJR Am J Roentgenol* 1996; 166:369-374.
99. Larson RE, Semelka RC, Bagley AS, Molina PL, Brown ED, Lee JK. Hypervascular malignant liver lesions: comparison of various MR imaging pulse sequences and dynamic CT. *Radiology* 1994; 192:393-399.
100. Mahfouz AE, Hamm B, Taupitz M, Wolf KJ. Hypervascular liver lesions: differentiation of focal nodular hyperplasia from malignant tumors with dynamic gadolinium-enhanced MR imaging. *Radiology* 1993; 186:133-138.
101. Yoshida H, Itai Y, Ohtomo K, Kokubo T, Minami M, Yashiro N. Small hepatocellular carcinoma and cavernous hemangioma: differentiation with dynamic FLASH MR imaging with Gd-DTPA. *Radiology* 1989; 171:339-342.
102. Huppertz A, Balzer T, Blakeborough A, et al. Improved detection of focal liver lesions at MR imaging: multicenter comparison of gadoxetic acid-enhanced MR images with intraoperative findings. *Radiology* 2004; 230:266-275.

103. Pirovano G, Vanzulli A, Marti-Bonmati L, et al. Evaluation of the accuracy of gadobenate dimeglumine-enhanced MR imaging in the detection and characterization of focal liver lesions. *AJR Am J Roentgenol* 2000; 175:1111-1120.
104. Wang C, Ahlstrom H, Ekholm S, et al. Diagnostic efficacy of MnDPDP in MR imaging of the liver. A phase III multicentre study. *Acta Radiol* 1997; 38:643-649.
105. Bhartia B, Ward J, Guthrie JA, Robinson PJ. Hepatocellular carcinoma in cirrhotic livers: double-contrast thin-section MR imaging with pathologic correlation of explanted tissue. *AJR Am J Roentgenol* 2003; 180:577-584.
106. Burrel M, Llovet JM, Ayuso C, et al. MRI angiography is superior to helical CT for detection of HCC prior to liver transplantation: an explant correlation. *Hepatology* 2003; 38:1034-1042.
107. Kim YK, Kwak HS, Kim CS, Chung GH, Han YM, Lee JM. Hepatocellular carcinoma in patients with chronic liver disease: comparison of SPIO-enhanced MR imaging and 16-detector row CT. *Radiology* 2006; 238:531-541.
108. Krinsky GA, Lee VS, Theise ND, et al. Transplantation for hepatocellular carcinoma and cirrhosis: sensitivity of magnetic resonance imaging. *Liver Transpl* 2002; 8:1156-1164.
109. Teefey SA, Hildeboldt CC, Dehdashti F, et al. Detection of Primary Hepatic Malignancy in Liver Transplant Candidates: Prospective Comparison of CT, MR Imaging, US, and PET. *Radiology* 2003; 226:533-542.
110. Materne R, Smith AM, Peeters F, et al. Assessment of hepatic perfusion parameters with dynamic MRI. *Magn Reson Med* 2002; 47:135-142.
111. Koh TS, Thng CH, Lee PS, et al. Hepatic metastases: in vivo assessment of perfusion parameters at dynamic contrast-enhanced MR imaging with dual-input two-compartment tracer kinetics model. *Radiology* 2008; 249:307-320.
112. Zapletal C, Jahnke C, Mehrabi A, et al. Quantification of liver perfusion by dynamic magnetic resonance imaging: experimental evaluation and clinical pilot study. *Liver Transpl* 2009; 15:693-700.
113. Scharf J, Kemmling A, Hess T, et al. Assessment of hepatic perfusion in transplanted livers by pharmacokinetic analysis of dynamic magnetic resonance measurements. *Invest Radiol* 2007; 42:224-229.
114. Annet L, Materne R, Danse E, Jamart J, Horsmans Y, Van Beers BE. Hepatic flow parameters measured with MR imaging and Doppler US: correlations

- with degree of cirrhosis and portal hypertension. *Radiology* 2003; 229:409-414.
115. Abdullah SS, Pialat JB, Wiart M, et al. Characterization of hepatocellular carcinoma and colorectal liver metastasis by means of perfusion MRI. *J Magn Reson Imaging* 2008; 28:390-395.
 116. Hounsfield GN. Computerized transverse axial scanning (tomography): Part I. Description of system. 1973. *Br J Radiol* 1995; 68:H166-H172.
 117. Goldman LW. Principles of CT and CT technology. *J Nucl Med Technol* 2007; 35:115-128.
 118. Bhosale P, Szklaruk J, Silverman PM. Current staging of hepatocellular carcinoma: imaging implications. *Cancer Imaging* 2006; 6:83-94.
 119. Saab S, Ly D, Nieto J, et al. Hepatocellular carcinoma screening in patients waiting for liver transplantation: a decision analytic model. *Liver Transpl* 2003; 9:672-681.
 120. Brancatelli G, Federle MP, Grazioli L, Carr BI. Hepatocellular carcinoma in noncirrhotic liver: CT, clinical, and pathologic findings in 39 U.S. residents. *Radiology* 2002; 222:89-94.
 121. Yamashita Y, Takahashi M, Baba Y, et al. Hepatocellular carcinoma with or without cirrhosis: a comparison of CT and angiographic presentations in the United States and Japan. *Abdom Imaging* 1993; 18:168-175.
 122. Kamel IR, Bluemke DA. Imaging evaluation of hepatocellular carcinoma. *J Vasc Interv Radiol* 2002; 13:S173-S184.
 123. Murakami T, Kim T, Takahashi S, Nakamura H. Hepatocellular carcinoma: multidetector row helical CT. *Abdom Imaging* 2002; 27:139-146.
 124. Murakami T, Kim T, Takamura M, et al. Hypervascular hepatocellular carcinoma: detection with double arterial phase multi-detector row helical CT. *Radiology* 2001; 218:763-767.
 125. Murakami T, Kim T, Kawata S, et al. Evaluation of optimal timing of arterial phase imaging for the detection of hypervascular hepatocellular carcinoma by using triple arterial phase imaging with multidetector-row helical computed tomography. *Invest Radiol* 2003; 38:497-503.
 126. Lim JH, Kim CK, Lee WJ, et al. Detection of hepatocellular carcinomas and dysplastic nodules in cirrhotic livers: accuracy of helical CT in transplant patients. *AJR Am J Roentgenol* 2000; 175:693-698.

127. Peterson MS, Baron RL, Marsh JW, Jr., Oliver JH, III, Confer SR, Hunt LE. Pretransplantation surveillance for possible hepatocellular carcinoma in patients with cirrhosis: epidemiology and CT-based tumor detection rate in 430 cases with surgical pathologic correlation. *Radiology* 2000; 217:743-749.
128. Valls C, Cos M, Figueras J, et al. Pretransplantation diagnosis and staging of hepatocellular carcinoma in patients with cirrhosis: value of dual-phase helical CT. *AJR Am J Roentgenol* 2004; 182:1011-1017.
129. Sharma RM, Sharma C, Donnelly AJ, Morris HP, Weinhouse S. Glucose-ATP phosphotransferases during hepatocarcinogenesis. *Cancer Res* 1965; 25:193-199.
130. Khan MA, Combs CS, Brunt EM, et al. Positron emission tomography scanning in the evaluation of hepatocellular carcinoma. *J Hepatol* 2000; 32:792-797.
131. Trojan J, Schroeder O, Raedle J, et al. Fluorine-18 FDG positron emission tomography for imaging of hepatocellular carcinoma. *Am J Gastroenterol* 1999; 94:3314-3319.
132. Huebner RH, Park KC, Shepherd JE, et al. A meta-analysis of the literature for whole-body FDG PET detection of recurrent colorectal cancer. *J Nucl Med* 2000; 41:1177-1189.
133. Munk OL, Bass L, Feng H, Keiding S. Determination of regional flow by use of intravascular PET tracers: microvascular theory and experimental validation for pig livers. *J Nucl Med* 2003; 44:1862-1870.
134. Ziegler SI, Haberkorn U, Byrne H, et al. Measurement of liver blood flow using oxygen-15 labelled water and dynamic positron emission tomography: limitations of model description. *Eur J Nucl Med* 1996; 23:169-177.
135. Taniguchi H, Oguro A, Koyama H, Masuyama M, Takahashi T. Analysis of models for quantification of arterial and portal blood flow in the human liver using PET. *J Comput Assist Tomogr* 1996; 20:135-144.
136. Chen BC, Huang SC, Germano G, et al. Noninvasive quantification of hepatic arterial blood flow with nitrogen-13-ammonia and dynamic positron emission tomography. *J Nucl Med* 1991; 32:2199-2206.
137. Koh T, Taniguchi H, Yamagishi H. Oxygen-15 positron-emission tomography for predicting selective delivery of a chemotherapeutic agent to hepatic cancers during angiotensin II-induced hypertension. *Cancer Chemother Pharmacol* 2003; 51:349-358.

138. Fukuda KI, Taniguchi H, Koh T, Kunishima S, Yamagishi H. Relationships between oxygen and glucose metabolism in human liver tumours: positron emission tomography using ¹⁵O and ¹⁸F-deoxyglucose. *Nucl Med Commun* 2004; 25:577-583.
139. Llovet JM, Fuster J, Bruix J. Intention-to-treat analysis of surgical treatment for early hepatocellular carcinoma: resection versus transplantation. *Hepatology* 1999; 30:1434-1440.
140. Minagawa M, Makuuchi M, Takayama T, Kokudo N. Selection criteria for repeat hepatectomy in patients with recurrent hepatocellular carcinoma. *Ann Surg* 2003; 238:703-710.
141. Okada S, Shimada K, Yamamoto J, et al. Predictive factors for postoperative recurrence of hepatocellular carcinoma. *Gastroenterology* 1994; 106:1618-1624.
142. Mazzaferro V, Regalia E, Doci R, et al. Liver transplantation for the treatment of small hepatocellular carcinomas in patients with cirrhosis. *N Engl J Med* 1996; 334:693-699.
143. Bismuth H, Majno PE, Adam R. Liver transplantation for hepatocellular carcinoma. *Semin Liver Dis* 1999; 19:311-322.
144. Jonas S, Bechstein WO, Steinmuller T, et al. Vascular invasion and histopathologic grading determine outcome after liver transplantation for hepatocellular carcinoma in cirrhosis. *Hepatology* 2001; 33:1080-1086.
145. Bruix J, Llovet JM. Prognostic prediction and treatment strategy in hepatocellular carcinoma. *Hepatology* 2002; 35:519-524.
146. Llovet JM, Real MI, Montana X, et al. Arterial embolisation or chemoembolisation versus symptomatic treatment in patients with unresectable hepatocellular carcinoma: a randomised controlled trial. *Lancet* 2002; 359:1734-1739.
147. Hussain SA, Ferry DR, El Gazzaz G, et al. Hepatocellular carcinoma. *Ann Oncol* 2001; 12:161-172.
148. Hawkins MA, Dawson LA. Radiation therapy for hepatocellular carcinoma: from palliation to cure. *Cancer* 2006; 106:1653-1663.
149. Cao Y, Platt JF, Francis IR, et al. The prediction of radiation-induced liver dysfunction using a local dose and regional venous perfusion model. *Med Phys* 2007; 34:604-612.
150. D'Amato RJ, Loughnan MS, Flynn E, Folkman J. Thalidomide is an inhibitor of angiogenesis. *Proc Natl Acad Sci U S A* 1994; 91:4082-4085.

151. Kruse FE, Jousseaume AM, Rohrschneider K, Becker MD, Volcker HE. Thalidomide inhibits corneal angiogenesis induced by vascular endothelial growth factor. *Graefes Arch Clin Exp Ophthalmol* 1998; 236:461-466.
152. Patt YZ, Hassan MM, Lozano RD, Ellis LM, Peterson JA, Waugh KA. Durable clinical response of refractory hepatocellular carcinoma to orally administered thalidomide. *Am J Clin Oncol* 2000; 23:319-321.
153. Gasparini G, Longo R, Fanelli M, Teicher BA. Combination of antiangiogenic therapy with other anticancer therapies: results, challenges, and open questions. *J Clin Oncol* 2005; 23:1295-1311.
154. Ansiaux R, Baudelet C, Jordan BF, et al. Thalidomide radiosensitizes tumors through early changes in the tumor microenvironment. *Clin Cancer Res* 2005; 11:743-750.
155. Hurwitz HI, Fehrenbacher L, Hainsworth JD, et al. Bevacizumab in combination with fluorouracil and leucovorin: an active regimen for first-line metastatic colorectal cancer. *J Clin Oncol* 2005; 23:3502-3508.
156. Lee CG, Heijn M, di Tomaso E, et al. Anti-Vascular endothelial growth factor treatment augments tumor radiation response under normoxic or hypoxic conditions. *Cancer Res* 2000; 60:5565-5570.
157. Teicher BA, Holden SA, Ara G, et al. Influence of an anti-angiogenic treatment on 9L gliosarcoma: oxygenation and response to cytotoxic therapy. *Int J Cancer* 1995; 61:732-737.
158. Ansiaux R, Baudelet C, Jordan BF, et al. Mechanism of Reoxygenation after Antiangiogenic Therapy Using SU5416 and Its Importance for Guiding Combined Antitumor Therapy. *Cancer Res* 2006; 66:9698-9704.
159. Jain RK. Normalizing tumor vasculature with anti-angiogenic therapy: a new paradigm for combination therapy. *Nat Med* 2001; 7:987-989.
160. Lin MI, Sessa WC. Antiangiogenic therapy: creating a unique "window" of opportunity. *Cancer Cell* 2004; 6:529-531.
161. Fan ZH, Chen MH, Dai Y, et al. Evaluation of primary malignancies of the liver using contrast-enhanced sonography: correlation with pathology. *AJR Am J Roentgenol* 2006; 186:1512-1519.
162. Hanna RF, Kased N, Kwan SW, et al. Double-contrast MRI for accurate staging of hepatocellular carcinoma in patients with cirrhosis. *AJR Am J Roentgenol* 2008; 190:47-57.

163. Ebied OM, Federle MP, Carr BI, et al. Evaluation of responses to chemoembolization in patients with unresectable hepatocellular carcinoma. *Cancer* 2003; 97:1042-1050.
164. Miles KA. Perfusion CT for the assessment of tumour vascularity: which protocol? *Br J Radiol* 2003; 76 Spec No 1:S36-S42.
165. Crone C. The Permeability of Capillaries in various Organs as determined by use of the 'indicator diffusion' Method. *Acta Physiol Scand* 1963; 58:292-305.
166. Materne R, Van Beers BE, Smith AM, et al. Non-invasive quantification of liver perfusion with dynamic computed tomography and a dual-input one-compartmental model. *Clin Sci (Lond)* 2000; 99:517-525.
167. Goresky CA. A linear method for determining liver sinusoidal and extravascular volumes. *Am J Physiol* 1963; 204:626-640.
168. Martinez-Hernandez A, Martinez J. The role of capillarization in hepatic failure: studies in carbon tetrachloride-induced cirrhosis. *Hepatology* 1991; 14:864-874.
169. Larson KB, Markham J, Raichle ME. Tracer-kinetic models for measuring cerebral blood flow using externally detected radiotracers. *J Cereb Blood Flow Metab* 1987; 7:443-463.
170. Johnson JA, Wilson TA. A model for capillary exchange. *Am J Physiol* 1966; 210:1299-1303.
171. Cao Y, Alspaugh J, Shen Z, Balter JM, Lawrence TS, Ten Haken RK. A practical approach for quantitative estimates of voxel-by-voxel liver perfusion using DCE imaging and a compartmental model. *Med Phys* 2006; 33:3057-3062.
172. Cuenod C, Leconte I, Siauve N, et al. Early changes in liver perfusion caused by occult metastases in rats: detection with quantitative CT. *Radiology* 2001; 218:556-561.
173. Miles KA, Hayball MP, Dixon AK. Functional images of hepatic perfusion obtained with dynamic CT. *Radiology* 1993; 188:405-411.
174. St Lawrence KS, Lee TY. An adiabatic approximation to the tissue homogeneity model for water exchange in the brain: I. Theoretical derivation. *J Cereb Blood Flow Metab* 1998; 18:1365-1377.
175. Cenic A, Nabavi DG, Craen RA, Gelb AW, Lee TY. A CT method to measure hemodynamics in brain tumors: validation and application of cerebral blood flow maps. *AJNR Am J Neuroradiol* 2000; 21:462-470.

176. Bassingthwaite JB, Knopp TJ, Anderson DU. Flow estimation by indicator dilution (bolus injection). *Circ Res* 1970; 27:277-29

CHAPTER 2: HEPATIC PERFUSION IN A TUMOR MODEL USING DCE-CT: A ACCURACY AND PRECISION STUDY

The content of this chapter have been adapted from the paper entitled “Hepatic perfusion in a tumor model using DCE-CT: A accuracy and precision study”, published in the journal *Physics in Medicine and Biology* vol. 53 (16): pp. 4249 – 4267 (2008) by Errol E. Stewart, Xiaogang Chen, Jennifer A. Hadway, Ting-Yim Lee.

2.1 INTRODUCTION

Alterations in liver blood flow may distinguish among different stages of liver disease and can be used to monitor response to treatment (1). The liver receives blood from the hepatic artery delivering oxygenated blood from the heart and the portal vein draining blood from the gastrointestinal tract. The dual system of blood supply gives rise to the hepatic arterial buffer response, which maintains total hepatic blood flow (H_TBF) at a constant level despite portal venous blood flow (P_VBF) alterations (2). In the liver the progression from cirrhosis to dysplastic nodules to hepatocellular carcinoma (HCC) is characterized by a shift from a predominantly venous to an arterial blood supply (3). Hepatic arterial blood flow (H_ABF) is a more relevant physiological parameter to liver function and disease than H_TBF , because it more accurately reflects the adaptive response in the liver to injury, regeneration, and the development of malignancy (4-6). Furthermore, Kobayashi *et al.* demonstrated that a reduction in P_VBF is an important predictor of HCC development (7). Hence, knowledge of H_ABF and H_TBF is important for the accurate diagnosis of liver tumor from benign lesions.

A number of in-vivo dynamic contrast-enhanced (DCE) Computed Tomography (CT) methods have been developed to measure H_ABF (8-12). Miles *et al.* used the Fick Principle with the assumption that there is no venous outflow of contrast agent such that tissue blood flow can be calculated as the ratio of the maximum initial slope of the tissue time-enhancement curve to the peak height of the arterial time-enhancement curve (11). However, the assumption of no venous outflow at the time of the maximum initial slope of the tissue time-enhancement curve may not always be correct (13). Other investigators have used a two compartmental model with dual contrast input from hepatic artery and portal vein to measure liver blood flow (8-10). Materne *et al.* validated the compartmental DCE-CT measurements of liver blood flow in normal liver against *ex-vivo* radiolabelled microsphere measurements (10). The compartmental model estimates the product of flow (both hepatic arterial and portal venous) and the extraction fraction (E) of contrast agent in the liver; to arrive at flow, it is necessary to assume that E is equal to one (10). This assumption may be correct in the normal liver because the liver sinusoids are fenestrated, allowing contrast molecules to diffuse freely into the extravascular space of Disse (14). However, capillarization of liver sinusoids is common in regeneration (15), which may reduce extraction efficiency of contrast agent heterogeneously in the affected liver parenchyma. We have used the Johnson and Wilson model (16), which assumes a concentration gradient of contrast from the arterial to the venous end as blood carrying contrast travels down the length of capillaries. One advantage of the Johnson and Wilson model is that it allows for the separate estimation of flow (H_ABF and H_TBF), E (sinusoid permeability surface area product) and total hepatic blood volume (H_TBV) from a single CT study (12). The accuracy and precision of

hepatic tissue perfusion measurements based on the Johnson and Wilson model with the adiabatic approximation have not been reported (17). The purpose of our study is to determine the accuracy and precision of hepatic perfusion measurements with this model.

2.2 MATERIALS AND METHODS

2.2.1 Study Protocol

Twelve New Zealand white rabbits (3.1 – 3.4 kg) were used in these experiments. The experimental procedures were approved by the local animal use subcommittee of the Canadian Council on Animal Care. To induce growth of liver tumor, VX2 carcinoma cells from donor rabbits were injected directly into the liver of the rabbits (12). Following implantation of the tumor cells, DCE-CT scans were performed every 4 days to monitor for the development of tumor. Day 0 was set at the time when a tumor was detected by DCE-CT (approximate 0.7 ± 0.1 cm diameter). Physiological parameters, including partial arterial carbon dioxide tension (P_aCO_2) and pH (ABL 500, Radiometer Copenhagen, Denmark) were monitored and maintained at normal levels unless otherwise specified throughout the experiments. The animal's body temperature was maintained between 38.5 and 39.5°C with a heated re-circulating water blanket.

2.2.2 Surgical Preparation

Anesthesia was induced via a mask at approximately 2.5 minimum alveolar concentrations (MAC) of isoflurane (the MAC levels were estimated from (18) where 2 % isoflurane in rabbit is equivalent to 1 MAC). One ear vein was cannulated for drugs and contrast injection (Omnipaque 300 diluted to 200 mg iodine ml^{-1} ; GE Healthcare,

Wisconsin, USA). A cuffed endotracheal tube was inserted and inflated; anesthesia was maintained by mechanical ventilation at a rate of 20 breaths per min with a mixture of oxygen and 1.5 MAC isoflurane. For the accuracy study, the isoflurane level was increased to 2.5 MAC and the chest wall of the rabbit was open to expose the heart and closed after insertion of a catheter into the left atrial appendage for injection of microspheres. Another catheter was placed in the right femoral artery for blood gas and hematocrit determination, monitoring of mean arterial pressure (MAP) and heart rate (HR) and blood withdrawal for the microsphere experiment. Isoflurane level was reduced to 1.5 MAC and respiratory reflex was suppressed with pancuronium bromide if required. At the end of the study the animals were sacrificed by an overdose of potassium chloride.

2.2.3 DCE-CT Scanning Protocol

CT scanning was performed with a LightSpeed CT scanner (GE Healthcare) following stabilization of HR, MAP and blood gas parameters. After locating the liver with a localizer, four 5 mm thick slices covering the liver were scanned with a two-phase protocol as describe by Stewart *et al.* (12). The scan parameters for both phases were 120 kVp, 60 mA, and 1 s per rotation. During the 1st phase, the liver was continuously scanned for 30 s with injection of a bolus of non-ionic contrast agent (Omnipaque 300 (GE Healthcare) diluted to 200 mg iodine ml⁻¹ and a dose of 1.5 ml kg⁻¹) at a rate of 1ml s⁻¹. Prior to injection, ventilation was suspended to eliminate motion from breathing. During the 2nd phase the ventilator was set to a breathing rate of 20 breaths per min and a 4.0 s burst of a continuous scan was performed every 10 s for a period of 2 min.

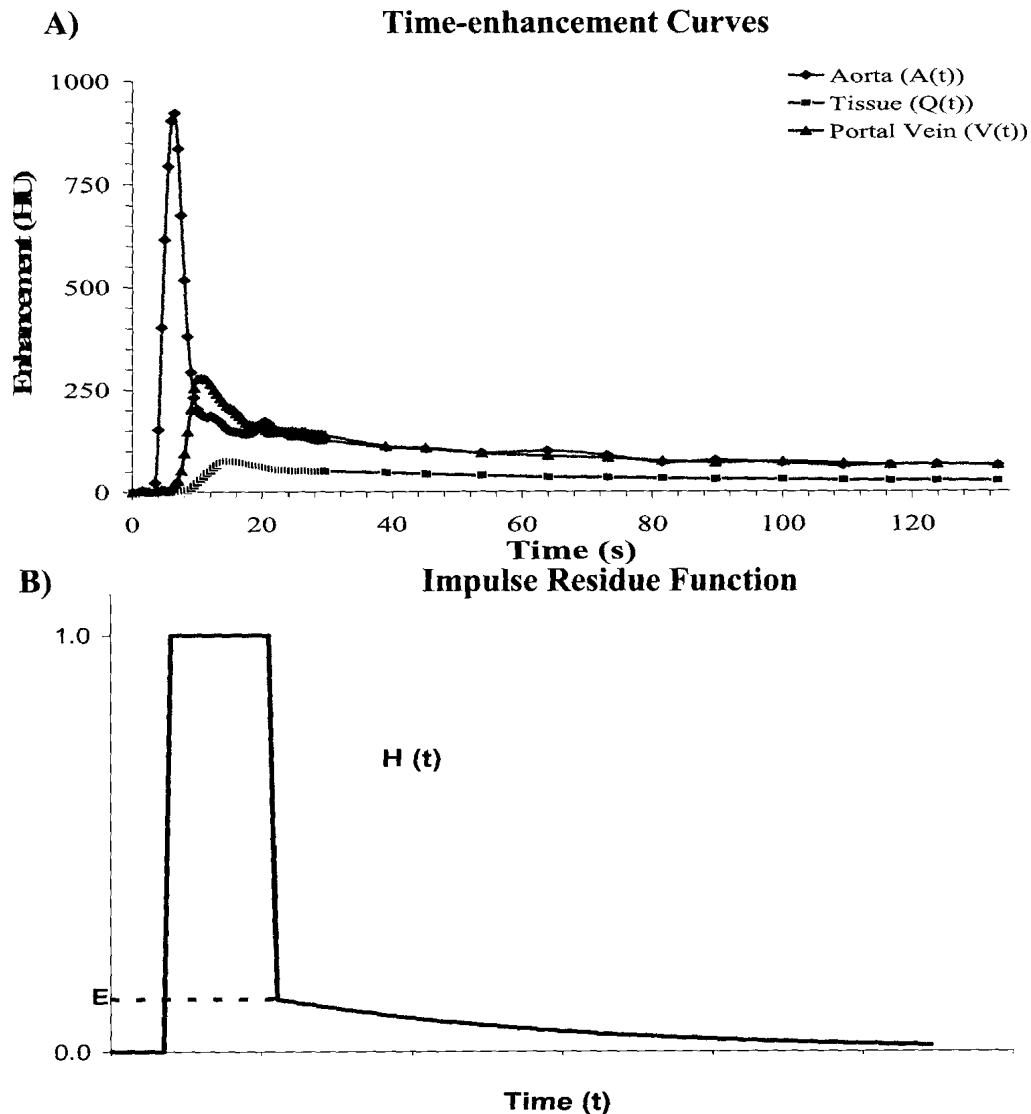
2.2.4 Precision Study

Five rabbits were used for the precision studies. For each rabbit, the first precision study was performed 12 days after the initial detection of the liver tumor. The study consisted of two DCE-CT scans performed 15 min apart to measure $H_{\Delta}BF$ (1st and 2nd measurements) under normal conditions ($PaCO_2$ of 39 ± 2 mmHg, temperature of 39.0 ± 0.1 °C and, pH of 7.46 ± 0.01) using the scanning protocol described above. The animal was allowed to recover and a second precision study was performed four days later in the same manner as the first study.

2.2.5 Calculation of Parametric Maps

Images from both phases of the DCE-CT study were co-registered to remove breathing motion using the CT Perfusion 4.0 software (GE Healthcare). At each slice location a region was drawn to outline the liver in the CT images from the 1st phase of the scanning protocol. Each scan burst in the 2nd phase captured a complete breathing cycle and produced 16 images per slice. The image from each 2nd phase scan burst that best matched the outlined liver region from the 1st phase at each slice location was selected manually. The co-registration process required less than 10 minutes and the breathing motion of the liver can be largely eliminated as evidenced by the smooth appearance of the time-enhancement curves shown in Figure 2.1(A).

Figure 2.1: Time enhancement curves and IRF

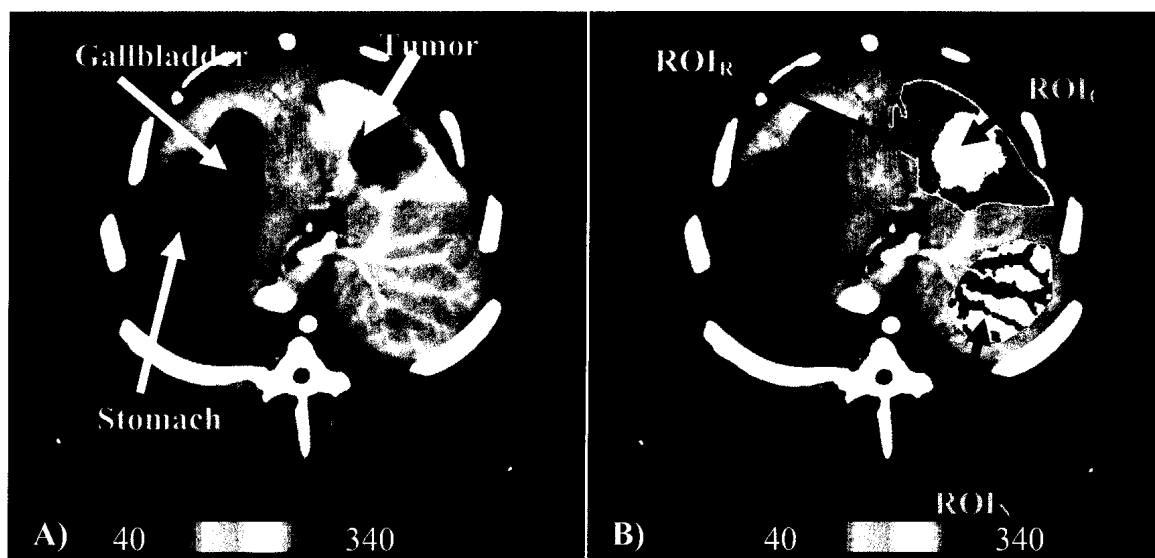


Time-enhancement curves from the aorta, the portal vein and liver parenchyma of a rabbit and the derived impulse residue function. **A)** Aorta (diamond), portal vein (triangle), and normal liver parenchyma (square) time-enhancement curves as measured by a CT scanner following intravenous injection of contrast. The curves were measured from the co-registered 1st and 2nd phase CT images and were deconvolved to calculate **B)** the impulse residue function ($H(t)$) according to the Johnson-Wilson model as explained in the Appendix B. The first part of $H(t)$, a rectangular function, shows the intravascular passage of contrast media through the tissue (vascular phase). The second part of the curve, a slowly decaying mono-exponential function, represents the diffusion of extracted

contrast media in the extravascular space of liver parenchyma into the vascular space to be cleared by blood flow (interstitial phase). The extraction fraction, E , is the ratio of the initial point of the second phase to the plateau height of the first phase. From the derived $H(t)$, the set of functional parameters: H_TBF , H_TBV , PS , and H_{ABF} can be calculated according to Equations (B.1) to (B.4) in the Appendix B.

The Johnson and Wilson model with the adiabatic approximation was used to account for the distribution of contrast in the liver as well as for the liver's dual inputs of contrast from the hepatic artery and the portal vein (12). Time-enhancement curves from the aorta ($A(t)$), portal vein ($V(t)$) and liver or tumor ($Q(t)$) were obtained from images of the co-registered phases, Figure 2.1(A). Deconvolution of $Q(t)$ from each voxel with a weighted summation ($C_a(t)$) of the $A(t)$ and $V(t)$ generated the following five parametric maps according to equ (B.1) to (B.4) in Appendix B: H_TBF ; hepatic arterial fraction (α); permeability surface area product (PS); H_{ABF} as the product of α and H_TBF ; and, H_TBV as $F \cdot T_c$ according to the Central Volume Principle (19). Glossary gives the units of the perfusion parameters. A sixth parametric map, perfusion-weighted (PW) map, was produced by averaging all images over the duration of the 1st phase of the scanning protocol, Figure 2.2(A).

Figure 2.2: Perfusion Weighted Map



A) The perfusion-weighted image was created by averaging cine images over the duration of the 1st phase of the scanning protocol since concentration of contrast in the blood vessels and tumor rim was highest during the first 30 s of scanning. **B)** The averaging of these images increases the SNR in the image by a factor of 7.7, and allow for the delineation of the tumor rim (ROI_R) from the tumor core (ROI_C), and; the exclusion of the blood vessels (green) from the normal tissue (ROI_N).

2.2.6 Accuracy Study

H_ABF measured with DCE-CT was compared against that measured using the *ex vivo* method of radiolabelled microsphere technique in seven animals 16 days post tumor detection (20). To achieve a range in H_ABF three arterial P_aCO₂ levels: normo-, hyper- and hypo-capnia were used. Radiolabelled microspheres (15 μm diameter, 1×10⁶ microspheres in 0.25 ml) was flushed into the left atrium with 3.7 ml of saline simultaneously with an intravenous injection of contrast for the DCE-CT scan. A different radiolabelled microsphere from a collection of four: strontium-85, cerium-141,

scandium-46, and niobium-95 (PerkinElmer, Massachusetts, USA) was chosen at random for each capnic level. Blood was withdrawn from the femoral artery catheter for 4 min, starting 1 min before the microspheres injection. At the end of blood withdrawal, the liver was removed, fixed in formalin for 24 hours before being sectioned into 5 mm thick slices to match those of the DCE-CT study. For each liver slice the normal tissue, tumor rim and core were collected into 0.5 ± 0.14 g samples to match their appearance in the PW map as described in the Data Analysis section. The activity of each sample, blood or tissue, was measured with an automated gamma ray spectrometer/counter (DSPEC; Ortec, Tennessee, USA). $H_A BF$ was calculated for each tissue sample using the equation:

$$H_A BF = \frac{N_t B_w}{R} \quad (2.1)$$

where $H_A BF$ is blood flow in a tissue sample ($\text{ml} \cdot \text{min}^{-1} \cdot (100 \text{ g})^{-1}$), N_t is the activity of the tissue sample normalized to 100 g, B_w is the rate of blood withdrawal ($1 \text{ ml} \cdot \text{min}^{-1}$) and R is the activity in the volume of blood extracted.

2.2.7 Data Analysis

All parametric maps were imported into custom software (IDL v6.0; RSI Inc., Colorado, USA) for analysis. In the PW map of each slice a region of interest (ROI) was drawn on the adjacent normal tissue (ROI_N) avoiding the portal vein and the hepatic artery. The tumor core appears hypo-enhanced in the PW map, with the mean Hounsfield Unit (HU) at least one standard deviation lower than the mean in the tumor rim, Figure 2.2 (A). Base on this difference in HU, the tumor rim can be segmented automatically from the tumor core, Figure 2.2 (B). The resulting tumor rim (ROI_R) and tumor core (ROI_C) mask were applied to all available parametric maps to obtain values in both the

accuracy and precision study. In the accuracy study the assigned regions were also used as templates to section the microsphere imbedded liver tissue into the three tissue types.

2.2.8 Monte Carlo Simulation

Monte Carlo simulations were used to determine the reliability of parameter estimates. The simulations were performed using procedures described by St Lawrence and Lee (21). The simulation was performed using parameter values that represent the normal tissue, tumor rim and core obtained under normal condition of the accuracy study. The background subtracted arterial and portal vein curves from a rabbit study together with known parameter values of our liver perfusion model (F , T_0 , T_c , PS and α) were used to generate tissue curves according to equations (A.1) to (A.4) and then a range of Gaussian noise was added to the tissue curves using the Monte Carlo method. The signal-to-noise ratio (SNR) in the simulated tissue curve was defined as the maximum enhancement (signal) in the simulated tissue curves divided by the standard deviation (SD) of the Gaussian distribution used to generate noise. Estimates of model parameters derived from the deconvolution of the simulated tissue curves with respect to the assumed arterial and portal vein curve were compared to their true values to calculate the coefficient of variation (CV) of the parameter estimates.

2.2.9 Statistical Analysis

Precision was investigated by a three-way analysis of variance (ANOVA). Precision was measured by the CV derived from the ANOVA (22) and the Bland-Altman plot was used to assess bias (23). To determine accuracy a three-way ANOVA and post-

hoc paired t-test with Bonferroni correction was used to compare DCE-CT and microsphere H_{ABF} . The Bland-Altman plot was also used to assess the agreement between the two methods (23). All normally distributed data was reported as mean \pm standard error, and significance was set at $P < 0.05$.

To account for multiple measurements in the same rabbit, the generalized estimating equation (GEE) method was used instead of a regular regression analysis (24). First, a linear regression was applied to the data from each rabbit individually. Second, correlation between DCE-CT and microsphere H_{ABF} , or repeated measurements in the precision study were tested using a t-test to compare the mean of the distribution of slopes against zero (the null hypothesis). The null hypothesis is rejected if the slope is significantly different from zero. Finally, the mean slope was compared with a slope of unity. All statistical tests were performed using the SPSS software version 15.0 (SPSS Inc; Illinois, USA).

2.3 RESULTS

The P_aCO_2 levels achieved under steady state normo-, hyper- and hypo-capnia were 39.4 ± 0.6 , 62.3 ± 2.5 and 27.4 ± 0.8 mmHg respectively, Table 2.1. An ANOVA showed significant P_aCO_2 differences among the three capnic levels, $P < 0.05$. Similarly, there were significant differences among the corresponding arterial pH under the three capnic levels: 7.43 ± 0.02 , 7.28 ± 0.03 and 7.54 ± 0.03 , respectively, $P < 0.05$. The MAP under hyper-capnia was significantly different from normo- and hypo-capnic conditions, $P <$

0.05. The heart rate and hematocrit remained constant at $264 \pm 8 \text{ min}^{-1}$ and $34.8 \pm 0.8 \%$, respectively under the three capnic levels.

Table 2.1: Physiological parameters at different capnic levels

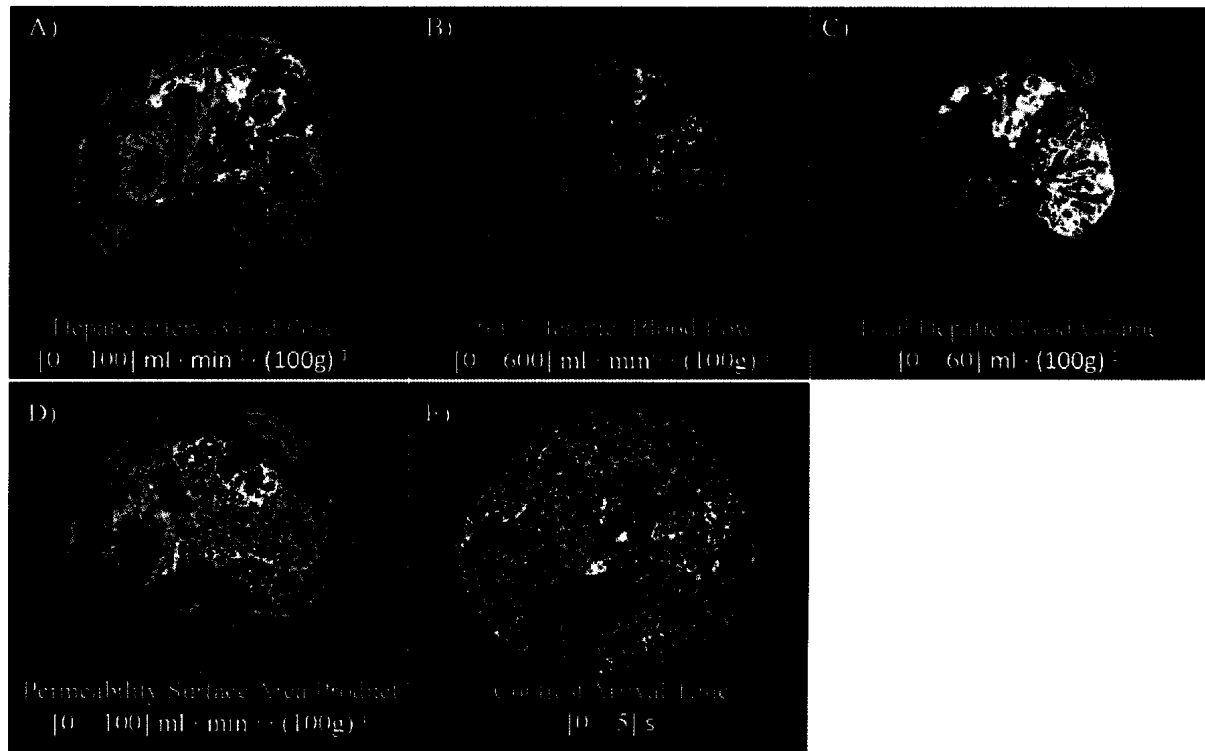
	Normo-capnia	Hyper-capnia	Hypo-capnia
$P_a\text{CO}_2$ (mmHg)	$39.4 \pm 0.6^*$	$62.4 \pm 2.5^*$	$27.4 \pm 0.8^*$
Heart Rate (min^{-1})	271 ± 9	259 ± 8	261 ± 7
pH_a	$7.43 \pm 0.02^*$	$7.28 \pm 0.03^*$	$7.54 \pm 0.03^*$
MAP (mmHg)	46 ± 2	$55 \pm 3^*$	44 ± 2
Hematocrit (%)	34.9 ± 0.8	34.9 ± 0.8	34.4 ± 0.8

$P_a\text{CO}_2$ = arterial partial carbon dioxide tension; pH_a = arterial pH; MAP = mean arterial blood pressure. * indicates measurement significantly different ($P < 0.05$) from that at other capnic levels: normo-capnia, hyper-capnia, or hypo-capnia.

Example parametric maps for $H_A\text{BF}$, $H_T\text{BF}$, $H_T\text{BV}$, PS and T_0 are shown in Figure 2.3. Under steady state normo-capnic condition the microsphere $H_A\text{BF}$ were: 51.9 ± 4.2 , 40.7 ± 4.9 and $99.7 \pm 6.0 \text{ ml}\cdot\text{min}^{-1}\cdot(100 \text{ g})^{-1}$ while DCE-CT $H_A\text{BF}$ were: 50.0 ± 5.7 , 37.1 ± 4.5 and $99.8 \pm 6.8 \text{ ml}\cdot\text{min}^{-1}\cdot(100 \text{ g})^{-1}$ in normal liver, tumor core and rim respectively, Table 2.2. For all capnic levels, $H_A\text{BF}$ measured with both techniques showed significant difference amongst all three tissue types, $P < 0.05$. Similarly, measurements of $H_T\text{BF}$, PS and α showed significant difference amongst all three tissue types, $P < 0.05$; whereas, $H_T\text{BV}$ showed significantly difference only between the tumor core and the other tissues at all capnic levels, $P < 0.05$, Table 2.2. The effect of varying the capnic level on perfusion related parameters were examined in Table 2.2. An ANOVA showed that there were no differences between perfusion parameters measured during steady state normo-

and hyper-capnic conditions, $P > 0.05$, Table 2.2. For all tissues H_ABF measured under steady state hypo-capnia were significantly different from those under steady state normo- and hyper-capnia, $P < 0.05$, Table 2.2.

Figure 2.3: DCE-CT perfusion maps



Parametric maps of the liver generated under normo-capnia from the same rabbit study as in Figure 2.2. **A)** Hepatic artery blood flow (H_ABF) map. **B)** Total hepatic blood flow (H_TBF) map. **C)** Total hepatic blood volume (H_TBV) map. **D)** Permeability surface area (PS) map. **E)** Contrast arrival time (T_0) map. The tumor is visible in all of the maps. However, the H_ABF map delineates the tumor rim from the tumor core most clearly. It also suggests that the tumor has increased arterial blood supply than normal liver.

Table 2.2: Hepatic perfusion measured with DCE-CT and microsphere under three capnic levels in the normal tissue

A)	Normal Tissue		
	<i>Normo-capnia</i>	<i>Hyper-capnia</i>	<i>Hypo-capnia</i>
Microsphere			
$H_A BF$ (ml · min ⁻¹ · (100g) ⁻¹) δ	51.9 ± 4.2	56.1 ± 9.4	28.0 ± 1.3*
DCE-CT Parameters			
$H_A BF$ (ml · min ⁻¹ · (100g) ⁻¹) δ	50.0 ± 5.7	48.7 ± 4.1	28.6 ± 3.6*
$H_T BF$ (ml · min ⁻¹ · (100g) ⁻¹) δ	224 ± 16	216 ± 11	190.1 ± 9.8
$H_T BV$ (ml · (100g) ⁻¹) ξ	22.5 ± 1.4	24.3 ± 1.0	20.51 ± 0.85Φ
PS (ml · min ⁻¹ · (100g) ⁻¹) δ	45.1 ± 4.5	41.3 ± 6.1	50.9 ± 5.4
α (%) δ	23.5 ± 3.4	21.9 ± 1.5	15.3 ± 1.3†
B)			
	Tumor Core		
	<i>Normo-capnia</i>	<i>Hyper-capnia</i>	<i>Hypo-capnia</i>
Microsphere			
$H_A BF$ (ml · min ⁻¹ · (100g) ⁻¹) δ	40.7 ± 4.9	38.4 ± 4.5	26.9 ± 4.5†
DCE-CT Parameters			
$H_A BF$ (ml · min ⁻¹ · (100g) ⁻¹) δ	37.1 ± 4.5	33.9 ± 3.7	26.0 ± 3.1†
$H_T BF$ (ml · min ⁻¹ · (100g) ⁻¹) δ	67.3 ± 8.7	69 ± 15	77 ± 12
$H_T BV$ (ml · (100g) ⁻¹) δ	7.1 ± 2.0	7.7 ± 3.1	6.9 ± 1.3
PS (ml · min ⁻¹ · (100g) ⁻¹) δ	25.8 ± 3.4	24.1 ± 3.1	36.4 ± 7.6
α (%) δ	56.1 ± 4.9	53 ± 10	35.3 ± 4.0

C)	Tumor Rim		
	<i>Normo-capnia</i>	<i>Hyper-capnia</i>	<i>Hypo-capnia</i>
Microsphere			
H_{ABF} (ml · min ⁻¹ · (100g) ⁻¹) δ	99.7 ± 6.0	97 ± 12	53.8 ± 4.9*
DCE-CT Parameters			
H_{ABF} (ml · min ⁻¹ · (100g) ⁻¹) δ	99.8 ± 6.8	100.0 ± 5.7	74.2 ± 6.2*
H_{TBF} (ml · min ⁻¹ · (100g) ⁻¹) δ	330 ± 29	347 ± 28	243 ± 26
H_{TBV} (ml · (100g) ⁻¹) ξ	26.0 ± 1.4	26.1 ± 2.5	20.4 ± 1.6
PS (ml · min ⁻¹ · (100g) ⁻¹) δ	55.9 ± 5.3	65.0 ± 8.6	55.0 ± 8.0
α (%) δ	31.3 ± 1.9	29.6 ± 2.2	29.6 ± 1.6

All data was reported as mean ± standard error.

H_{ABF} = hepatic arterial blood flow; H_{TBF} = total hepatic blood flow; H_{TBV} = total hepatic blood volume; PS = permeability surface area product; α = Hepatic arterial factor.

* indicates significantly different from both normo- and hyper-capnia, $P < 0.05$.

Φ indicates significantly different from hyper-capnia only, $P < 0.05$.

† indicates significantly different from normo-capnia only, $P < 0.05$.

δ indicates significantly different from other tissues at all capnic levels, $P < 0.05$.

ξ indicates significantly different from tumor core at all capnic levels, $P < 0.05$.

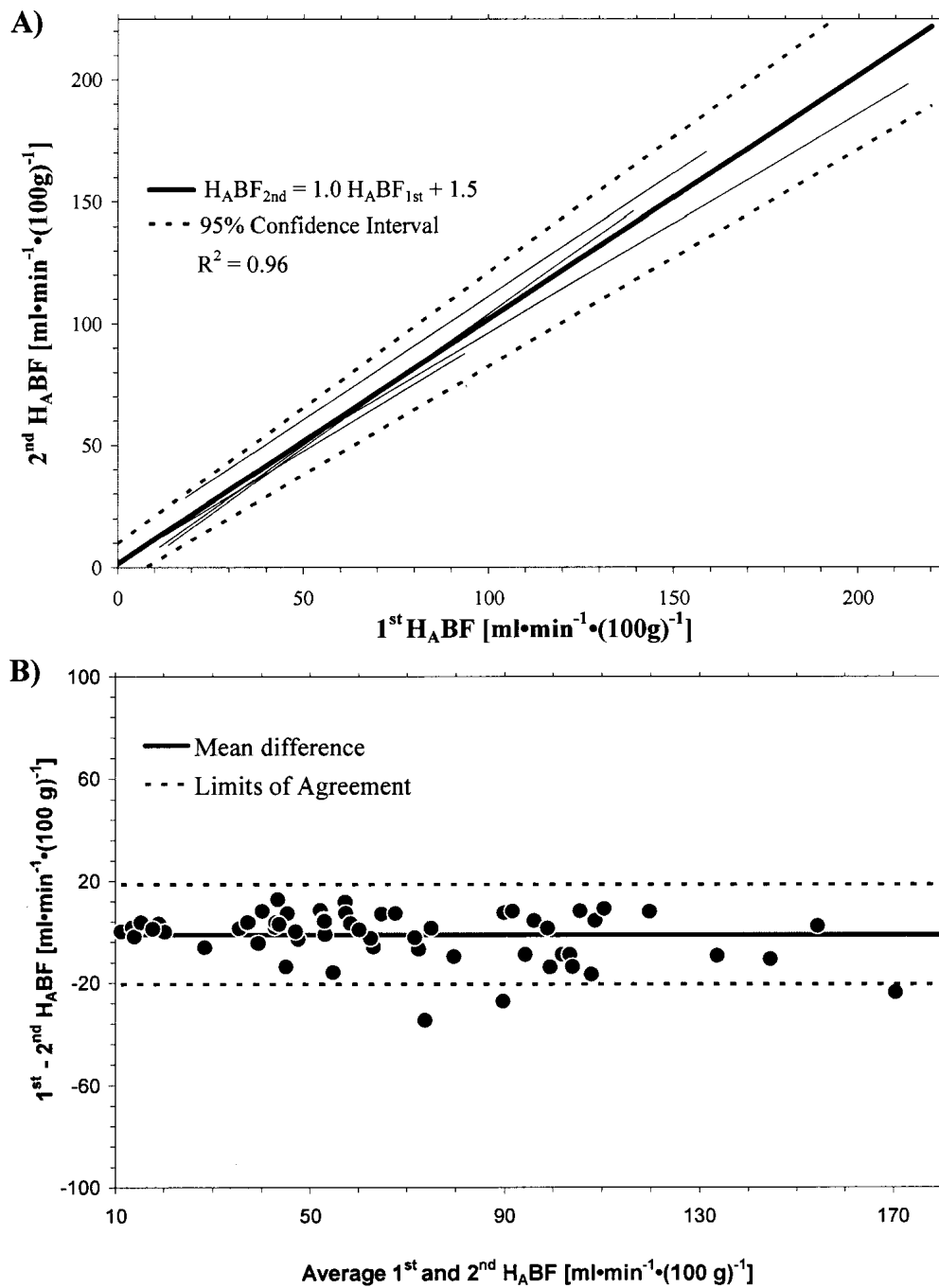
An ANOVA showed that repeated measurements of $H_{A}BF$ with DCE-CT on either the same day or different days are not different from each other. Furthermore, the CVs of DCE-CT $H_{A}BF$ in normal liver, tumor core and rim are 5.7, 24.9 and 1.4% respectively. Parameters other than $H_{A}BF$ also showed similar results with better precision in the tumor rim and normal tissue than in the tumor core, Table 2.3. The GEE and Bland-Altman plot for $H_{A}BF$ determined from the precision studies are shown in Figure 2.4. The average linear regression line has a slope of 1.0 ± 0.09 and an intercept of $1.5 \pm 6.7 \text{ ml}\cdot\text{min}^{-1}\cdot(100 \text{ g})^{-1}$, both of which were not significantly different from those of the line of identity ($P > 0.05$). This suggests that the repeated measurements of $H_{A}BF$ were identical on the average. The Bland-Altman plot comparing the first and second $H_{A}BF$ measurements gives a mean difference of $-1.0 \text{ mL}\cdot\text{min}^{-1}\cdot(100 \text{ g})^{-1}$ and the 95 % limits of agreement was -20.7 to $18.6 \text{ ml}\cdot\text{min}^{-1}\cdot(100 \text{ g})^{-1}$, Figure 2.4(B). Results from the GEE and Bland-Altman plot for the other parametric maps are given in Table 2.4. The CV derived from the Monte Carlo simulation for $H_{T}BF$ and PS was plotted as a function of noise in the normal tissue, tumor core and rim, Figure 2.5. The simulation showed that $H_{T}BF$ in the normal tissue and tumor rim were equivalent in reproducibility (CV), while the tumor core was the most sensitive to noise. It also showed that the corresponding PS in the tumor rim was comparatively more reproducible than those in the tumor core and normal tissue. Similar results were seen in the other perfusion parameters, but were not shown in the interest of space. In general, the CVs derived from the Monte Carlo simulation at a noise level of $SD = 4$ were comparable to those in the precision study, Table 2.3. Both studies showed that noise had a greater effect in the tumor core than in the tumor rim or normal tissue.

Table 2.3: The coefficient of variation for all the functional parameters

	<i>ROI Area</i> (cm^2)	<i>Coefficient of Variation (%)</i>				
		H_{ABF}	α	H_TBF	H_TBV	PS
<i>Tumor Rim</i>	3.15 ± 0.22	1.4	3.5	0.5	0.5	6.7
<i>Tumor Core</i>	0.97 ± 0.17	24.9	14.9	41.6	16.9	42.2
<i>Normal Tissue</i>	1.65 ± 0.05	5.7	14.0	7.4	6.3	18.6

Note that values are the coefficients of variation determined using an ANOVA.

Figure 2.4: Precision of DCE-CT perfusion measurement



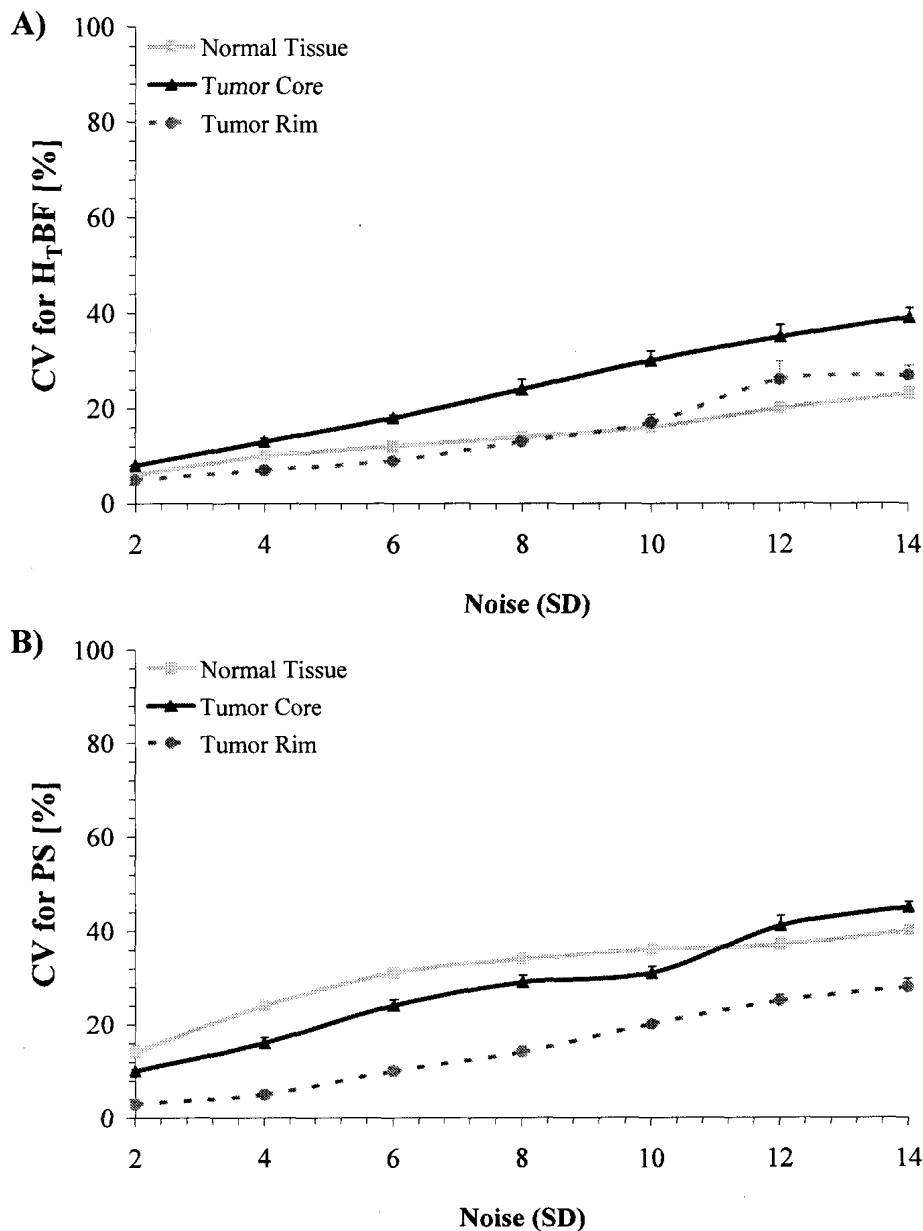
A) Plot of the first vs. the second H_ABF measured in all rabbits under normal condition in the precision study. The thin solid lines are the individual linear regression lines for each rabbit and the thick solid line is the average of all the individual rabbit regression lines (slope = 1.0 ± 0.09 , intercept = $1.5 \pm 6.7 \text{ ml}\cdot\text{min}^{-1}\cdot(100 \text{ g})^{-1}$). The dotted lines represent

the 95% CI for the average slope and intercept. **B)** Bland–Altman plot comparing first and second H_{ABF} measurement. The mean difference (solid line) between the two methods is $-1.0 \text{ ml}\cdot\text{min}^{-1}\cdot(100 \text{ g})^{-1}$. The limits of agreement (dotted lines), that is, the boundaries of the region in which 95% of the differences lie, are -20.68 and $18.58 \text{ ml}\cdot\text{min}^{-1}\cdot(100 \text{ g})^{-1}$.

Table 2.4: GEE and Bland-Altman analysis between the first and second measurement for each functional parameter.

	Generalized Estimating Equation			<i>Bland-Altman</i> Mean difference (limits of agreement)
	<i>Slope</i> mean (95% CI)	<i>Intercept</i> mean (95% CI)	R^2 mean (SD)	
H_{ABF} ($\text{ml}\cdot\text{min}^{-1}\cdot(100\text{g})^{-1}$)	1.0(1.11, 0.89)	1.5(9.7, -6.8)	0.96 (0.02)	-1.0 (18.6, -20.7)
H_{7BF} ($\text{ml}\cdot\text{min}^{-1}\cdot(100\text{g})^{-1}$)	0.96(1.11, 0.81)	17.5(78, -43)	0.90 (0.10)	-7.3 (70.1, -84.7)
H_{7BV} ($\text{ml}\cdot(100\text{g})^{-1}$)	0.92(1.01, 0.84)	1.9(6.8, -2.9)	0.92 (0.12)	0.11 (8.6, -8.4)
H_{AF} (%)	0.94(1.17, 0.72)	0.6(7.6, -6.3)	0.91 (0.05)	1.3 (11.5, -8.9)
PS ($\text{ml}\cdot\text{min}^{-1}\cdot(100\text{g})^{-1}$)	0.92(1.17, 0.68)	5.1(12.9, -2.7)	0.81 (0.16)	-2.1 (16.3, -20.5)

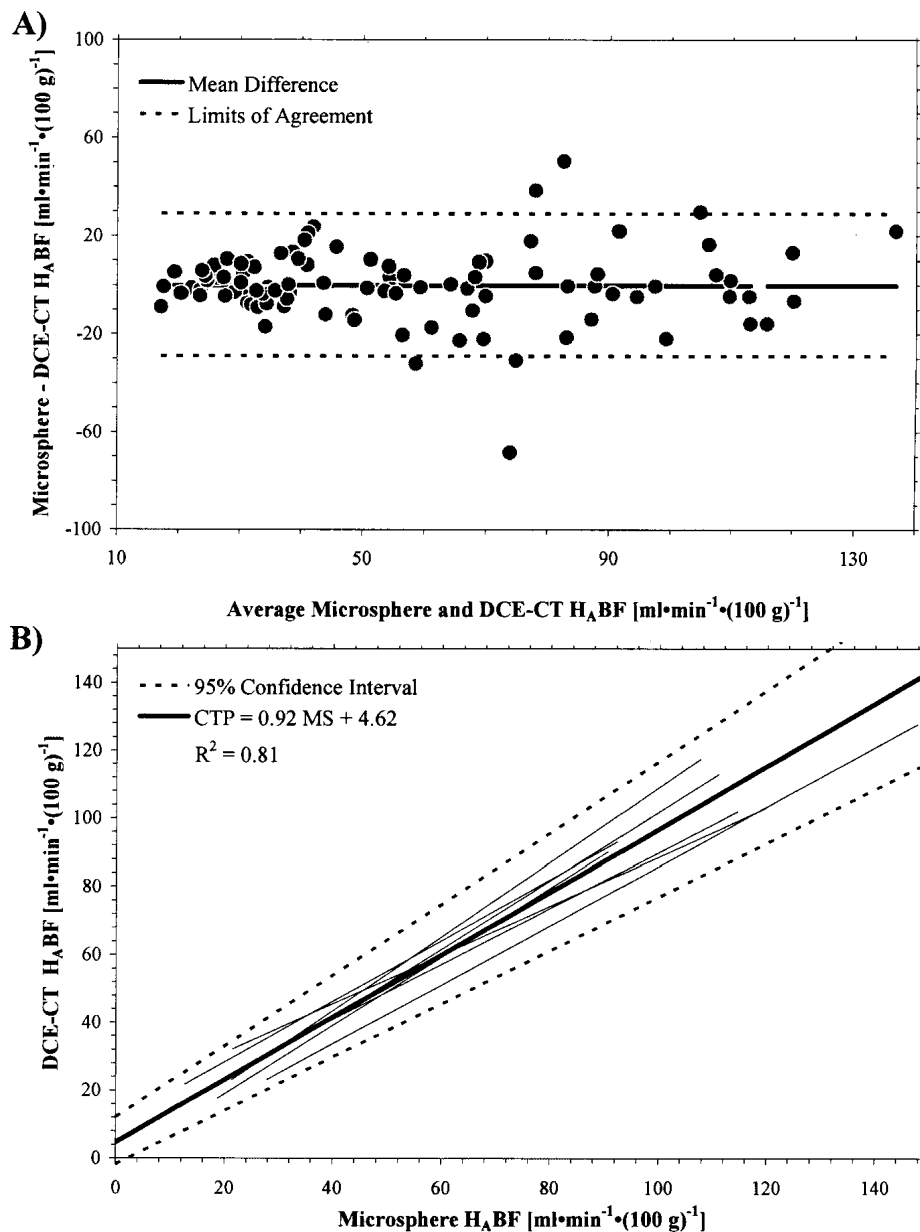
Figure 2.5: Monte Carlo Simulation



Monte Carlo simulation results on the precision of model parameter estimates at different noise conditions created by adding Gaussian noise with different standard deviation (SD) to the simulated tissue curve using the Monte Carlo method. The incremental noise resulted in SNR ranging from 2.4 to 17.2 in the normal tissue, 1.1 to 7.7 in the tumor core and 2.9 to 20.4 in the tumor rim. Coefficient of variation (CV) was used to express the precision of each parameter estimate. **A)** CV of H_TBF and **B)** CV of PS in normal tissue, tumor core and rim.

An ANOVA showed no significant differences between DCE-CT and microsphere $H_{A}BF$ measurements, $P > 0.05$. The Bland-Altman plot comparing DCE-CT and microsphere $H_{A}BF$ measurements gives a mean difference of $-0.13 \text{ ml}\cdot\text{min}^{-1}\cdot(100 \text{ g})^{-1}$, which is not significantly different from zero Figure 2.6(A). The limits of agreement, the region in which 95 % of the differences lie are from -29.21 to $28.95 \text{ ml}\cdot\text{min}^{-1}\cdot(100 \text{ g})^{-1}$. A plot of DCE-CT vs. microsphere $H_{A}BF$ measurements in all rabbits and under all capnic conditions is shown in Figure 2.6(B). The average slope of the individual linear regression of $H_{A}BF$ measurements from a single rabbit was 0.92 ± 0.05 , which was significantly different from a value of zero ($P < 0.05$), but not significantly different from the line of identity ($P > 0.05$). This indicates that there was a significant correlation between the DCE-CT and microsphere $H_{A}BF$ measurements. The average intercept, $4.62 \pm 2.69 \text{ ml}\cdot\text{min}^{-1}\cdot(100 \text{ g})^{-1}$, was not significantly different from zero, $P > 0.05$. The average R^2 was 0.81 ± 0.05 (range 0.64 – 0.96).

Figure 2.6: Validation of DCE-CT perfusion against radioactive microsphere



A) Bland–Altman plot comparing DCE-CT and microsphere $H_A BF$ measurements. The mean difference (solid line) between the two methods is $-0.13 \text{ ml}\cdot\text{min}^{-1}\cdot(100 \text{ g})^{-1}$. The limits of agreement (dotted lines), that is, the boundaries of the region in which 95% of the differences lie, are -29.21 and $28.95 \text{ ml}\cdot\text{min}^{-1}\cdot(100 \text{ g})^{-1}$. **B)** Plot of DCE-CT vs. microsphere $H_A BF$ measurements in all rabbits under all capnic conditions. The thin solid lines are the individual linear regression lines for each rabbit and the thick solid line is the average of all the individual rabbit regression lines (slope = 0.92 ± 0.05 , intercept = 4.62

$\pm 2.69 \text{ ml}\cdot\text{min}^{-1}\cdot(100 \text{ g})^{-1}$). The dotted lines represent the 95% confidence interval (CI) for the average slope and intercept.

2.4 DISCUSSION

We have developed and validated a new non-invasive DCE-CT method for measuring $H_A\text{BF}$ with the Johnson and Wilson (16) model under the adiabatic approximation (21). The DCE-CT $H_A\text{BF}$ was validated directly against radiolabelled microsphere, Figure 2.6; while α and $H_T\text{BF}$ were validated indirectly, since $H_A\text{BF}$ is the product of α and $H_T\text{BF}$. Microsphere $H_A\text{BF}$ measured in the tumor rim under hypoxia were slightly lower than that measured with DCE-CT, Table 2.2 (C). The presence of arteriovenous shunting in tumors may have cause an underestimation of the microsphere $H_A\text{BF}$ (25). The Monte Carlo simulations, accuracy and precision study showed that our perfusion model is well suited for the separation of each perfusion parameters. Moreover, the simulations showed that the higher CV of tumor core parameter estimates was due to lower $H_T\text{BF}$ and corresponding low SNR. Both simulation and precision study showed that PS had the poorest CV among all the parameters for each tissue type. For both tumor rim and normal tissue, the CV of PS, being less than 20%, was within acceptable range, Table 2.3.

Our study demonstrates that DCE-CT measurement of liver functional parameters is accurate and precise, thus well suited for the non-invasive investigation of liver diseases. Our scanning protocol developed in an animal model (12) was modified by Sahani *et al.* and used in patient studies (26). VX2 carcinoma is a rabbit tumor derived from a virus-induced papilloma, hence it is different in origin and pathology from most

human tumors. However, the underlying physiology of hemodynamics should remain the same in both human and rabbit VX2 liver tumor, hemodynamic functional parameters derived in human studies will remain accurate as we have demonstrated in the rabbit studies. Precision in patient studies will be more affected by movement and respiratory artifacts because patients are awake while the rabbits are anesthetized in this study (26). The SNR of the dynamic CT images will be poorer in patient studies because of increased attenuation relative to animal studies. The extent of the decrease in precision of liver functional parameters in patients studies require further additional studies that are outside the scope of the present study. Our designation of tumor core and rim was for the purpose of identifying abnormal liver tissue with lower and higher perfusion than normal tissue. Without histopathological correlative data, we cannot be sure that the so-named regions exactly corresponded to the 'real' tumor core and rim. However, they should be in the close neighborhood because a variety of neoplastic tumors have cores that are known to be hypovascular, while the tumor rim is hypervascular from upregulated angiogenic activities (27, 28).

In our study, we used isoflurane for anesthesia and pancuronium for muscle relaxation. By adding pancuronium we were able to limit the level of isoflurane required to maintain adequate anesthesia to 1.5 MAC. The effects of these drugs should be considered when interpreting our results. Pancuronium does not seem to significantly affect splanchnic circulation (29). Isoflurane, on the other hand, is known to severely affect splanchnic circulation (30). We cannot exclude the possibility that the level of isoflurane used may have modified the response of splanchnic circulation to hyper- and hypo-capnia. However, these anesthetic effects should not affect the results of the

accuracy study, since both microsphere and DCE-CT data were collected simultaneously under the same conditions.

Our data show that hyper-capnia did not have a significant effect on perfusion related parameters, Table 2.2. This finding could be due to the influence of isoflurane. Gelman *et al.* showed that the induction of 1 MAC isoflurane in dogs leads to a twofold increase in H_ABF over the awake state (30). Isoflurane may have caused the hepatic artery to be maximally dilated and unable to respond to increase in $PaCO_2$. Our hyper-capnia results were similar to those performed under pentobarbital anesthesia by Hughes *et al.* that showed H_TBF and H_ABF remained constant at steady state $PaCO_2$ concentration up to 70 mmHg (31). Pentobarbital is believed to have no significant effect on liver blood flow (32). Conversely, Fujita *et al.* showed an increase in H_TBF and P_VBF with a corresponding reduction in H_ABF during hyper-capnia under pentobarbital anesthesia (33). However, Fujita *et al.* acknowledged that surgical interventions during the electromagnetic flow technique and the difference between nutritive flow (DCE-CT and microsphere technique) and total flow (electromagnetic flow meter) may lead to discrepancies between the two techniques (33). Hypo-capnia did not induce a buffer response, which is consistent with other published results showing a reduction in H_ABF without a matched increase in P_VBF measured under hypo-capnia compared to normo-capnia (33-35).

Fujita *et al.* (33) demonstrated that a decrease in the rate of oxygen delivery to the liver correlates to a reduction in H_ABF but not H_TBF , which remained unchanged. This suggests that the measurement of H_ABF is a more reliable predictor of hepatic oxygenation than H_TBF . During P_VBF disruption the hepatic arterial buffer response, by

inference H_{ABF} , plays an important role in maintaining hepatic tissue oxygenation through microvascular remodeling (36). The increase in H_{ABF} seen in the tumor possibly reflects microvascular remodeling from the hepatic artery to meet the increased oxygen and metabolic demand during angiogenesis, Figure 2.3 (A) and Table 2.2. This suggests that the implanted VX2 carcinoma derived a higher portion of its blood supply from the arterial rather than the portal circulation, in agreement with observations made by Miles *et al.* (11). This is similar to the hepatic arterial shift demonstrated in cirrhotic liver by Richter *et al.* (37) and in liver transplant recipient by Marcos *et al.* (38). Hence, the ability to non-invasively measure H_{ABF} may allow for the assessment of liver function after liver transplant and for monitoring the progression of cirrhosis to hepatocellular carcinoma (3, 7, 37, 38).

H_TBV is a combined measure of functional micro-vascular density and diameter (perfused cross-sectional area) because it reflects the pooling of blood in functioning blood vessels in a mass of tissue. There was a significant difference between H_TBV in the tumor core compared to the tumor rim and normal tissue, Table 2.2. This finding is similar to those reported by Fukumura *et al.* who demonstrated that vessel density in the center of the tumor was significantly lower than that in the periphery (39). However, Fukumura *et al.* also showed that while vessel density in liver tumors was sevenfold lower than that in the normal liver, the tumor vessel diameter was much larger than that in the normal liver (39). This effect may explain why there was no significant difference between H_TBV measured in the tumor rim compared to the normal tissue, Table 2.2.

PS is the product of permeability and total surface area of perfused capillary endothelium (sinusoid in this study) in a mass of tissue. Knowledge of PS can be used to

optimize the delivery of drugs to solid tumors (40). In our study, PS in the tumor rim was found to be significantly higher than that in the tumor core, Table 2.2. The high PS in the tumor rim may arise from increased blood flow (hence, surface area of perfused capillaries, S) or/and permeability (P) of capillaries, both of which is an indicator of increased angiogenic activity resulting from upregulated VPF/VEGF expression in tumor (27). This is consistent with previously published data on the microvascular permeability of dextran in VX2 carcinoma grown in the rabbit ear chamber (41).

There are several limitations for the non-invasive measurement of H_A BF and related parameters using DCE-CT. One limitation is the effect of partial volume averaging (PVA). Cenic *et al.* demonstrated that when arterial concentration is underestimated from PVA, blood flow is overestimated (42). Moreover, PVA correction can only be performed effectively on vessels at right angle to the imaging plane. In our study, we eliminated the effect of PVA on the arterial input by approximating the hepatic artery input with the time-enhancement curve from the aorta which is > 0.5 cm in diameter (data not shown), much larger than the ~ 0.7 mm spatial resolution of CT images and was invariably scanned in cross-section. PVA in the portal vein was reduced by using time-enhancement curves from the portal vein trunk which was also scanned in cross-section and whose mean radial diameter is approximately 0.53 cm (data not shown).

Another limitation is that only measurement of H_A BF was validated, but not H_T BF due to other challenges in the latter case. The main ones being the dual blood supply of the liver and the inaccessibility of the portal system to some tracers (43). Proposed methods to solve these problems such as radiolabelled microsphere and [^{15}O] water

Positron Emission Tomography (PET) have their own sets of challenges. [^{15}O] water PET is limited by availability, cost, and limited spatial resolution to accurately resolve the portal vein (44). Radiolabelled microsphere cannot measure $P_V\text{BF}$ directly. Microspheres injected into the arterial blood stream are lodged in capillary beds; hence the technique can only measure regional and total $H_A\text{BF}$. The total $P_V\text{BF}$ can be indirectly estimated by summing all the flow in splanchnic organs that drain into the portal vein, but not regional $P_V\text{BF}$ (10). Hence, a suitable method to validate regional measurement of $H_T\text{BF}$ is yet to be determined. However, the normal tissue regional $H_T\text{BF}$ value of $224 \pm 16 \text{ ml}\cdot\text{min}^{-1}\cdot(100 \text{ g})^{-1}$ reported in our study, Table 2.2, is consistent with the indirect microsphere $H_T\text{BF}$ measurement of $178 \pm 56 \text{ ml}\cdot\text{min}^{-1}\cdot(100 \text{ g})^{-1}$ reported by Materne *et al.* (10).

Radiation dose associated with our DCE-CT protocol is also a limiting factor and it has to be optimized before clinical applications can be contemplated. High kVp and mA increase dose to the patient but generate high image quality with low CT noise; whereas low kVp and mA reduce dose to the patient but increase CT noise (45). A typical adult abdominal CT scan using 120 kVp and 340 mA produces an effective dose of 14 mSv (46). For our DCE-CT liver study, the X-ray tube parameters were lowered to 120 kVp and 60 mA and would have produced an effective dose of 11.9 mSv in human. The lowered X-ray tube parameters allowed us to reduce the effective dose and acquire reasonably good quality images. A more detailed analysis is needed prior to clinical application to determine the correct balance among image quality, dose, and precision.

Our findings demonstrate feasibility for making precise, non-invasive regional perfusion measurements in the liver using DCE-CT. Both $H_A\text{BF}$ and $H_T\text{BF}$ are important physiological parameters of liver function and reflect adaptive response to injury,

regeneration, and the development of malignancy (4-6). DCE-CT imaging has the potential to enhance the diagnosis of liver disease with CT scanners by adding physiological information to the already detailed anatomical images.

2.5 REFERENCES

1. Pandharipande PV, Krinsky GA, Rusinek H, Lee VS. Perfusion imaging of the liver: current challenges and future goals. *Radiology* 2005; 234:661-673.
2. Lauth WW. Mechanism and role of intrinsic regulation of hepatic arterial blood flow: hepatic arterial buffer response. *Am J Physiol* 1985; 249:G549-G556.
3. Park YN, Yang CP, Fernandez GJ, Cubukcu O, Thung SN, Theise ND. Neoangiogenesis and sinusoidal "capillarization" in dysplastic nodules of the liver. *Am J Surg Pathol* 1998; 22:656-662.
4. Kin Y, Nimura Y, Hayakawa N, et al. Doppler analysis of hepatic blood flow predicts liver dysfunction after major hepatectomy. *World J Surg* 1994; 18:143-149.
5. Miles KA, Leggett DA, Kelley BB, Hayball MP, Sinnatamby R, Bunce I. In vivo assessment of neovascularization of liver metastases using perfusion CT. *Br J Radiol* 1998; 71:276-281.
6. Wu Y, Campbell KA, Sitzmann JV. Hormonal and splanchnic hemodynamic alterations following hepatic resection. *J Surg Res* 1993; 55:44-48.
7. Kobayashi M, Ikeda K, Hosaka T, et al. Dysplastic nodules frequently develop into hepatocellular carcinoma in patients with chronic viral hepatitis and cirrhosis. *Cancer* 2006; 106:636-647.
8. Cao Y, Platt JF, Francis IR, et al. The prediction of radiation-induced liver dysfunction using a local dose and regional venous perfusion model. *Med Phys* 2007; 34:604-612.
9. Cuenod C, Leconte I, Siauve N, et al. Early changes in liver perfusion caused by occult metastases in rats: detection with quantitative CT. *Radiology* 2001; 218:556-561.
10. Materne R, Van Beers BE, Smith AM, et al. Non-invasive quantification of liver perfusion with dynamic computed tomography and a dual-input one-compartmental model. *Clin Sci (Lond)* 2000; 99:517-525.
11. Miles KA, Hayball MP, Dixon AK. Functional images of hepatic perfusion obtained with dynamic CT. *Radiology* 1993; 188:405-411.
12. Stewart EE, Chen X, Hadway J, Lee TY. Correlation between hepatic tumor blood flow and glucose utilization in a rabbit liver tumor model. *Radiology* 2006; 239:740-750.
13. Lee TY, Purdie TG, Stewart E. CT imaging of angiogenesis. *Q J Nucl Med* 2003; 47:171-187.

14. Goresky CA. A linear method for determining liver sinusoidal and extravascular volumes. *Am J Physiol* 1963; 204:626-640.
15. Martinez-Hernandez A, Martinez J. The role of capillarization in hepatic failure: studies in carbon tetrachloride-induced cirrhosis. *Hepatology* 1991; 14:864-874.
16. Johnson JA, Wilson TA. A model for capillary exchange. *Am J Physiol* 1966; 210:1299-1303.
17. van den Hoff J. Blood flow quantification with permeable contrast agents: a valid technique? *Radiology* 2007; 243:909-910.
18. Ramani R, Todd MM, Warner DS. The influence of a cryogenic brain injury on the cerebrovascular response to isoflurane in the rabbit. *J Cereb Blood Flow Metab* 1991; 11:388-397.
19. Meier P, Zierler KL. On the theory of the indicator-dilution method for measurement of blood flow and volume. *J Appl Physiol* 1954; 6:731-744.
20. Heymann MA, Payne BD, Hoffman JI, Rudolph AM. Blood flow measurements with radionuclide-labeled particles. *Prog Cardiovasc Dis* 1977; 20:55-79.
21. St Lawrence KS, Lee TY. An adiabatic approximation to the tissue homogeneity model for water exchange in the brain: I. Theoretical derivation. *J Cereb Blood Flow Metab* 1998; 18:1365-1377.
22. Eliasziw M, Young SL, Woodbury MG, Fryday-Field K. Statistical methodology for the concurrent assessment of interrater and intrarater reliability: using goniometric measurements as an example. *Phys Ther* 1994; 74:777-788.
23. Bland JM, Altman DG. Statistical methods for assessing agreement between two methods of clinical measurement. *Lancet* 1986; 1:307-310.
24. Zeger SL, Liang KY, Albert PS. Models for longitudinal data: a generalized estimating equation approach. *Biometrics* 1988; 44:1049-1060.
25. Fan FC, Schuessler GB, Chen RY, Chien S. Determinations of blood flow and shunting of 9- and 15-micrometer spheres in regional beds. *Am J Physiol* 1979; 237:H25-H33.
26. Sahani DV, Holalkere NS, Mueller PR, Zhu AX. Advanced hepatocellular carcinoma: CT perfusion of liver and tumor tissue--initial experience. *Radiology* 2007; 243:736-743.
27. Claffey KP, Brown LF, del Aguila LF, et al. Expression of vascular permeability factor/vascular endothelial growth factor by melanoma cells increases tumor

- growth, angiogenesis, and experimental metastasis. *Cancer Res* 1996; 56:172-181.
28. Tozer GM, Lewis S, Michalowski A, Aber V. The relationship between regional variations in blood flow and histology in a transplanted rat fibrosarcoma. *Br J Cancer* 1990; 61:250-257.
 29. Saxena PR, Dhasmana KM, Prakash O. A comparison of systemic and regional hemodynamic effects of d-tubocurarine, pancuronium, and vecuronium. *Anesthesiology* 1983; 59:102-108.
 30. Gelman S, Fowler KC, Smith LR. Liver circulation and function during isoflurane and halothane anesthesia. *Anesthesiology* 1984; 61:726-730.
 31. Hughes RL, Mathie RT, Campbell D, Fitch W. Effect of hypercarbia on hepatic blood flow and oxygen consumption in the greyhound. *Br J Anaesth* 1979; 51:289-296.
 32. Gilmore JP. Effect of anesthesia and hepatic sampling site upon hepatic blood flow. *Am J Physiol* 1958; 195:465-468.
 33. Fujita Y, Sakai T, Ohsumi A, Takaori M. Effects of hypocapnia and hypercapnia on splanchnic circulation and hepatic function in the beagle. *Anesth Analg* 1989; 69:152-157.
 34. Hughes RL, Mathie RT, Fitch W, Campbell D. Liver blood flow and oxygen consumption during hypocapnia and IPPV in the greyhound. *J Appl Physiol* 1979; 47:290-295.
 35. Johnson EE. Splanchnic hemodynamic response to passive hyperventilation. *J Appl Physiol* 1975; 38:156-162.
 36. Kollmar O, Corsten M, Scheuer C, Vollmar B, Schilling MK, Menger MD. Portal branch ligation induces a hepatic arterial buffer response, microvascular remodeling, normoxygenation, and cell proliferation in portal blood-deprived liver tissue. *Am J Physiol Gastrointest Liver Physiol* 2007; 292:G1534-G1542.
 37. Richter S, Mucke I, Menger MD, Vollmar B. Impact of intrinsic blood flow regulation in cirrhosis: maintenance of hepatic arterial buffer response. *Am J Physiol Gastrointest Liver Physiol* 2000; 279:G454-G462.
 38. Marcos A, Olzinski AT, Ham JM, Fisher RA, Posner MP. The interrelationship between portal and arterial blood flow after adult to adult living donor liver transplantation. *Transplantation* 2000; 70:1697-1703.

39. Fukumura D, Yuan F, Monsky WL, Chen Y, Jain RK. Effect of host microenvironment on the microcirculation of human colon adenocarcinoma. *Am J Pathol* 1997; 151:679-688.
40. Jain RK, Gerlowski LE. Extravascular transport in normal and tumor tissues. *Crit Rev Oncol Hematol* 1986; 5:115-170.
41. Gerlowski LE, Jain RK. Microvascular permeability of normal and neoplastic tissues. *Microvasc Res* 1986; 31:288-305.
42. Cenic A, Nabavi DG, Craen RA, Gelb AW, Lee TY. Dynamic CT measurement of cerebral blood flow: a validation study. *AJNR Am J Neuroradiol* 1999; 20:63-73.
43. Johnson DJ, Muhlbacher F, Wilmore DW. Measurement of hepatic blood flow. *J Surg Res* 1985; 39:470-481.
44. Ziegler SI, Haberkorn U, Byrne H, et al. Measurement of liver blood flow using oxygen-15 labelled water and dynamic positron emission tomography: limitations of model description. *Eur J Nucl Med* 1996; 23:169-177.
45. McNitt-Gray MF. AAPM/RSNA Physics Tutorial for Residents: Topics in CT. Radiation dose in CT. *Radiographics* 2002; 22:1541-1553.
46. Shrimpton PC, Hillier MC, Lewis MA, Dunn M. National survey of doses from CT in the UK: 2003. *Br J Radiol* 2006; 79:968-980.

CHAPTER 3: CORRELATION BETWEEN HEPATIC TUMOR BLOOD FLOW AND GLUCOSE UTILIZATION IN A RABBIT LIVER TUMOR MODEL

The content of this chapter have been adapted from the paper entitled “Correlation between hepatic tumor blood flow and glucose utilization in a rabbit liver tumor model”, published in the journal *Radiology* vol. 239 (3): pp. 740 – 750 (2006) by Errol E. Stewart, Xiaogang Chen, Jennifer A. Hadway, Ting-Yim Lee.

3.1 INTRODUCTION

As the metabolic demand of a tissue increases, an equivalent increase in oxygen supply via increased blood flow (perfusion) is necessary to maintain aerobic respiration (1, 2). The coupling of blood flow to metabolic rate under physiological and pathophysiological conditions has been demonstrated in a variety of organs and tissues, such as in the brain, muscle, heart, and various cancers (2-6). Malignant neoplasm usually exhibits regions of low oxygenation due to poor perfusion (7). The limited availability of oxygen in these hypoxic regions results in increased anaerobic glycolysis and hence less efficient use of glucose, which in turn will necessitate a high extraction and uptake of glucose and its radioactive analogue, fluorine-18 fluoro-2-deoxy-D-glucose ($[^{18}\text{F}]$ FDG). Thus, autoradiographic studies in animal models have demonstrated that adjacent to the necrotic area of a tumor there is always increased glucose ($[^{18}\text{F}]$ FDG) uptake (8, 9). More specifically, Mankoff *et al.* suggested that an elevated ratio of $[^{18}\text{F}]$ FDG metabolic rate to blood flow is an indicator of glucose use relative to delivery, and

an elevated ratio, or uncoupling of blood flow and glucose utilization, indicates high glucose extraction by the tumor (4). Besides indicating a higher glucose extraction by the tumor, the uncoupling of blood flow and glucose utilization may also reflect tissue hypoxia. Clinical data have shown that hypoxia negatively affects the treatment outcome of both radiotherapy and anti-cancer drug treatment (10). There is significant potential for therapeutic benefit if tumor hypoxia can be diagnosed non-invasively and the information used to define high-risk populations, and modify therapy accordingly.

Dynamic contrast enhanced computed tomography (DCE-CT) perfusion (11) and [^{18}F] FDG positron emission tomography (PET) are two functional imaging methods that can non-invasively measure physiological changes, specifically blood flow and glucose utilization in the liver. However, the measurement of liver [^{18}F] FDG metabolic rate is relatively invasive (12). Hence, the accumulation of [^{18}F] FDG, which can be measured with the standardized uptake value (SUV), is taken to reflect the rate of tumor glycolytic metabolism (13). Changes in liver perfusion correlate with the growth of new tumor blood vessels (angiogenesis) (14). Recent studies using dynamic contrast-enhanced CT have demonstrated its ability to non-invasively measure liver perfusion (15, 16).

In contrast to other organs or tissues, which are supplied only by arteries, the liver has a dual blood supply. The liver receives its blood both from the hepatic artery delivering oxygenated blood from the heart and the portal vein draining venous blood from the gastrointestinal tract (17). Approximately two-thirds of the blood flow to the liver is supplied by the portal vein, the remaining one-third is supplied by the common and proper hepatic arteries (18). The purpose of our study was to determine the

relationship between hepatic tumor blood flow and glucose utilization *in vivo* using a hybrid PET/CT scanner.

3.2 MATERIALS AND METHODS

3.2.1 Study Protocol

Eight healthy male New Zealand White rabbits (2.9 – 3.5 kg) were used in these experiments. The experimental procedures were approved by the Council on Animal Care and Use Sub-Committee at the University of Western Ontario, Canada. Partial financial support for this work was provided by the General Electric Healthcare (in the form of salary support for E.E.S). The authors had control of the data and the information submitted for publication. For each animal anesthesia was induced with isoflurane via a mask, an endotracheal tube was inserted and anesthesia was maintained by mechanical ventilation at a rate of 20 breathes per min with a mixture of oxygen and isoflurane (1.5 – 2.5%). Respiratory reflex was suppressed with vecuronium bromide if required. The animal's body temperature was maintained between 38.5 and 39.5 °C with a heated recirculating water blanket.

Tumor cells were harvested from a VX2 carcinoma grown in a leg of a donor rabbit. Subsequently, 0.25 mL of these harvested cells suspended in Hanks balanced salt solution was injected directly into the liver of the rabbit. Functional CT studies were performed prior to and every 4 days until metastatic nodules were observed in the lung (on average 24 days post). At that time the animals were sacrificed by an overdose of sodium pentobarbital. Five out of eight animals had [¹⁸F] FDG-PET scans performed prior to and every 8 days after tumor implantation.

3.2.2 DCE-CT Scanning Protocol

One ear vein was cannulated for administration of the muscle relaxant vecuronium bromide during the experiment, and for the injection of contrast (Omnipaque 300, Berlex Canada), and [^{18}F] FDG (Hamilton Health Science Center, Canada, synthesis technique as described by Hamacher *et al.* (19)). The abdomen of the rabbit was imaged by the CT component of a hybrid PET/CT scanner (Discovery LS, General Electric Medical Systems, Waukesha, Wisconsin) using the following technique. A localization axial CT scan was performed to position four 5 mm slices. The first slice was at the dome of the liver, just below the diaphragm, while the 4th slice was at the level of the upper pole of either kidney.

In order to determine liver perfusion, CT images of the four chosen slices were acquired with a two-phase scan protocol. The scan parameters for the first phase of the scan protocol were 80 kVp, 60 mA, 1 s with four slices per rotation. During this phase, the liver was continuously (cine) scanned for 30 s simultaneously with the injection of a bolus of non-ionic contrast agent (Omnipaque 300 diluted to 200 mg iodine mL⁻¹ and a dose of 1.5 mL kg⁻¹) at a rate of 1 mL s⁻¹. Prior to the injection of contrast, the ventilator was turned-off to eliminate motion from breathing. The images were reconstructed at 0.5 s intervals to give time-density curves of the same time interval. The second phase of the scan protocol followed 10 s after the first phase. During the second phase the ventilator was turned-on with a breathing cycle of 20 breathes per min, and a 4.0 s burst of cine scan was performed every 10 s for a period of 2 min. The scan parameters were 80 kVp, 60 mA, 1 s per rotation with four 5 mm thick slices. However, the images were

reconstructed at 0.2 s intervals instead of 0.5 s intervals, resulting in 19 images per slice location for each cine scan.

3.2.3 [^{18}F] FDG-PET Acquisition and Image Reconstruction

The [^{18}F] FDG-PET scans were acquired after the DCE-CT imaging. Prior to the DCE-CT scans, 50 ± 15 MBq of [^{18}F] FDG were injected via an ear vein catheter. Approximately, 40 min later, a four-slice helical CT scan covering the thorax and abdomen was acquired at 1 s rotational speed and 1.5:1 pitch and with a transaxial field of view (FOV) of 50 cm. The x-ray tube was operated at a voltage of 140 kVp and a current of 80 mA. CT images were reconstructed into 5 mm thick slices at 4.25 mm interval and were subsequently used to correct the PET emission images for attenuation. At least three of the CT images in this acquisition matched three of the 5 mm x 5 mm slices from the DCE-CT study. The PET scanner has a transaxial FOV of 55 cm and an axial FOV of 15.2 cm divided into 35 4.25 mm thick slices which coincided with the helical CT scan images. PET images were acquired in 2-dimensional mode (septa between detector rings of the scanner were fully extended to reduce cross-plane scatter) for 5 min per axial FOV for a total of 10 min (i.e. 2 bed positions to cover the entire thorax and abdomen of a rabbit). Software provided with the Discovery LS PET/CT scanner was used to initially correct the emission data for random coincidences, dead time, scatter coincidences and attenuation using CT attenuation correction maps from the helical CT scan. The corrected data was reconstructed into transaxial images using ordered-subset expectation maximization software. The resulting in-plane image

resolution of the transaxial images was approximately ~ 4.5 mm full-width at half-maximum (FWHM), with an axial resolution of approximately ~ 4.5 mm FWHM.

3.2.4 Functional Parameters Calculation

Images from the first and second phase scans of the DCE-CT study were co-registered to remove motion caused by breathing. From each 4.0 s burst of cine scan during the second phase, the image that best matched the images at the same slice location from the first phase (with breath hold) was selected. These selected second phase images were used together with the first phase breath hold images for calculation of functional parameters (see Appendix B).

Contrast enhancement or time density curves from the aorta (to approximate the hepatic artery), portal vein and liver parenchyma were obtained from the co-registered first and second phase images. A weighted summation of the aortic and portal venous curves was deconvolved against the liver parenchymal curve using the Johnson-Wilson model (20) with a software program developed in our laboratory. The sum of squared deviations of the fitted curve from the measured liver parenchymal or tumor contrast enhancement curves was minimized to determine the optimal weights of the aortic and portal venous curves as well as the optimal impulse residue function (IRF) according to the Johnson-Wilson model (20) (see Appendix B). As discussed in the Appendix B, the determined IRF is used to calculate the following functional parameters: hepatic blood flow (HBF), hepatic blood volume (HBV), capillary permeability surface area product (PS), appearance time of contrast in tissue relative to that in aorta (T_0), and hepatic arterial fraction (HAF) or the fraction of HBF that is derived from the hepatic artery as

opposed to the portal vein. Functional maps were generated by deconvolution as described above the liver or tumor enhancement curve corresponding to each voxel.

3.2.5 Data Analysis

From the set of five functional maps, four regions of interest (ROI) were drawn to measure perfusion and other available functional parameters (HBV, PS, T_0 , and HAF) in the tumor and adjacent normal tissue. The first ROI was drawn on the normal tissue in the HBF maps (ROI_{normal}). A second ROI, the tumor core (ROI_{core}) was drawn on areas with HBF less than or equal to 75% of that measured in ROI_{normal} . The corresponding T_0 map was used to draw a third region ROI_{T_0} covering the entire tumor, which comprised of the core of the tumor and adjacent tumor tissue. This region was drawn to include voxels where the T_0 was less than or equal to half of that in normal voxel. A fourth region, the rim of the tumor (ROI_{rim}) was defined as the difference between the ROI_{core} and ROI_{T_0} . Measurements were made using ROI_{core} , ROI_{rim} and ROI_{normal} ; the reported values reflect averages from 2 – 4 DCE-CT slices that cover a 1 - 2 cm slab through the tumor and normal liver parenchyma.

For quantitative analysis of the acquired [^{18}F] FDG-PET images, ROIs were drawn around areas with enhanced [^{18}F] FDG uptake relative to the adjacent normal tissue, which also encompassed the entire tumor (i.e. ROI_{T_0}) in the corresponding CT image. These regions were representative of the most metabolically active portion of the tumors and therefore likely represented areas with the most biologically aggressive behavior. [^{18}F] FDG uptake was measured in all drawn ROIs as whole body standardized

uptake value (SUV) in g mL^{-1} and the mean SUV over all slices covering the tumor was reported.

3.2.6 Statistical Analysis

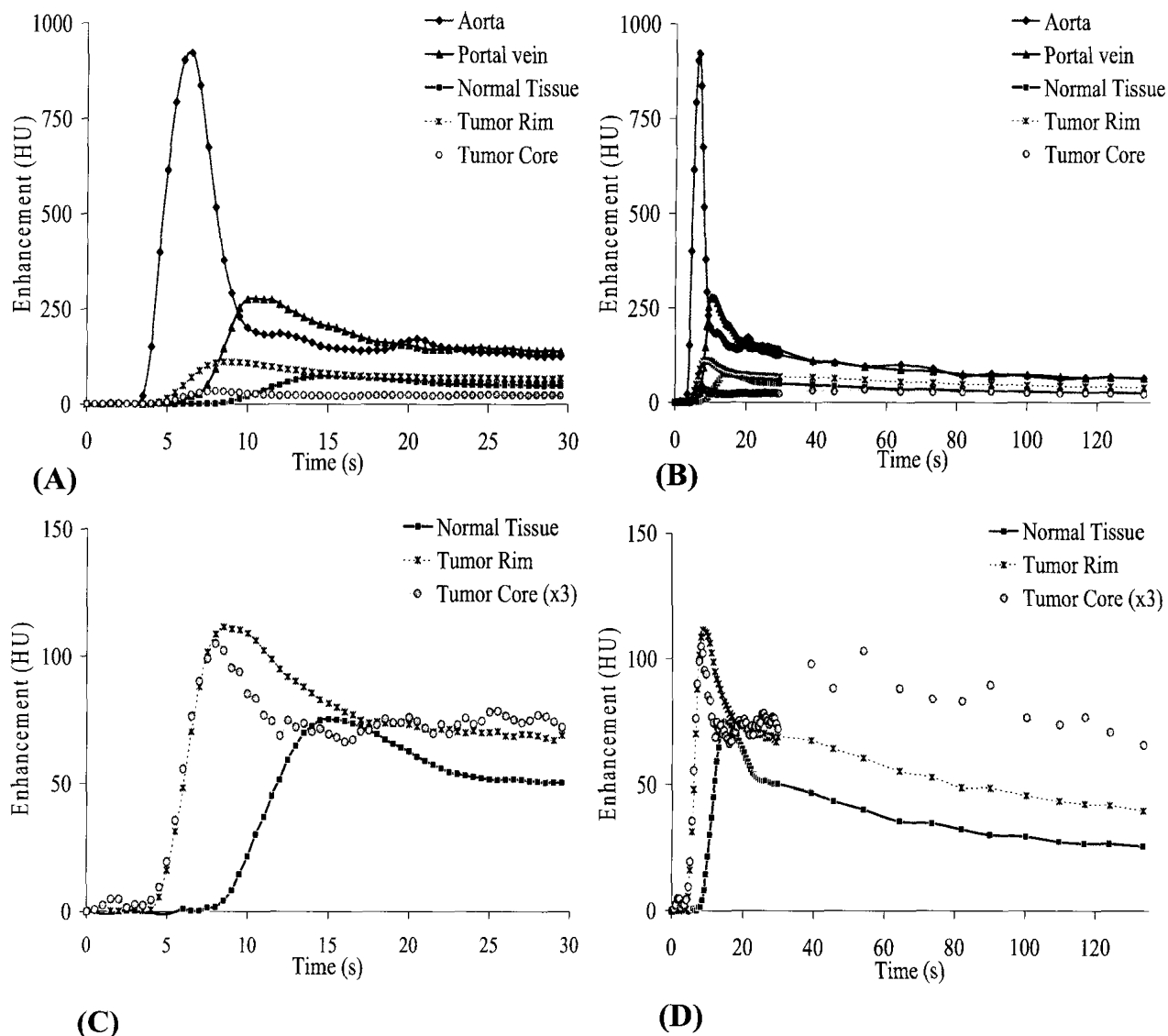
Statistical analysis was performed using SAS software (SAS system for Windows, Release 8.2; SAS Institute Inc., Cary NC). In order to account for the missing data, the MIXED procedure for repeated measures analysis of variance (ANOVA) was used. The design was completely within-subjects where time after initial detection and tissue type were the independent factors and CT functional parameters or SUV as dependent variables. The Tukey-Kramer multiple comparison tests were used for post-hoc comparisons with significance set at $P < 0.05$. Linear regression analysis was used to compare the SUV measured in the [^{18}F] FDG-PET images and to the HBF values derived by DCE-CT. To investigate the sensitivity of our results relative to the choice of thresholds, a series of different thresholds were investigated, such as: 75% HBF, 50% T_0 ; 65% HBF, 40% T_0 ; and 85% HBF, 60 % T_0 . This data was also analyzed using MIXED procedure for repeated measures ANOVA where time after initial detection, thresholds and tissue type were the independent factors and CT functional parameters as dependent variables.

3.3 RESULTS

Contrast enhancement curves from the aorta, portal vein, normal tissue and tumor shows that contrast appears much earlier in the tumor than in the adjacent normal tissue, Figure 3.1. The time taken for contrast to arrive at the tumor relative to the instant of

arrival at the aorta, or tumor T_0 , decreased by an average of $64.9 \pm 7.8 \%$ in the tumors compared to the adjacent normal liver tissue (data not shown). Using T_0 map and the contrast-enhanced CT images we were able to visually detect tumors as early as 4 days after they were implanted. However, since the time of initial detection varied among the rabbits (4 to 12 days), data was reported for baseline and days following the initial detection of the tumor. We were able to detect relatively small tumors with an average of diameter of 0.76 ± 0.14 cm at the initial detection which grew to 2.99 ± 0.90 cm at the end of the study. A comparison between [^{18}F] FDG-PET uptake, HBF and the T_0 maps at baseline, 8 and 16 days after the initial detection of the tumor illustrates how these functional parameters change with tumor growth, Figure 3.2. In these maps we were able to identify major blood vessels, the tumor, and observe the development of the hypovascular core.

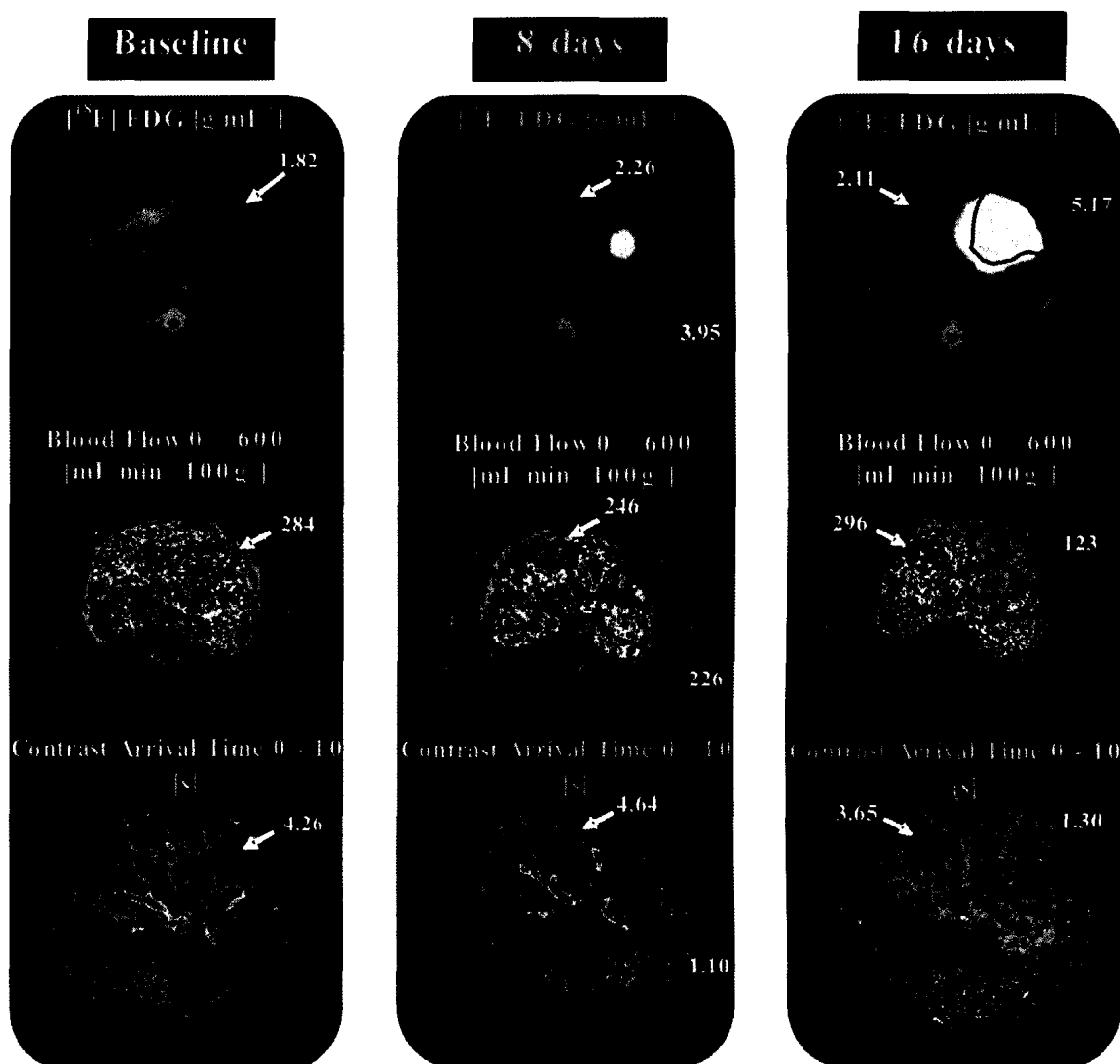
Figure 3.1: CT-measured contrast concentration (enhancement) curves



CT-measured contrast concentration (enhancement) curves of the aorta (diamond), portal vein (triangle), normal liver parenchyma (square), tumor rim (cross) and tumor core (circle) in a rabbit's liver. **A)** Enhancement curves taken from the first phase "breath hold" CT images. **B)** Enhancement curves from the co-registered first and second phase CT images; these curves were deconvolved to calculate the set of functional parameters: HBF, HBV, MTT, PS, HAF and T_0 . **C and D)** An enlarged view of the contrast enhancement curves measured in the tumor and normal liver tissue- the enhancement curve from the tumor core was multiplied by a factor of 3. **C)** During the first phase both the tumor and normal tissue enhancement did not return to baseline from peak enhancement - a result of contrast 'leaking' into the extra-vascular space. The curves also

show that contrast appeared in the tumor at the same time as in the aorta whereas it appeared in the normal tissue and in the portal vein at about the same time. This suggests that the tumor derived more of its blood supply from the hepatic artery; whereas normal tissue obtained more of its blood supply from the portal vein.

Figure 3.2: Comparison of CT and PET functional images



A comparison between [¹⁸F] FDG-PET images, HBF and T₀ maps at baseline, 8 and 16 days after the initial detection of the tumor, all in the axial plane of view. The white arrows indicate regions drawn on the normal tissue, while the red arrows indicate regions drawn on the tumors as they appear in the T₀ maps and then superimposed on the other

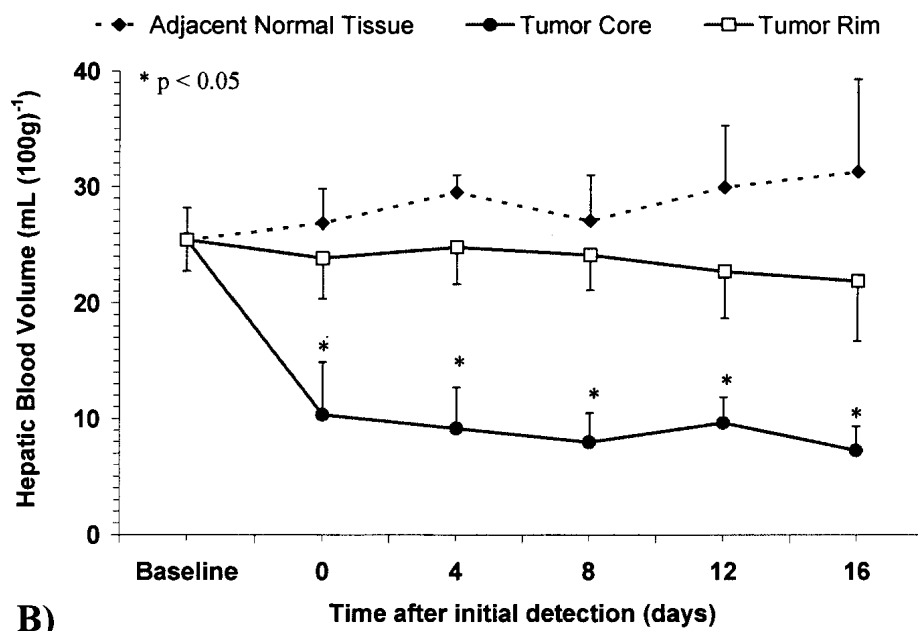
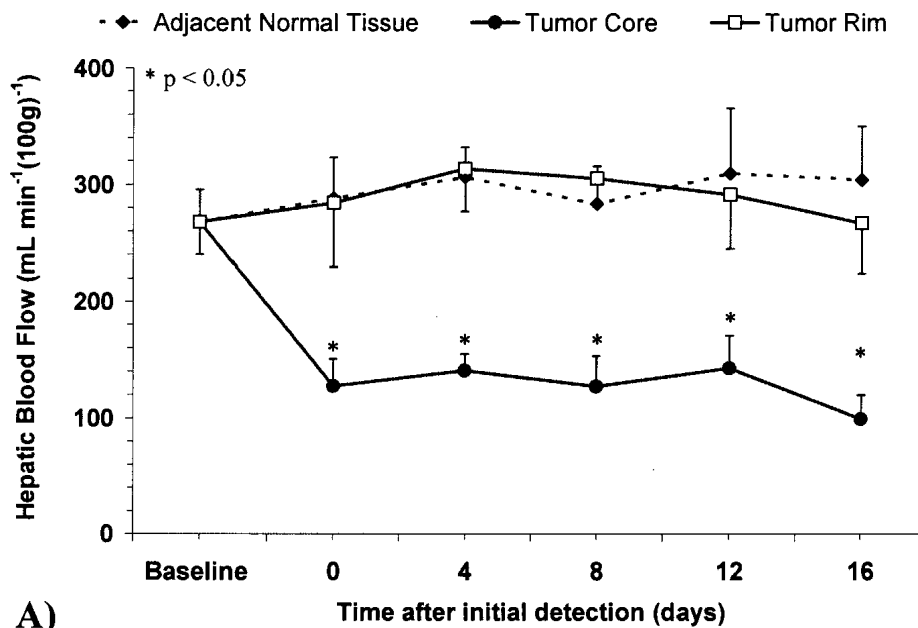
maps. **Top:** Fused [^{18}F] FDG-PET/CT images of the liver of a rabbit. **Middle:** HBF maps of the liver at the same slice locations as shown in the [^{18}F] FDG-PET scans. Sixteen days after the initial detection of the tumor there was a flow-glucose utilization mismatch at the center of the tumor, with comparatively less blood flow in the center than periphery of the tumor, but more or less uniform glycolytic activity maintained throughout the tumor. **Bottom:** Contrast arrival time maps, i.e. appearance time of contrast in tissue relative to that in aorta, show clearly that contrast arrived much earlier in the tumor than in the adjacent normal tissue. .

3.3.1 Hepatic Blood Flow and Volume

Using the thresholds described earlier, it was possible to delineate the tumor into two types of tissues: the hypovascular tumor core (ROI_{core}), and the tumor rim (ROI_{rim}). The repeated measures ANOVA showed no significant differences between perfusion and other functional parameters measured with regions created from thresholds of 75% HBF, 50% T_0 , and those measured with regions from the other thresholds, ($F(2, 12) = 0.63$, $P > 0.05$ and observed power = 0.17). Hence, all further analysis was performed using thresholds 75% HBF and 50% T_0 to delineate the tumor core. Both HBF and HBV were significantly different in the tumor core, tumor rim and normal tissue ($F(2, 12) = 148.22$, $P < 0.05$ and observed power = 1.0 for HBF and $F(2, 12) = 201.79$, $P < 0.05$ and observed power = 1.0 for HBV). Post-hoc tests revealed there were significant differences between HBF measured in the tumor core compared to the tumor rim and the normal tissue ($P < 0.05$). There were no significant differences between HBF measured in the normal tissue and tumor rim throughout the study period ($P > 0.05$), HBF remained relatively constant at 292 ± 37 and $289 \pm 41 \text{ mL min}^{-1} (100 \text{ g})^{-1}$ respectively, Figure 3.3 (A). At the initial detection of the tumor HBF and HBV in the tumor core dropped

significantly below baseline values in the normal tissue and tumor rim, ($P < 0.05$), Figure 3.3. Once the tumor was detected, the HBF and HBV in the tumor core remained stable at $127 \pm 23 \text{ mL min}^{-1} (100 \text{ g})^{-1}$ and $8.9 \pm 2.6 \text{ mL (100 g)}^{-1}$ respectively throughout the study, Figure 3.3. However, except at baseline there were significant differences between HBV measured in the normal tissue and tumor rim ($P < 0.05$); normal tissue and tumor core ($P < 0.05$), and tumor rim and core ($P < 0.05$) throughout the study, Figure 3.3 (B).

Figure 3.3: Changes in HBF and HBV measurement as the tumor develops



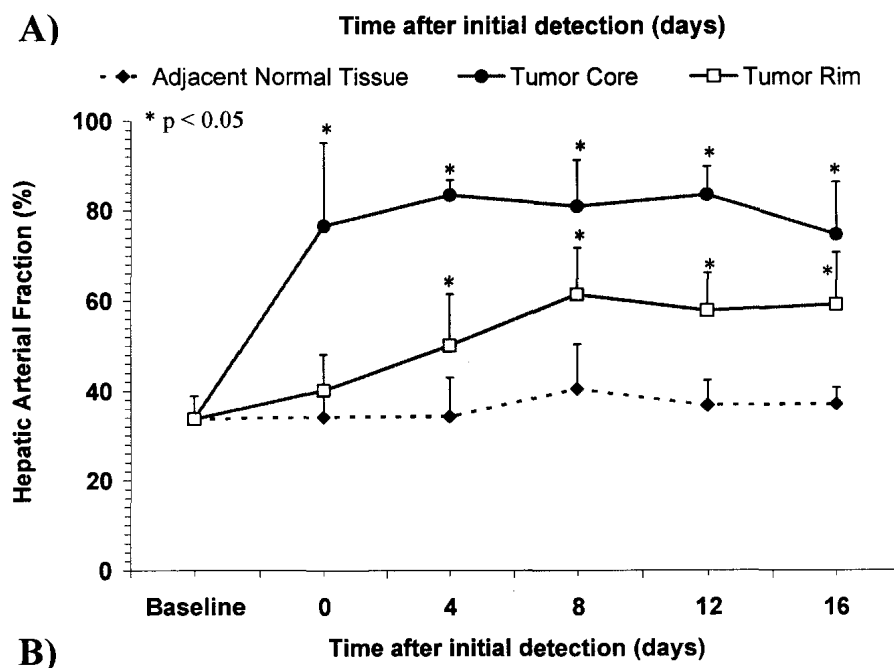
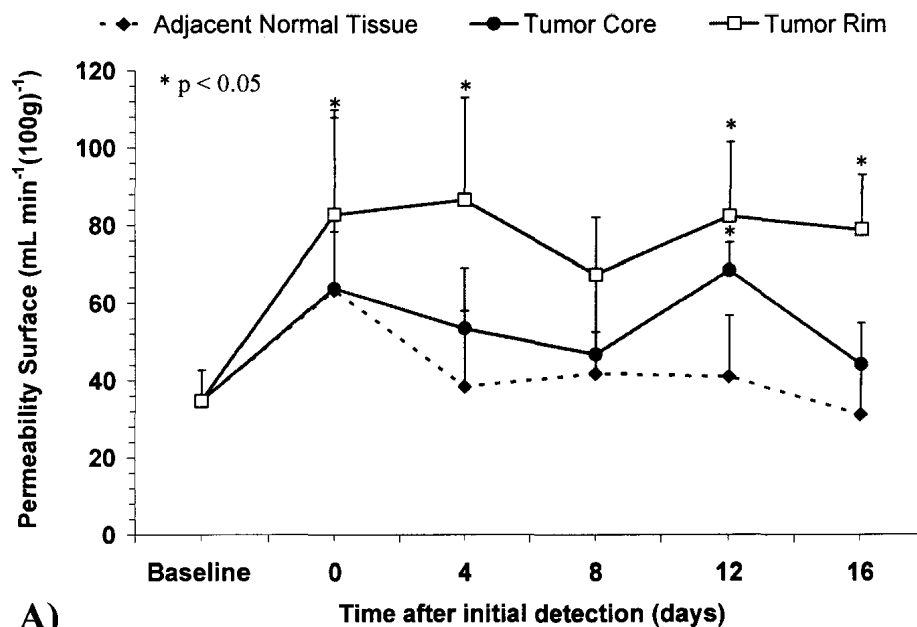
(A) Hepatic blood flow; and (B) hepatic blood volume measured (mean \pm SD) in the tumor compared to the adjacent normal tissue (diamond) throughout the study period. Each tumor was separated into two regions: the hypovascular core (circle) and the tumor rim (open square).

* Indicates significant difference from baseline using two-way ANOVA and post-hoc with the Tukey-Kramer multiple comparison test. For clarity other significant differences in either HBF or HBV are not shown but are discussed in the text.

3.3.2 Permeability Surface-Area Product and Hepatic Arterial Fraction

A comparison between the mean PS and HAF in the tumor and adjacent normal tissue at baseline and every 4 days after the initial detection of the tumor illustrates the difference between the two types of tissue, Figure 3.4. PS was significantly different in tumor core, tumor rim and normal tissue ($F(2, 12) = 20.43$, $P < 0.05$ and observed power = 1.0). Post-hoc tests revealed that at the initial detection of the tumor, PS in the tumor rim increased significantly above baseline ($P < 0.05$), adjacent normal tissue ($P < 0.05$) and tumor core ($P < 0.05$), and remained significantly above the baseline throughout the remainder of the experiment ($P < 0.05$) except for day 8, Figure 3.4 (A). However, there were no differences between PS in normal tissue and tumor core, except for day 12 in the tumor core ($P > 0.05$), Figure 3.4 (A). HAF was significantly different in tumor core, tumor rim and normal tissue ($F(2, 12) = 158.60$, $P < 0.05$ and observed power = 1.0). Post-hoc tests revealed that HAF in normal liver remained relatively constant at 36 ± 7 % throughout the study ($P > 0.05$), Figure 3.4 (B). At the initial detection of the tumor, the HAF in the tumor core increased twofold over the baseline and adjacent normal tissue value ($P < 0.05$). Conversely, HAF in the tumor rim gradually increased and was significantly different from normal tissue starting 4 days after the initial detection of the tumor ($P < 0.05$).

Figure 3.4: Changes in PS and HAF as the tumor develops



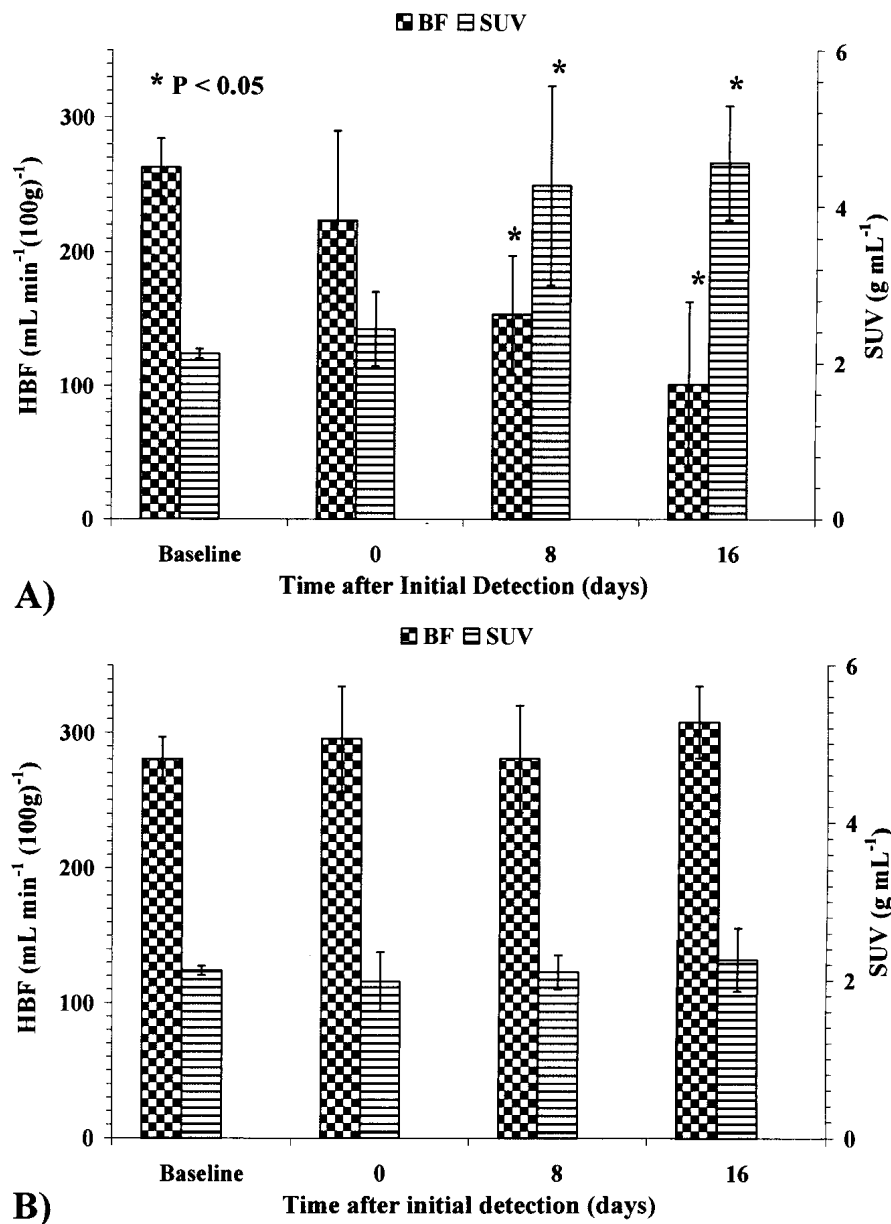
(A) Capillary permeability surface-area product (PS) and (B) hepatic arterial fraction (HAF) (mean \pm SD) as the implanted VX2 tumor grew. Each tumor was separated into two regions: the hypovascular core (circles) and the tumor rim (open squares). The normal liver tissue region (diamond) was also plotted for comparison.

* Indicates significant difference from baseline using two – way ANOVA and post-hoc with the Tukey-Kramer multiple comparison test. For clarity other significant differences in either PS or HAF are not shown but are discussed in the text.

3.3.3 Glucose uptake vs. Hepatic Blood Flow

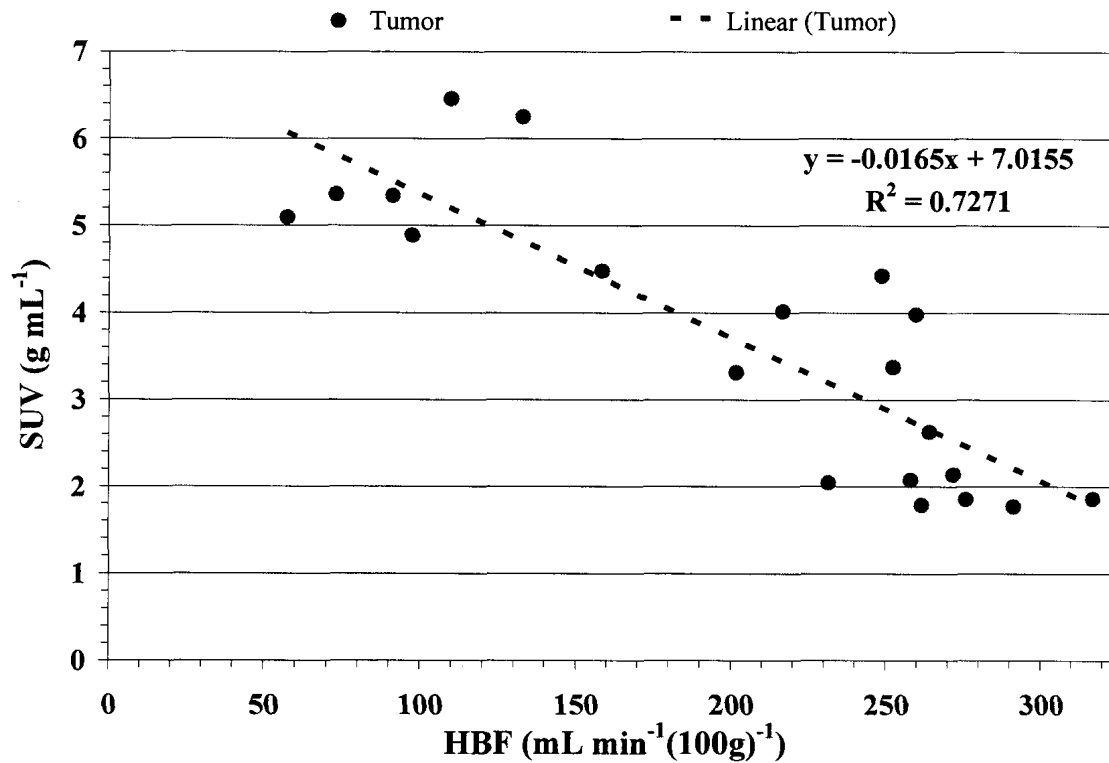
Both SUV and HBF in the tumor core were significantly different during the growth of the tumor ($F(3, 12) = 15.87, P < 0.05$ and observed power = 0.999) for SUV and ($F(3, 12) = 7.94, P < 0.05$ and observed power = 0.948) for HBF. In the hypovascular tumor core, post-hoc tests revealed: (i) SUV increased from 2.12 ± 0.06 at baseline to $4.56 \pm 0.73 \text{ g mL}^{-1}$ at the end of the study ($P < 0.05$) and; (ii) HBF decreased from 262 ± 22 to $101 \pm 62 \text{ mL min}^{-1} (100\text{g})^{-1}$ during the same period ($P < 0.05$), Figure 3.5(A). Conversely, SUV and HBF in the adjacent normal liver remained relatively constant around $2.12 \pm 0.27 \text{ g mL}^{-1}$ and $291 \pm 31 \text{ mL min}^{-1} (100\text{g})^{-1}$ ($P > 0.05$), Figure 3.5 (B). To explore the uncoupling between glucose utilization and blood flow, we plotted glucose uptake vs. HBF in all the tumors from baseline to the end of the study, Figure 3.6. A linear regression analysis showed an inverse correlation between tumor SUV and HBF, with R^2 of 0.727 ($P < 0.05$). This result shows that the spatial resolution of the PET scanner was sufficient for detecting regions of low [^{18}F] FDG uptake in the tumor core. The low [^{18}F] FDG uptake region in Figure 3.7 was in the tumor core and had prolonged T_0 and extremely low HBF of $87 \pm 4 \text{ mL min}^{-1} (100 \text{ g})^{-1}$ relative to normal liver.

Figure 3.5: Change in HBF and glucose utilization in tumors and normal tissue



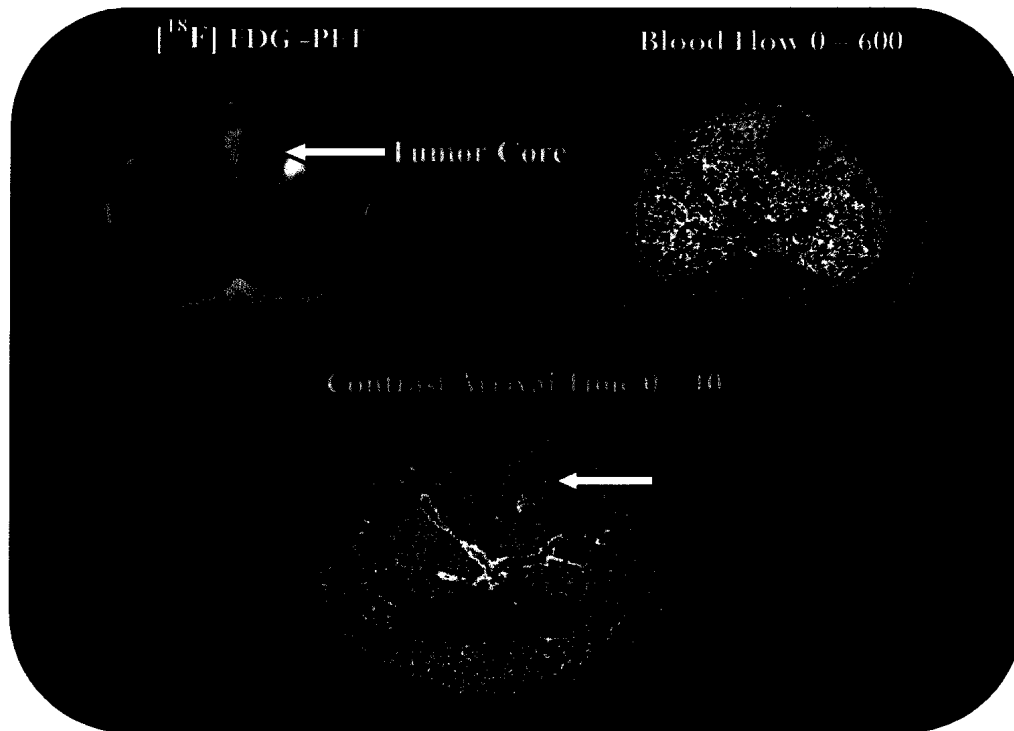
SUV vs. HBF (mean \pm SD) in the liver as the implanted VX2 tumor grew. **(A)** Shows the comparison between HBF (cross hatch) and SUV (line) in tumors. As the tumor grew the HBF decreased while the SUV increased, indicating a mismatch between blood flow and glucose utilization. **(B)** Shows the corresponding measurements in the adjacent normal tissue. These measurements show that both HBF and SUV remained relatively constant in normal tissue over time, $P > 0.05$.

* Indicates significant difference from baseline using two – way ANOVA and post-hoc with the Tukey-Kramer multiple comparison test.

Figure 3.6: Relationship between tumor SUV and HBF

The linear correlation between HBF (mL min⁻¹ 100g⁻¹) and [¹⁸F] FDG uptake (g mL⁻¹) for all tumors from baseline to the end of the study. A disparity between glucose uptake and blood flow was demonstrated, suggesting that the tumors were surviving via anaerobic glycolysis.

Figure 3.7: Development of hypo-vascular region in the tumor core



A comparison between $[^{18}\text{F}]$ FDG-PET scans, HBF and T_0 maps in an animal at the last day of the study, all in the axial plane of view. The white arrows indicate areas of low glycolytic activity inside the tumor and areas of increase contrast arrival time. The low FDG uptake in the center suggests that the spatial resolution of the PET scanner was sufficient to detect low SUV and blood flow in the tumor core.

3.4 DISCUSSION

The normal HBF value of $292 \pm 37 \text{ mL min}^{-1} (100\text{g})^{-1}$ measured in our study is consistent with values reported for total liver perfusion by Materne *et al* (21). Moreover, our perfusion data suggest that the growth of VX2 carcinoma is separated into two phases: a pre-vascular, and a vascular phase. The pre-vascular phase exists from 4 to 12 days after tumor cells were implanted, during which neither contrast enhanced CT nor [^{18}F] FDG-PET were able to detect the tumor. During this phase, the liver HBF remained stable at $288 \pm 13 \text{ mL min}^{-1} (100\text{g})^{-1}$ ($P > 0.05$). Conversely, during the vascular phase the tumor differentiated into two regions: the tumor rim and a hypovascular tumor core, Figure 3.3 (A), and there was a significant increase in HAF first in the tumor core and then in the tumor rim, Figure 3.4 (B).

Fukumura *et al* demonstrated that the vessel density in liver tumors was sevenfold lower than that in the normal liver and also that vessel density in the center of the tumor was significantly lower than that in the periphery (22). Similarly, our study shows significantly higher HBV in the tumor rim than in the tumor core, and lower HBV in the tumor than in the normal tissue, Figure 3.3 (B). The magnitude of the tumor HBF and HBV is likely dependent on the functional micro-vascular density or the perfused cross-sectional area and the velocity of flow through the vasculature. A high vascular density is a prerequisite for, but is not necessarily indicative of a high nutritive flow (23). Some tumors have diminished functionality, because of heterogeneous distribution of blood vessels with sluggish and intermitted flow (22, 23). Diminished micro-vascular function may lead to low HBV and deprive the central region of the tumor of a viable blood supply, which may lead to hypoxia or even necrosis and the uncoupling of glucose

utilization and blood flow as we have shown in our study. This is consistent with studies showing a correlation between tumor size and reduced blood flow and oxygen supply (7, 24).

In our study, the PS in the tumor rim was found to be significantly higher than that in the tumor core, normal tissue and at baseline, Figure 3.4. Claffey *et al.* showed a close correlation between vascular permeability factor (VPF)/vascular endothelial growth factor (VEGF) expression, micro-vascular hyper-permeability, and tumor induced angiogenesis. Conversely, low VPF/VEGF expression leads to extensive necrosis and poor vasculature (25). Hence, the high PS found in the tumor rim in our study could be an indication of high VPF/VEGF expression and tumor induced angiogenesis.

Similarly, the increase in HAF seen in the tumor core was possibly due to the recruitment of new blood vessels from the hepatic artery during angiogenesis. This suggests that the implanted VX2 carcinoma derived most of its' blood from the arterial rather than the portal circulation, in agreement with observations made by Miles *et al.* (15). Studies in tumors have shown a linear relationship between oxygen consumption and oxygen availability (7, 24). Any increase in the hepatic artery flow may lead to increased oxygen supply and therefore, increased metabolic rate. That is, there is a redistribution of HBF towards more oxygenated blood from the hepatic artery rather than de-oxygenated blood from the portal vein. However, in the tumor core, as the tumor growth accelerated, angiogenesis was unable to maintain an adequate blood supply to the tumor; consequently, contributing to the uncoupling of glucose utilization and blood flow.

As discussed in the DCE-CT scanning protocol, the locations of the four slices were directly transferable to the PET acquisitions, because the scanning table is common to the PET and CT scanner in a hybrid PET/CT scanner and we were careful not to disturb the positioning of the rabbit between the two types of scans. The [^{18}F] FDG - PET studies shows an uncoupling of glucose utilization and tumor hepatic blood flow, Figure 3.6. As the tumors grew, SUV increased and tumor HBF decreased, whereas the SUV and HBF in the normal tissue remained relatively constant, Figure 3.5 (B). The increase in glucose metabolism in the tumor core has been suggested to be due to an increased activity of glycolytic enzymes (26, 27). Monakhov *et al.* reported that hexokinase played an important role in this process (28). The disparity between glucose SUV and HBF in tumors suggests that there was limited supply of oxygen and tumor cells in this liver tumor model were surviving via anaerobic glycolysis. These results are consistent with rodent studies, where blood flow rates in most isografted rodent tumors decreased with increasing tumor size (29-31). More recently, Fukuda *et al.* showed a negative correlation between tumor glucose utilization, measured by SUV, and blood flow, measured by oxygen-15 labeled water and dynamic PET scanning in hepatocellular carcinoma and metastatic colon cancer patients (32). This is contrary to observations made in human breast cancer patients by Mankoff *et al.* and Zasadny *et al.*, where they both reported an increase in blood flow with an increase in tumor metabolic rate (4, 33). On the other hand, Mankoff *et al.* stated that the relationship between blood flow and tumor metabolic rate showed considerable dispersion and was highly variable (4).

There are several limitations with our study. The most important was the relatively high blood glucose level, on average $5.6 \pm 0.8 \text{ mmol L}^{-1}$ at the start of each [^{18}F] FDG

PET scan. In clinical studies patients were fasted from 4 - 6 h to reduce competition from plasma glucose and thus optimize and standardize tumor [^{18}F] FDG uptake (34). However, fasting rabbits to stabilize HBF and blood glucose level is impractical. It causes severe peristaltic movement, which leads to severe motion artifacts in the CT images. The high blood glucose level may lead to poor contrast between SUV in the tumor and normal tissue, and may have limited our ability to differentiate between tumor rim and core using [^{18}F] FDG – PET (35). However, our data suggests that even without fasting the spatial resolution of the PET scanner was sufficient to detect low SUV region in the tumor core, Figure 3.7. This suggests that contrast and glucose delivery to the tumor core was impeded, possibly due to necrosis.

Partial volume averaging (PVA) is an inherent source of error when imaging small objects (36). It causes the underestimation of enhancement and hence errors in the estimation of perfusion and related parameters in small objects. However, in our study, at the initial detection of the tumors, HBF, HBV and HAF in the tumor core were significantly different from adjacent normal tissue and tumor rim, Figure 3.3 and Figure 3.4 (B). This suggests that the spatial resolution of our functional imaging technique was able to separate the tumor rim from the normal tissue and tumor core from the tumor rim. Hence, the size limitation for regional functional imaging is probably between 0.59 and 1.03 cm diameter, which is the range of sizes of the initially detected tumors in the series.

In our study, 75 % of normal HBF and 50 % of normal T_0 were used as thresholds to delineate the tumor core from the rest of the tumor. The average HBF and T_0 used for the thresholds were $220 \pm 12 \text{ mL min}^{-1} (100 \text{ g})^{-1}$, and $2.1 \pm 0.1 \text{ s}$ respectively. The HBF threshold used was significantly higher than the HBF measured in the tumor core

throughout the study period, Figure 3.3 (A). This suggests that the low HBF measured in the tumor core was not an artifact introduced by the arbitrary choice of a low threshold. Moreover, analysis of the sensitivity of the thresholds showed no significant differences between perfusion and related functional parameters measured with regions created from thresholds of 75% HBF, 50% T_0 , and those measured with regions from the other thresholds, ($P > 0.05$) as discussed in the materials and methods.

In conclusion, there was a mismatch between tumor blood flow and glucose uptake in the tumor core. A possible interpretation of this result is that the tumor core is dependent on anaerobic glycolysis for survival, hence could be hypoxic. This later prediction remains unproven in our study, because we have not evaluated hypoxia with other hypoxic markers or direct oxygen tension measurements.

3.5 REFERENCES

1. Johnson PC. Autoregulation of blood flow. *Circ Res* 1986; 59:483-495.
2. Jones RD, Berne RM. Evidence for a metabolic mechanism in autoregulation of blood flow in skeletal muscle. *Circ Res* 1965; 17:540-554.
3. Lehtio K, Oikonen V, Gronroos T, et al. Imaging of blood flow and hypoxia in head and neck cancer: initial evaluation with [(15)O]H(2)O and [(18)F]fluoroerythronitroimidazole PET. *J Nucl Med* 2001; 42:1643-1652.
4. Mankoff DA, Dunnwald LK, Gralow JR, et al. Blood Flow and Metabolism in Locally Advanced Breast Cancer: Relationship to Response to Therapy. *J Nucl Med* 2002; 43:500.
5. McFalls EO, Murad B, Haspel HC, Marx D, Sikora J, Ward HB. Myocardial glucose uptake after dobutamine stress in chronic hibernating swine myocardium. *J Nucl Cardiol* 2003; 10:385-394.
6. Sokoloff L. Relationships among local functional activity, energy metabolism, and blood flow in the central nervous system. *Fed Proc* 1981; 40:2311-2316.
7. Kallinowski F, Schlenger KH, Kloes M, Stohrer M, Vaupel P. Tumor blood flow: the principal modulator of oxidative and glycolytic metabolism, and of the metabolic micromilieu of human tumor xenografts in vivo. *Int J Cancer* 1989; 44:266-272.
8. Brown RS, Fisher SJ, Wahl RL. Autoradiographic evaluation of the intra-tumoral distribution of 2-deoxy-D-glucose and monoclonal antibodies in xenografts of human ovarian adenocarcinoma. *J Nucl Med* 1993; 34:75-82.
9. Kubota R, Kubota K, Yamada S, Tada M, Ido T, Tamahashi N. Active and passive mechanisms of [fluorine-18] fluorodeoxyglucose uptake by proliferating and preneoplastic cancer cells in vivo: a microautoradiographic study. *J Nucl Med* 1994; 35:1067-1075.
10. Teicher BA. Hypoxia and drug resistance. *Cancer Metastasis Rev* 1994; 13:139-168.
11. Lee TY. Functional CT: physiological models. *Trends Biotechnol* 2002; 20:s3-s10.
12. Brix G, Ziegler SI, Bellemann ME, et al. Quantification of [(18)F]FDG uptake in the normal liver using dynamic PET: impact and modeling of the dual hepatic blood supply. *J Nucl Med* 2001; 42:1265-1273.
13. Graham MM, Peterson LM, Hayward RM. Comparison of simplified quantitative analyses of FDG uptake. *Nucl Med Biol* 2000; 27:647-655.

14. Ackerman NB. The blood supply of experimental liver metastases. IV. Changes in vascularity with increasing tumor growth. *Surgery* 1974; 75:589-596.
15. Miles KA, Hayball MP, Dixon AK. Functional images of hepatic perfusion obtained with dynamic CT. *Radiology* 1993; 188:405-411.
16. Van Beers BE, Leconte I, Materne R, Smith AM, Jamart J, Horsmans Y. Hepatic perfusion parameters in chronic liver disease: dynamic CT measurements correlated with disease severity. *AJR Am J Roentgenol* 2001; 176:667-673.
17. Richardson PD, Withrington PG. Liver blood flow. I. Intrinsic and nervous control of liver blood flow. *Gastroenterology* 1981; 81:159-173.
18. Schenk WG Jr, McDonald JC, McDonald K, Drapanas T. Direct measurement of hepatic blood flow in surgical patients: with related observations on hepatic flow dynamics in experimental animals. *Ann Surg* 1962; 156:463-471.
19. Hamacher K, Coenen HH. Efficient routine production of the ¹⁸F-labelled amino acid O-2-¹⁸F fluoroethyl-L-tyrosine. *Appl Radiat Isot* 2002; 57:853-856.
20. Johnson JA, Wilson TA. A model for capillary exchange. *Am J Physiol* 1966; 210:1299-1303.
21. Materne R, Van Beers BE, Smith AM, et al. Non-invasive quantification of liver perfusion with dynamic computed tomography and a dual-input one-compartmental model. *Clin Sci (Lond)* 2000; 99:517-525.
22. Fukumura D, Yuan F, Monsky WL, Chen Y, Jain RK. Effect of host microenvironment on the microcirculation of human colon adenocarcinoma. *Am J Pathol* 1997; 151:679-688.
23. Folkman J. Tumor angiogenesis. In: Loitta LA, Mendelsohn J., Isreal MA eds. *The Molecular Basis of cancer*. 1 ed. Philadelphia: WB Saunders, 1995; 206-232.
24. Manz R, Otte J, Thews G, Vaupel P. Relationship between size and oxygenation status of malignant tumors. *Adv Exp Med Biol* 1983; 159:391-398.
25. Claffey KP, Brown LF, del Aguila LF, et al. Expression of vascular permeability factor/vascular endothelial growth factor by melanoma cells increases tumor growth, angiogenesis, and experimental metastasis. *Cancer Res* 1996; 56:172-181.
26. Weber G. Enzymology of cancer cells (second of two parts). *N Engl J Med* 1977; 296:541-551.
27. Weber G. Enzymology of cancer cells (first of two parts). *N Engl J Med* 1977; 296:486-492.

28. Monakhov NK, Neistadt EL, Shavlovskil MM, Shvartsman AL, Neifakh SA. Physicochemical properties and isoenzyme composition of hexokinase from normal and malignant human tissues. *J Natl Cancer Inst* 1978; 61:27-34.
29. Ward-Hartley KA, Jain RK. Effect of glucose and galactose on microcirculatory flow in normal and neoplastic tissues in rabbits. *Cancer Res* 1987; 47:371-377.
30. DiPette DJ, Ward-Hartley KA, Jain RK. Effect of glucose on systemic hemodynamics and blood flow rate in normal and tumor tissues in rats. *Cancer Res* 1986; 46:6299-6304.
31. Vaupel P, Thews G. Pathophysiological aspects of glucose uptake by the tumor tissue under various conditions of oxygen and glucose supply. *Adv Exp Med Biol* 1976; 75:547-553.
32. Fukuda KI, Taniguchi H, Koh T, Kunishima S, Yamagishi H. Relationships between oxygen and glucose metabolism in human liver tumours: positron emission tomography using ¹⁵O and ¹⁸F-deoxyglucose. *Nucl Med Commun* 2004; 25:577-583.
33. Zasadny KR, Tatsumi M, Wahl RL. FDG metabolism and uptake versus blood flow in women with untreated primary breast cancers. *Eur J Nucl Med Mol Imaging* 2003; 30:274-280.
34. Iwata Y, Shiomi S, Sasaki N, et al. Clinical usefulness of positron emission tomography with fluorine-18-fluorodeoxyglucose in the diagnosis of liver tumors. *Ann Nucl Med* 2000; 14:121-126.
35. Cremerius U, Bares R, Weis J, et al. Fasting improves discrimination of grade 1 and atypical or malignant meningioma in FDG-PET. *J Nucl Med* 1997; 38:26-30.
36. Cenic A, Nabavi DG, Craen RA, Gelb AW, Lee TY. Dynamic CT measurement of cerebral blood flow: a validation study. *AJNR Am J Neuroradiol* 1999; 20:63-73.

CHAPTER 4: DCE-CT PERFUSION IDENTIFY DIFFERENTIAL HEPATIC BLOOD FLOW RESPONSE DURING THALIDOMIDE INDUCED TUMOR VASCULAR NORMALIZATION

The content of this chapter have been adapted from the paper entitled “DCE-CT perfusion identify differential hepatic blood flow response during thalidomide induced tumor vascular normalization”, submitted for publication to the journal *Clinical Cancer Research* (2009) by Errol E. Stewart, Hongtao Sun, Xiaogang Chen, Peter H. Schafer, Yong Chen, Bertha M. Garcia, Ting-Yim Lee

4.1 INTRODUCTION

As tumors grow, the demand for oxygenated blood to support increased metabolic activity is met by the formation of new blood vessels from sprouts and branches of pre-existing capillaries through a process known as angiogenesis (1). The newly formed tumor blood vessels are structurally and functionally abnormal with defective endothelium, basement membrane, and pericyte coverage (2). Pericytes are required to stabilize the newly formed vessels, modulate blood flow and vascular permeability and regulate endothelial cells (EC) proliferation, survival, migration, differentiation and branching (3). Several reports have indicated that the consequence of insufficient pericyte coverage (immature vessels) are increased EC proliferation, high permeability, vessel enlargement, hemorrhage, impaired blood flow and hypoxia (4-6). Since coverage of the vessel wall with pericytes is a hallmark of vessel maturity (1, 7) and mature vessels are

more likely to conduct blood flow, tumor perfusion may indicate the degree of association between pericytes and the vessel wall.

Angiogenesis inhibitors have had mixed results in cancer treatment, showing positive effects in animal models but limited benefits in clinical trials (8). In contrast, angiogenesis inhibitors with adjuvant chemo- or radiation therapy have produced synergistic beneficial response in both animal and clinical trials (9-12). The exact mechanisms for this synergistic benefits are still unknown, however Jain (13) postulated that angiogenesis inhibitors selectively prune away sprouting vasculature leading to a transient normalization of the tumor vasculature that increases pericyte coverage and perfusion and sensitizes tumors to both chemo- and radiation therapy. Other studies have shown that angiogenesis inhibitors may decrease tumor blood flow and oxygenation, thereby compromising the outcome of radiotherapy (14, 15).

The controversy about the efficacy of combined therapy may be due to the relative timing of angiogenesis inhibitor and radiation therapy. Likewise, vessel maturity, which varies among tumor types, locations, and the stage of growth, plays an important role in determining the effectiveness of anti-vascular therapies (16, 17). Lin and Sessa (18) argued that knowledge of the 'normalization window' in which vessels become normalized is required to optimize adjuvant cytotoxic therapies with angiogenesis inhibitors. During this period tumor blood flow and oxygenation transiently increase, making chemo- or radiation therapy more effective (18). Furthermore, Jain (19) suggested that identifying the timing of the normalization of tumor vessels, to optimize the effect of angiogenesis inhibitors, requires a non-invasive imaging technique that can measure spatial and temporal changes in blood flow and other physiological parameters

at high spatial resolution. Stewart *et al.* validated a new dynamic contrast-enhanced (DCE) Computed Tomography (CT) technique that can non-invasively measure hepatic perfusion at high spatial resolution (20). Here we monitored tumor blood flow after treatment with thalidomide, which is known to inhibit vascular endothelial growth factor (VEGF) and basic fibroblast growth factor and causes vascular normalization (9, 21-23), and asked whether it could be used to identify which animal will have progression free survival. We identified a differential blood flow response in the therapy group with serial measurement of liver perfusion and identified vascular normalization with histological analysis.

4.2 MATERIALS AND METHOD

4.2.1 Animal Model

Twenty healthy male New Zealand White rabbits (3.0 – 3.5 kg) were used in these experiments. The experimental procedures were approved by the local Animal Use Subcommittee of the Canadian Council on Animal Care. VX2 carcinoma implanted in the rabbit liver was used as a model for hepatocellular carcinoma (HCC); it is a well established model for the investigation of chemoembolization therapies of HCC and its' blood supply is similar to many human liver tumors (24-26). One ear vein of the rabbit was cannulated for drugs and contrast injection (Omnipaque 300 diluted to 200 mg iodine ml⁻¹; GE Healthcare, Wisconsin, USA). Each animal was anesthetized and mechanically ventilated at a rate of 20 breathes per min to steady state normo-capnic conditions with a mixture of oxygen and 1.5 minimum alveolar concentrations of isoflurane. Body temperature was monitored with a rectal probe and maintained between 38.5 and 39.5 °C

with a heated re-circulating water blanket. Tumor cells were harvested from a VX2 carcinoma grown in a leg of a donor rabbit. Subsequently, 0.20 ml of these harvested cells suspended in Hank's Balanced Salt Solution (Sigma-Aldrich Canada Ltd., Ontario Canada) was injected directly into the liver of a rabbit.

4.2.2 Treatment Protocol

The animals were randomly assigned into a therapy ($n = 12$) and a control group ($n = 8$). Following implantation of the tumor cells, CT scans (helical and DCE-CT) were performed every 4 days to monitor for the development of tumor and measurement of liver perfusion. Thalidomide (Celgene Corp., Summit, NJ, USA), dissolved in dimethyl sulfoxide (DMSO) and sterile water (Sigma-Aldrich Canada Ltd.) at a ratio of 1:10, was administered at a dosage of $200 \text{ mg}\cdot\text{kg}^{-1}$ via an intraperitoneal injection once per week and a subcutaneous injection on subsequent days in the therapy group. An equivalent volume of DMSO and sterile water (vehicle) was given to the control group. The treatment with thalidomide or vehicle started when the tumor reached a size of 0.7 ± 0.1 cm in diameter and continued until metastatic lung nodules (a marker of disease progression) were observed in the helical CT scans or 40 days after the start of therapy. At the end of the study the rabbits were euthanized and perfusion-fixed with buffer solution and paraformaldehyde and the liver was harvested.

4.2.3 CT Scanning Protocol

CT scanning was performed with a LightSpeed CT scanner (GE Healthcare) following stabilization of blood gas at normo-capnic levels. Respiratory reflex was

suppressed with pancuronium bromide if required; prior to the start of all scans ventilation was suspended to eliminate motion from breathing. To assess the tumor burden a helical scan that covered the entire lung and liver were performed. The dynamic contrast enhanced (DCE)-CT scans were performed 15 min after the helical scan. Four 5 mm thick slices covering the liver were scanned for two and half minutes with a two-phase protocol as described by Stewart *et al.* (20).

4.2.4 Immunohistochemical Staining

The liver lobe with the tumor was cut into 5 mm thick blocks to match the slices from the DCE-CT study, fixed in 10% buffered paraformaldehyde, embedded in paraffin, and cut into 5 μ m thick sections. For regular light microscopy, the sections were stained with hematoxylin and eosin (H&E). For immunohistochemical staining, the sections were deparaffinized and heated in Tris-EDTA buffer (10mM Tris-Base, 2 mM EDTA, 0.05% Tween-20, pH 9.0) to retrieve antigens. The sections were blocked for 30 minutes in 5-10% blocking serum and incubated with primary antibodies for 1 hour at room temperature. The following primary antibodies were used: monoclonal mouse vimentin (clone V9; DAKO, Carpinteria, CA), monoclonal mouse anti-human α -smooth muscle actin (α -SMA) (clone 1A4; DAKO), monoclonal mouse pan Cytokeratin antibody (clone PCK-26; Abcam, Cambridge, MA) and monoclonal mouse anti-human CD31 (clone JC70A; DAKO). Negative control stains were obtained by substituting non-immune serum for the primary antibody. For example, in the case of α -SMA, isotype control IgG2a was also used in place of clone 1A4. Diaminobenzidine (DAB) was used as chromogen (brown) for detection of α -SMA, followed by hematoxylin counterstaining.

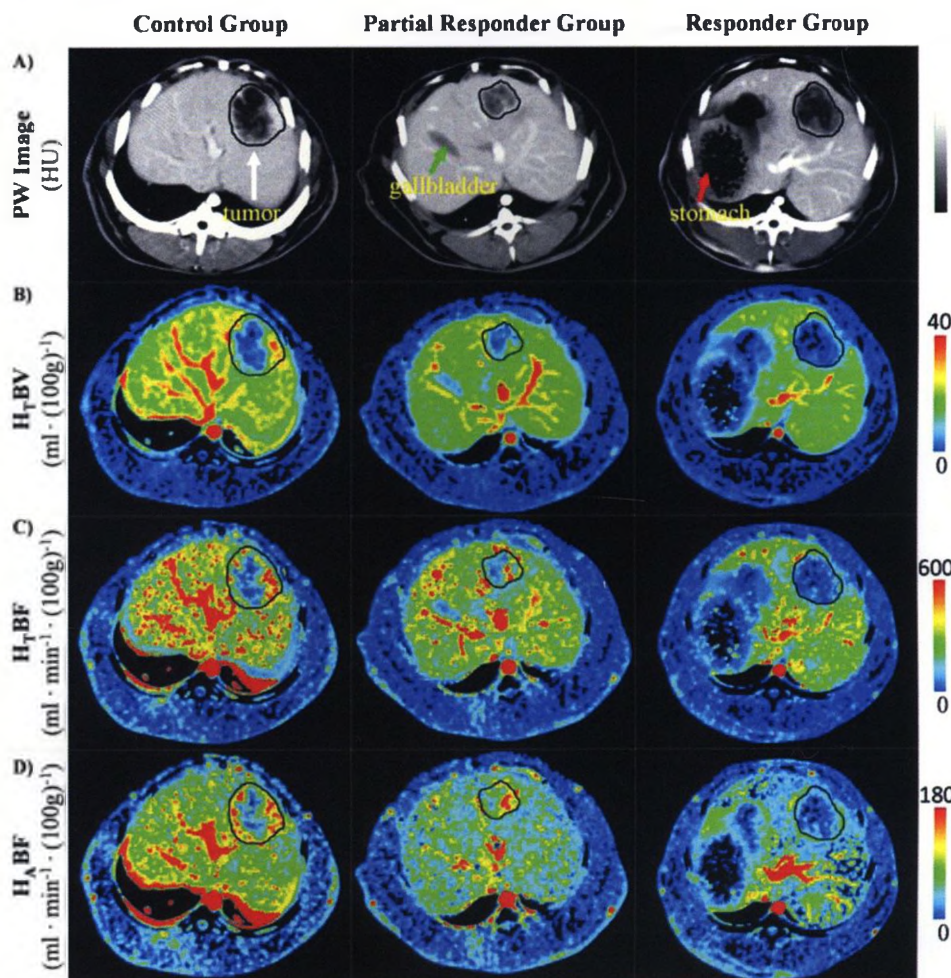
4.2.5 Data Analysis

The therapy group was sub-divided into animals that survived for more than 24 days after the start of therapy without lung metastasis (responder group, $n = 5$), or animals that survived for less than 24 days (partial responder group, $n = 7$). Parametric maps of total hepatic blood volume (H_TBV), total hepatic blood flow (H_TBF), hepatic artery blood flow (H_ABF) and the perfusion weighted (PW) image, which was the average of all DCE-CT images, for each CT slice were generated using the method described by Stewart *et al.* (20). In brief, the hepatic artery and the portal vein concentration of contrast were accepted as the dual inputs to the Johnson and Wilson model, which was solved with an adiabatic approximation to account for the distribution of intravenously injected iodinated contrast in the liver(20). The hepatic arterial fraction (α) represents the fraction of blood flow that perfuses the liver with oxygenated blood via the hepatic artery such that $H_ABF = \alpha \times H_TBF$.

The PW image and functional maps of H_TBV , H_TBF and H_ABF were imported into custom software (IDL v6.2; RSI Inc., Boulder, Colorado, USA) for analysis. In the PW image, the tumor rim appeared hyper-enhanced relative to the tumor core and normal tissue; this allowed us to segment the tumor from the surrounding normal tissue by drawing a region of interest (ROI) around the tumor, Figure 4.1 (A). The resulting ROI was applied to all available functional maps to obtain average values of the functional parameters in the entire tumor. To reduce variability from individual animal differences, the functional measurements from an animal were normalized by the initial measurements from the same animal prior to therapy. The tumor volume was measured from the helical scans using commercially available software (Volume Viewer 3.064, GE

Healthcare). Histological analysis was performed using the NIH ImageJ software v1.41n. For each slide, H&E images were captured at five random 2.10 mm² fields at low power ($\times 100$) and 0.247 mm² fields at high power ($\times 400$) magnifications. From these images the area fraction of hemorrhage and the nuclei density were determined. The micro-vascular density (MVD) and vessel diameter was determined from five random CD31 images at 0.556 mm² fields at ($\times 200$) magnification.

Figure 4.1: Dynamic Contrast Enhanced CT Perfusion Maps



A comparison of parametric maps in the control, partial responder and responder group 8 days after the start of thalidomide therapy. **A)** The PW image was created by averaging DCE-CT images acquired in the 1st phase of the scanning protocol. Since the concentration of contrast in the blood vessels and tumor rim was high during the first 30 s of scanning, the PW image was used to outline the tumor. The arrows indicate features such as the stomach, gallbladder and tumor. **B)** The H_TBV map represents the combined measure of functional micro-vascular density and diameter (perfused cross-sectional area) because it reflects the pooling of blood in functioning blood vessels. **C)** The H_TBF map represents total supply of blood flow to the liver from the hepatic artery (oxygenated) and the portal vein (deoxygenated). **D)** The H_ABF map was computed from the combination of the H_TBF and α (not shown); it reflects the oxygenated blood flow arriving from the hepatic artery.

4.2.6 Statistical Analysis

An omnibus test for differences among the measurements in the three groups: control, partial responder and responder was performed with analysis of variance (ANOVA) for repeated measures (SPSS Inc, Chicago, Illinois). A post-hoc Tukey test was used to compare differences between groups. All statistical tests were two-sided. Mann-Whitney rank test was used when data failed normality. The effect of thalidomide on survival was determined by Kaplan-Meier analysis. All data was reported as mean \pm standard error, and significance was set at $P < 0.05$.

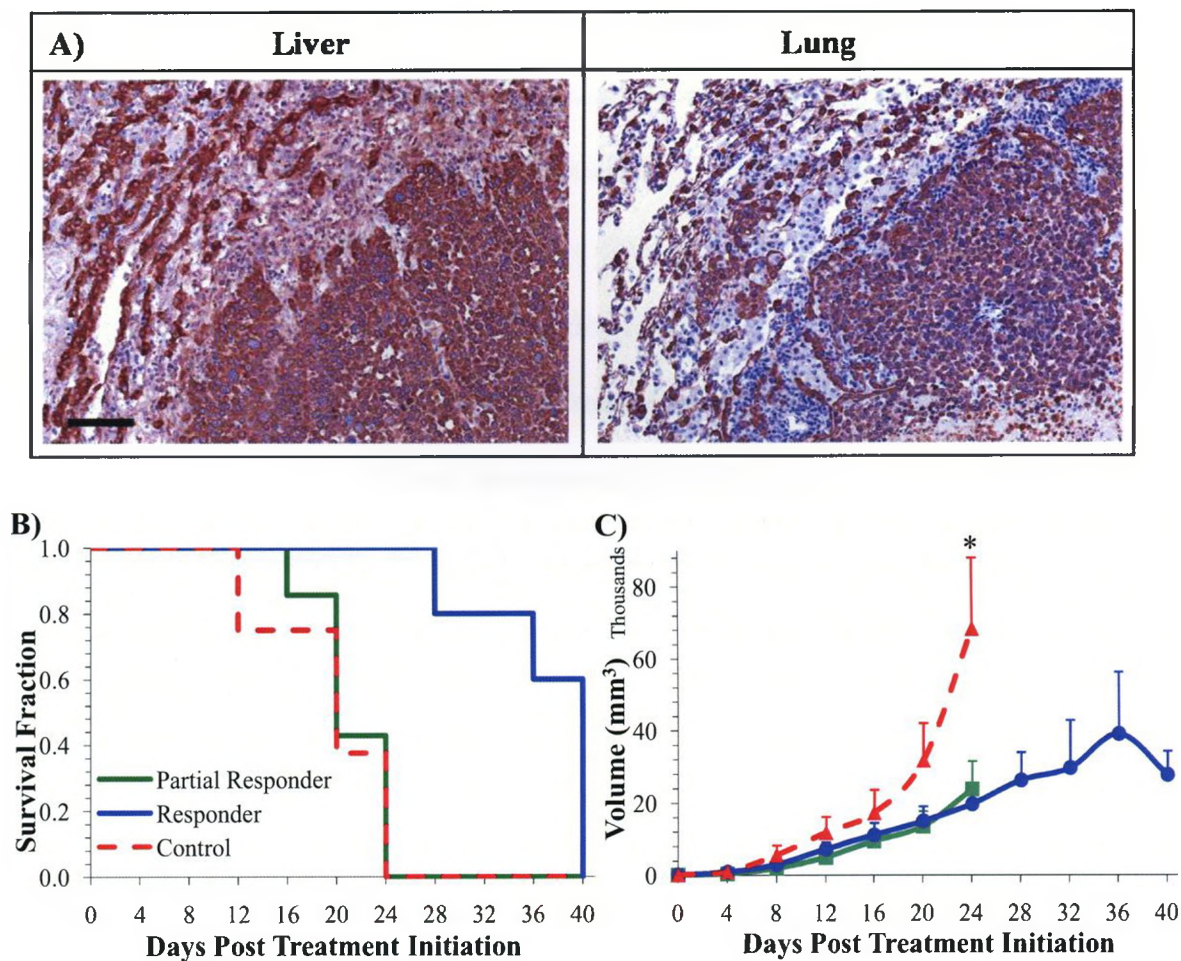
4.3 RESULTS

The functional maps of H_TBV , H_TBF , H_ABF and PW image from a rabbit at 8 days after the start of therapy are illustrated in Figure 4.1. All the functional maps show a complete suppression of perfusion in tumors in the responder group, Figure 4.1. The H_TBV and H_TBF maps from the control group show that the tumor developed a vascular rim and a hypo-vascular core; whereas tumor perfusion from the responder group was low and homogenous without the appearance of a vascular rim, Figure 4.1 (B) to (D). The H_ABF maps show a heterogeneous distribution of elevated H_ABF in tumors from the control and the partial responder group, Figure 4.1 (D).

Immunostaining showed positive pan-cytokeratin stains in the liver tumor and lung metastasis, which indicates that the tumors in both sites were derived from VX2 carcinoma and composed of epithelial cells, Figure 4.2 (A). The slides also show positive stains in the normal lung alveoli and liver parenchyma. The Kaplan-Meier survival curves for the control, partial responder and responder group are illustrated in Figure 4.2

(B). Thalidomide increased lung metastasis free survival in the responder group to a mean of 37 ± 2 days after the start of therapy, compared to 20 ± 2 and 21 ± 1 days for the control and partial responder group ($P < 0.05$). Three of the five animals in the responder group had lung metastasis free survival until the study end point at 40 days after the start of therapy. The tumor volume in the control group was significantly larger than those in the partial responder and responder group, $P < 0.05$; whereas, there was no significant difference between the partial responder and responder group, Figure 4.2 (C).

Figure 4.2: Tumor Progression and Survival of Animals with Hepatic Tumors

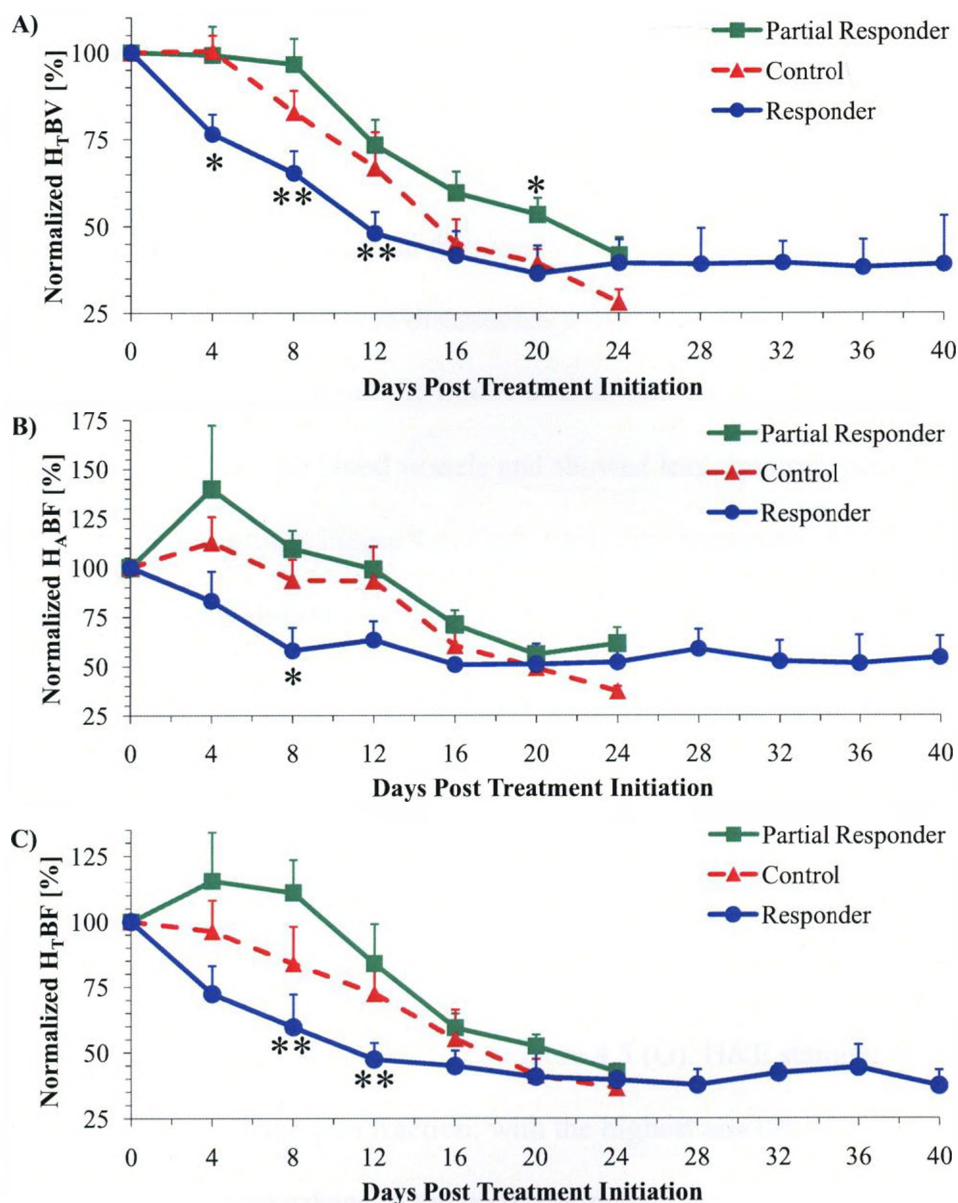


A) Immunohistochemical stains showing pan-cytokeratin antigen (brown stain) in the liver tumor and the lung metastasis at low power, the bar represents 100 μm . The positive pan-cytokeratin stain indicates the presents of epithelial cells. **B)** Kaplan-Meier survival curves for the control, partial responder and responder group. The mean survival in the responder group was 37 ± 2 days after the start of therapy compared to 20 ± 2 and 21 ± 1 days for the control and partial responder group ($P < 0.05$). **C)** The change in liver tumor volume in the control (triangle), partial responder (square) and responder (circle) group.

* Tukey test indicates significant difference from the other groups, $P < 0.05$

Thalidomide induced a differential perfusion change in the treated group; the most significant changes occurred during the first 8 days after the start of therapy, Figure 4.3. During this period, H_TBV in the responder group decreased by $35 \pm 6\%$ relative to day 0, $P < 0.05$ while that in the partial responder and control group remained stable with a non-significant trend of decrease by 3 ± 7 and $17 \pm 6\%$ respectively, Figure 4.3 (A). The corresponding H_TBF in the responder group decreased by $40 \pm 12\%$ compared to before treatment, $P < 0.05$ while those in the partial responder and control group showed a non-significant increase of $11 \pm 12\%$ and decrease of $16 \pm 14\%$ respectively, Figure 4.3 (B). Likewise, H_ABF decreased by $42 \pm 12\%$ relative to day 0 in the responder group, $P < 0.05$ while those in the partial responder and control group showed a non-significant increase of $10 \pm 9\%$ and decrease of $6 \pm 10\%$ respectively, Figure 4.3 (C).

Figure 4.3: Hepatic Perfusion in Animals Treated With Thalidomide



Perfusion measured in the tumor prior (day 0) to and every 4 days after the start of therapy. All data was normalized to that obtained in the same animal at day 0, to account for variations in the initial perfusion measurements among the animals prior to therapy.

A) Normalized hepatic blood volume ($H_{T}BV$), **B)** normalized total hepatic blood flow ($H_{T}BF$) and **C)** normalized hepatic artery blood flow ($H_{A}BF$) are shown in the figures.

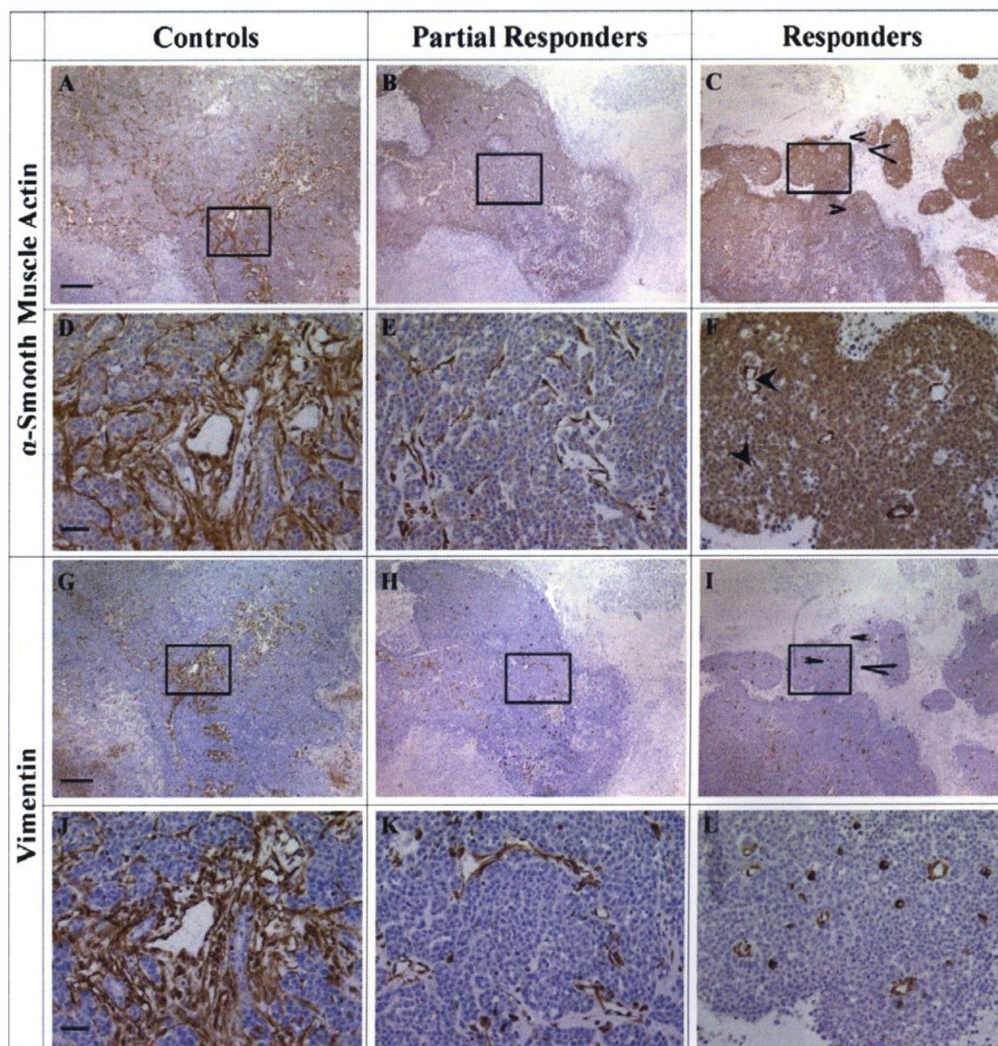
Data reported as mean \pm standard error.

* Tukey test indicates significant difference from the other groups, $P < 0.05$

** Tukey test indicates significant difference from the partial responder group, $P < 0.05$

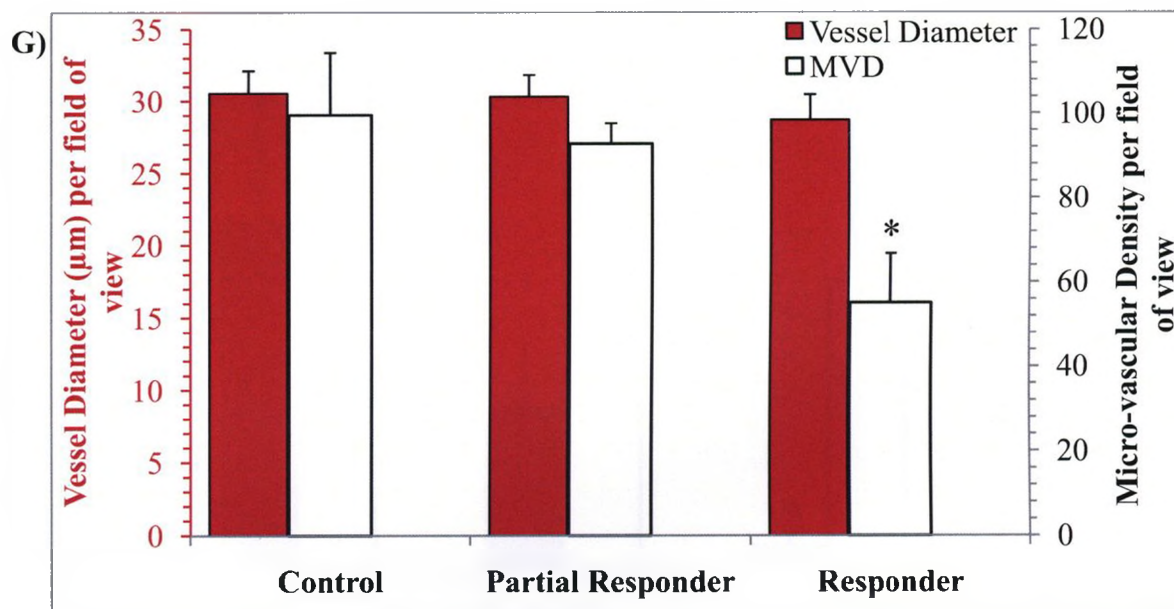
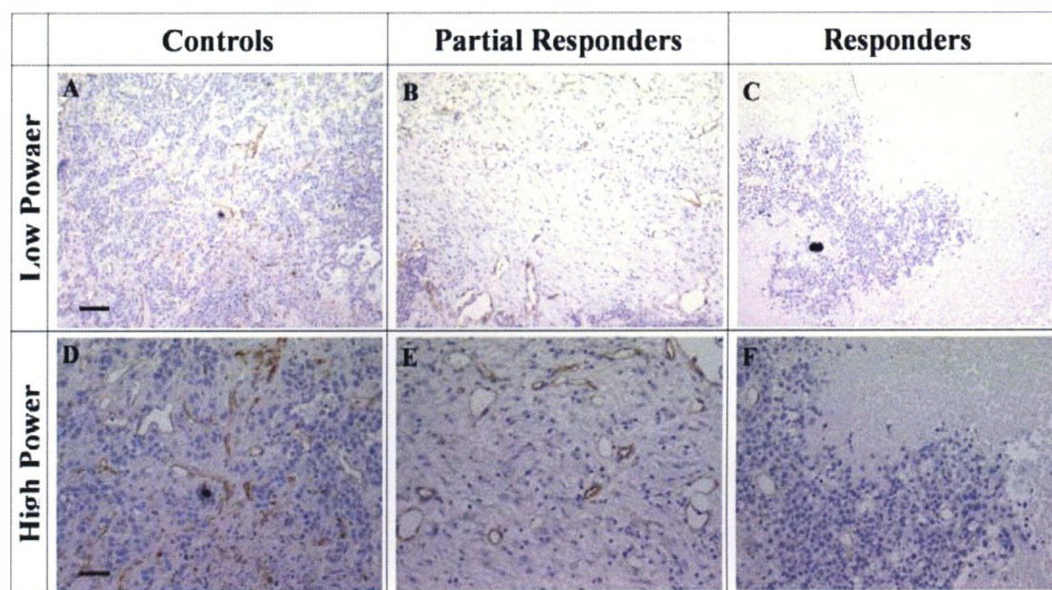
The immunostaining of paraffin sections of the tumor showed abundant α -SMA⁺ cells (light brown stain) within the tumor of all three groups, Figure 4.4 (A) to (F). Separate positive vimentin stain (the dark brown stains that lined vessel lumen) did confirm the presents of pericytes, Figure 4.4 (G) to (L). The pericytes surrounding tumor blood vessels in the control group frequently had irregular shape and extended cytoplasmic processes that were disassociated from the vessel wall and occasionally spread throughout the surrounding tissue. The partial responder group had more pericytes that were associated with blood vessels and showed less abnormal pericytes distribution than in the control group, Figure 4.4. Conversely, the arrangement of pericytes around blood vessels in the responder group resembles those in the normal tissue; with close association between the pericytes and the vessel wall, Figure 4.4 (F) & (L). The images also showed pairing of vessels and clusters or islands of viable tumors cells around the blood vessels, Figure 4.4 (C) & (I). An analysis of the tumor vasculature with CD31 indicates no significant difference in the vessel diameters of the three groups, Figure 4.5. However, the analysis showed a significant reduction in the MVD in the responder group compared to the other groups, $P < 0.05$, Figure 4.5 (G). H&E staining revealed a gradation of hemorrhage area fraction: with the highest amount of hemorrhage in the control, moderate hemorrhage in the partial responder, and mild hemorrhage in the responder group, $P < 0.05$, Figure 4.6. H & E staining also showed a significant increase in tumor cell death (decrease nuclei density), with the least tumor cell death in the control, moderate death in the partial responder and severe death in the responder group, $P < 0.05$, Figure 4.6 (G).

Figure 4.4: Immunohistochemical Staining of Pericytes



Immunohistochemical stains showing the distribution of pericyte on tumor blood vessels. **A) - F)** α -smooth muscle actin (SMA) at low (the bar represents 250 μ m) and high power (the bar represents 50 μ m); the dark brown stain reflects pericytes on and detached from vessels in tumor tissue. The 'arrows' show vessel pairing in the responder group and the 'arrow head' shows transcapillary bridge, both of which are indicative of intussusceptive angiogenesis (27). Also, tumor cells in the responder group developed as distinct clusters or islands of viable cells around the remodeled vessels; the clusters were separated by areas of necrosis. **G) - L)** Matching tissue slices stained with vimentin was used to confirm the presence of pericytes. Both immunostains showed a progressive improvement in the pericyte organization: from loose association in the control, to close association in the responder group.

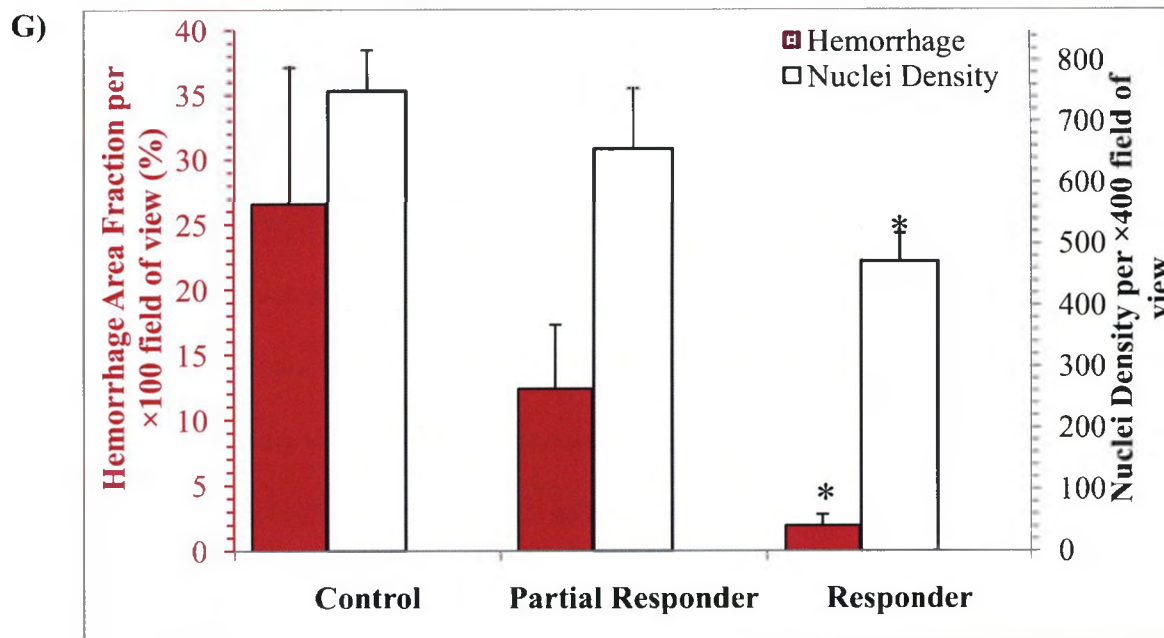
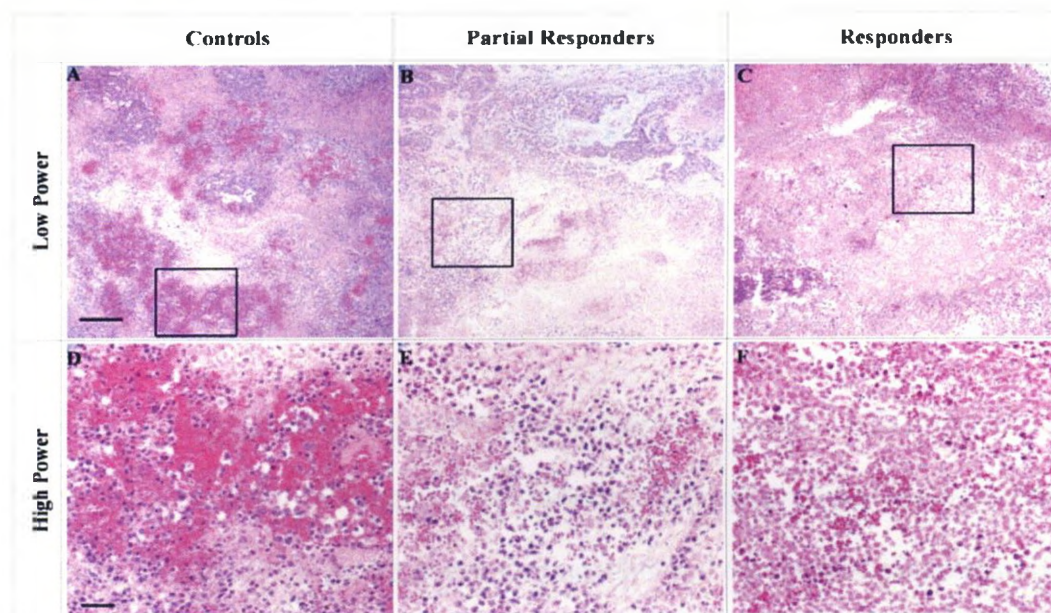
Figure 4.5: Immunohistochemical Staining of CD31 and Vessel Analysis



Immunohistochemical stains for CD31 in the three groups at the end of the study. **A) – C)** Shows vessels at both low power (bar represents 100 µm) and **D) – F)** high power (bar represents 50 µm). The images show numerous irregular shaped vessels in the control and partial responder group, with fewer more circular shaped vessels in the responder group. **G)** Analysis of the vessel diameter and MVD per x200 field of view.

* Mann-Whitney rank test indicates significant difference from the other groups, $P < 0.05$.

Figure 4.6: Hemorrhage Fraction and Nuclei Density in the Hepatic Tumor



The impact of thalidomide on VX2 carcinoma vascular permeability and cell survival was examined using hematoxylin and eosin (H&E) staining. (A) – (C) Histological slides at low power (bar represents 200 μm) in the three groups; hemorrhage was observed predominantly in the control group and progressively less in the partial responder and responder group. (D) – (F) Histological slides at high power (bar represents 50 μm) in the three groups show a progressive reduction in viable tumors cells from high in the control

to a low in the responder group. Each blue dot represents viable tumor cell nuclei. (G) The hemorrhage area fraction per field of view (%) and the nuclei density per field of view in the three groups at the end of the study.

* Mann-Whitney rank test indicates significant difference from the other groups, $P < 0.05$.

4.4 DISCUSSION

The major finding of the present study is that thalidomide, a VEGF and basic fibroblast growth factor inhibitor (21-23) induced differential therapeutic response in implanted VX2 tumors in rabbit livers. Our unpublished data on plasma concentration of thalidomide over the course of treatment showed a concentration of $3.7 \pm 0.6 \mu\text{g}\cdot\text{ml}^{-1}$, which was well within the range of therapeutic levels for thalidomide (28). The CT perfusion data shows that liver tumors treated with thalidomide can respond with decreased (responder) or maintained (partial responder) perfusion. The analysis of tumor perfusion and histology demonstrates a correlation between immediate perfusion reduction and reduction of hematogenous spreading of tumor cells; whereas, maintained perfusion showed no benefits to progression free survival. This is consistent with a recent study in renal cell carcinoma, which indicates that decreased tumor blood flow induced by the VEGF receptor antagonist PTK787/ZK222584 may predict favorable clinical outcome (29). Similarly, El Assal *et al.* demonstrated that tumors with high MVD had a higher incidence of intra-hepatic recurrence than those with low MVD; and that low MVD correlates with metastasis free survival (30). Since decrease in blood flow can lead to hypoxia and treatment resistance (8), it is important to determine the temporal profile

of tumor blood flow response to the administration of angiogenesis inhibitors in the scheduling of adjuvant chemo- or radiation therapy (10-12).

There is no single marker that identifies all pericytes since their receptor expression vary in different organs and with physiological conditions (31). Pericytes in this study were considered present if both α -SMA (microfilaments) and vimentin (intermediate filaments) immunoreactivity were visible around the vessel perimeter. By the end of the thalidomide treatment period in this study, results of immunohistochemical staining suggests improved pericyte coverage of vessels in the responder group and there was a marked reduction in tumor hemorrhage, MVD and lung metastasis. In comparison, detached pericytes from vessels observed in the control and partial responder group may have contributed to the increased tumor hemorrhage and the dissemination of tumor cells to the lungs. Our findings are in agreement with those found in colorectal cancer patients, in whom existence of tumors with immature neovasculation, as indicated by the absence of pericytes, was correlated with increase metastasis and poor prognosis (32).

Abramsson *et al.* showed that tumor vessels are adapted to the recruitment of pericytes and that reduced vessel density from pruning of newly sprouted vessels may lead to enhanced pericyte coverage of the remaining vessels (4). Likewise, in our study the reduction in MVD and perfusion in the responder group suggest that the initial pruning of newly sprouted vessels by thalidomide may have been followed by improved pericyte coverage on the remaining vessels leading to reduction in vessel permeability and hemorrhage shown in the H&E slides of the responder group. The pairing of vessels in the responder group suggests that after the initial vascular pruning the remaining vessels may have continued development through intussusceptive microvascular growth

(IMG). Hlushchuk *et al.* found that tumor vasculature expands predominantly through IMG after the cessation of the VEGF receptor antagonist PTK787/ZK222584 (33). They also demonstrated that the recruitment of α -SMA⁺ cells for intussusception was part of an adaptive angiogenesis mechanism (33).

The mechanism of resistance to anti-angiogenesis treatment or adaptive angiogenesis is poorly understood, but it has been proposed that the angiogenic process has built in redundancies that allow secondary pro-angiogenesis factors to be up-regulated when the primary factors are suppressed (34, 35). Our data suggest that the adaptive angiogenesis mechanism that leads to intussusception may also occur during the thalidomide treatment period. A possible mechanism for the action of thalidomide in the responder group is that the drug may have reduced the availability or production of VEGF, which leads to reduction in tumor perfusion through vascular pruning and the production of secondary pro-angiogenesis compounds such as platelet derive growth factor (PDGF). Huang *et al.* showed that adaptive angiogenesis results in up-regulation of secondary growth factors such as PDGF and ephrinB2, which may lead to recruitment of pericytes, enhanced vascular stability and recurrent tumor growth in response to chronic angiogenesis inhibitor (36). They also showed tumors that survived anti-angiogenic therapy developed as distinct clusters or islands of viable cells surrounding remodeled vessels (36), which is similar to our observations in the responder group, Figure 4.4 (C) & (I).

A literature review identified several reports of differential tumor oxygenation response and disagreement about the efficacy of adjuvant chemo- or radiation therapy with angiogenesis inhibitors (14, 15, 37-39). The disagreement on the efficacy of

combined therapy has been attributed to the timing of adjuvant cytotoxic therapy relative to anti-angiogenesis therapy (18, 19). Our data suggest that the disagreement may also be due to the differential perfusion response induced by the same angiogenesis inhibitor. The implication of this is two-fold, inadequate or inefficient perfusion could lead to poor delivery of drugs to the tumor or the creation of a hypoxic microenvironment resistant to therapy (40). Conversely, vascular normalization with improved perfusion, tissue oxygenation and drug delivery could lead to tumor radio-sensitivity (9). Tong *et al.* showed that VEGF receptor antagonists may improve drug delivery by the induction of vascular normalization, along with improvement in trans-vascular gradients in oncotic and hydrostatic pressure in tumors (38). Moreover, Ebied *et al.* used triple-phase helical CT to show that patients with hypervascular tumors had improved survival after transcatheter arterial chemoembolization (41). Our study showed an improvement in tumor perfusion in the partial responder group relative to the responder group during the first 8 days of therapy; which suggests that this group would more likely benefit from adjuvant chemo- and/or radio-therapy during this period. An inference supported by the finding that tumor blood vessels that are resistant to the VEGF antagonist sunitinib showed improved microvascular diameter, red blood cell velocity, blood flow and delivery of chemotherapy (42).

Conversely, the responder group showed an immediate reduction in tumor perfusion that may lead to hypoxia and poor drug delivery. Jain (19) suggest that maintenance of the balance between pro and anti-angiogenesis factors leads to vascular normalization; whereas, the abundant supply of anti-angiogenesis factors may lead to rapid pruning and inadequate tumor vasculature. Hypoxia is created from the mismatch

between the supply and consumption of oxygen. Vaupel *et al.* showed that restriction of the microcirculation in cancer cells leads to inadequate supply of oxygen, which is aggravated with the increase in tumor size (43). We have previously shown an inverse correlation between tumor H_TBF and glucose metabolic uptake in the VX2 carcinoma model (44). Prolong imbalance between oxygen supply and utilization may lead to hypoxia, therapy resistance and the spread of metastases to distant organs (45). Hence, knowledge of tissue oxygenation or perfusion could be used as a tool to identify which patient would benefit from adjuvant chemo- or radiation therapy with angiogenesis inhibitors. Patients with low blood flow and prolong periods of metastasis free survival after anti-angiogenesis therapy may be more suitable for resection, if operable, rather than adjuvant chemo- or radiotherapy (29, 46).

One of the first clinical evidence of vascular normalization induced by anti-VEGF therapy was first described by Willett *et al.* (46). Their study demonstrates the complex relationship between blood flow, MVD and α -SMA⁺ pericyte coverage during vascular normalization. We have further demonstrated that tumor response to anti-angiogenesis therapy is heterogeneous, even when studying the same inhibitor in the same tumor model; and that CT perfusion with its ability to assess tumor perfusion response may be used to optimize the timing of adjuvant chemo- or radiation therapy.

A limitation of the study is the use of VX2 carcinoma as a model of human HCC in studying the efficacy of thalidomide. The disadvantage with the model is that VX2 carcinoma is of epithelial origin and was developed from a papilloma virus (47). Consequentially, it does not share the same course of development as HCC or the background cirrhosis that usually accompany the disease (48). However, the large size of

rabbits compared to mice models of HCC makes them well suited for non-invasive perfusion imaging using clinical CT scanners. Another limitation is the lack of correlation between the DCE-CT perfusion data and immunohistochemical measurement of MVD and diameter. The difference between the two measurement techniques was due to the nature of the DCE-CT perfusion. DCE-CT perfusion measures only vessels with blood flow, whereas immunohistochemical studies measures the MVD and diameter in all vessels including those that do not have blood flow (49).

4.5 ACKNOWLEDGEMENT

We would like to thank Dr. Zia Khan for his insights on vascular biology and Kelly Galloway-Kay for her assistance with the histological studies.

4.6 REFERENCE

1. Jain RK. Molecular regulation of vessel maturation. *Nat Med* 2003; 9:685-693.
2. Carmeliet P, Jain RK. Angiogenesis in cancer and other diseases. *Nature* 2000; 407:249-257.
3. Bergers G, Benjamin LE. Tumorigenesis and the angiogenic switch. *Nat Rev Cancer* 2003; 3:401-410.
4. Abramsson A, Berlin O, Papayan H, Paulin D, Shani M, Betsholtz C. Analysis of mural cell recruitment to tumor vessels. *Circulation* 2002; 105:112-117.
5. Dinehart SM, Kincannon J, Geronemus R. Hemangiomas: evaluation and treatment. *Dermatol Surg* 2001; 27:475-485.
6. Hellstrom M, Gerhardt H, Kalen M, et al. Lack of pericytes leads to endothelial hyperplasia and abnormal vascular morphogenesis. *J Cell Biol* 2001; 153:543-553.
7. Darland DC, D'Amore PA. Blood vessel maturation: vascular development comes of age. *J Clin Invest* 1999; 103:157-158.
8. Kerbel R, Folkman J. Clinical translation of angiogenesis inhibitors. *Nat Rev Cancer* 2002; 2:727-739.
9. Ansiaux R, Baudelet C, Jordan BF, et al. Thalidomide radiosensitizes tumors through early changes in the tumor microenvironment. *Clin Cancer Res* 2005; 11:743-750.
10. Hurwitz HI, Fehrenbacher L, Hainsworth JD, et al. Bevacizumab in combination with fluorouracil and leucovorin: an active regimen for first-line metastatic colorectal cancer. *J Clin Oncol* 2005; 23:3502-3508.
11. Lee CG, Heijn M, di Tomaso E, et al. Anti-Vascular endothelial growth factor treatment augments tumor radiation response under normoxic or hypoxic conditions. *Cancer Res* 2000; 60:5565-5570.
12. Teicher BA, Holden SA, Ara G, et al. Influence of an anti-angiogenic treatment on 9L gliosarcoma: oxygenation and response to cytotoxic therapy. *Int J Cancer* 1995; 61:732-737.
13. Jain RK. Normalizing tumor vasculature with anti-angiogenic therapy: a new paradigm for combination therapy. *Nat Med* 2001; 7:987-989.
14. Franco M, Man S, Chen L, et al. Targeted anti-vascular endothelial growth factor receptor-2 therapy leads to short-term and long-term impairment of vascular function and increase in tumor hypoxia. *Cancer Res* 2006; 66:3639-3648.

15. Riesterer O, Honer M, Jochum W, Oehler C, Ametamey S, Pruschy M. Ionizing radiation antagonizes tumor hypoxia induced by antiangiogenic treatment. *Clin Cancer Res* 2006; 12:3518-3524.
16. Eberhard A, Kahlert S, Goede V, Hemmerlein B, Plate KH, Augustin HG. Heterogeneity of angiogenesis and blood vessel maturation in human tumors: implications for antiangiogenic tumor therapies. *Cancer Res* 2000; 60:1388-1393.
17. Gee MS, Procopio WN, Makonnen S, Feldman MD, Yeilding NM, Lee WM. Tumor vessel development and maturation impose limits on the effectiveness of anti-vascular therapy. *Am J Pathol* 2003; 162:183-193.
18. Lin MI, Sessa WC. Antiangiogenic therapy: creating a unique "window" of opportunity. *Cancer Cell* 2004; 6:529-531.
19. Jain RK. Normalization of tumor vasculature: an emerging concept in antiangiogenic therapy. *Science* 2005; 307:58-62.
20. Stewart EE, Chen X, Hadway J, Lee TY. Hepatic perfusion in a tumor model using DCE-CT: an accuracy and precision study. *Phys Med Biol* 2008; 53:4249-4267.
21. D'Amato RJ, Loughnan MS, Flynn E, Folkman J. Thalidomide is an inhibitor of angiogenesis. *Proc Natl Acad Sci U S A* 1994; 91:4082-4085.
22. Kruse FE, Jousen AM, Rohrschneider K, Becker MD, Volcker HE. Thalidomide inhibits corneal angiogenesis induced by vascular endothelial growth factor. *Graefes Arch Clin Exp Ophthalmol* 1998; 236:461-466.
23. Patt YZ, Hassan MM, Lozano RD, Ellis LM, Peterson JA, Waugh KA. Durable clinical response of refractory hepatocellular carcinoma to orally administered thalidomide. *Am J Clin Oncol* 2000; 23:319-321.
24. Geschwind JF, Ko YH, Torbenson MS, Magee C, Pedersen PL. Novel therapy for liver cancer: direct intraarterial injection of a potent inhibitor of ATP production. *Cancer Res* 2002; 62:3909-3913.
25. Ko YH, Pedersen PL, Geschwind JF. Glucose catabolism in the rabbit VX2 tumor model for liver cancer: characterization and targeting hexokinase. *Cancer Lett* 2001; 173:83-91.
26. Pauser S, Wagner S, Lippmann M, et al. Evaluation of efficient chemoembolization mixtures by magnetic resonance imaging therapy monitoring: an experimental study on the VX2 tumor in the rabbit liver. *Cancer Res* 1996; 56:1863-1867.

27. Burri PH, Tarek MR. A novel mechanism of capillary growth in the rat pulmonary microcirculation. *Anat Rec* 1990; 228:35-45.
28. Dal Lago L, Richter MF, Cancela AI, et al. Phase II trial and pharmacokinetic study of thalidomide in patients with metastatic colorectal cancer. *Invest New Drugs* 2003; 21:359-366.
29. de Bazelaire C, Alsop DC, George D, et al. Magnetic resonance imaging-measured blood flow change after antiangiogenic therapy with PTK787/ZK 222584 correlates with clinical outcome in metastatic renal cell carcinoma. *Clin Cancer Res* 2008; 14:5548-5554.
30. El Assal ON, Yamanoi A, Soda Y, et al. Clinical significance of microvessel density and vascular endothelial growth factor expression in hepatocellular carcinoma and surrounding liver: possible involvement of vascular endothelial growth factor in the angiogenesis of cirrhotic liver. *Hepatology* 1998; 27:1554-1562.
31. Morikawa S, Baluk P, Kaidoh T, Haskell A, Jain RK, McDonald DM. Abnormalities in pericytes on blood vessels and endothelial sprouts in tumors. *Am J Pathol* 2002; 160:985-1000.
32. Yonenaga Y, Mori A, Onodera H, et al. Absence of smooth muscle actin-positive pericyte coverage of tumor vessels correlates with hematogenous metastasis and prognosis of colorectal cancer patients. *Oncology* 2005; 69:159-166.
33. Hlushchuk R, Riesterer O, Baum O, et al. Tumor recovery by angiogenic switch from sprouting to intussusceptive angiogenesis after treatment with PTK787/ZK222584 or ionizing radiation. *Am J Pathol* 2008; 173:1173-1185.
34. Jubb AM, Oates AJ, Holden S, Koeppen H. Predicting benefit from anti-angiogenic agents in malignancy. *Nat Rev Cancer* 2006; 6:626-635.
35. Zaghoul N, Hernandez SL, Bae JO, et al. Vascular endothelial growth factor blockade rapidly elicits alternative proangiogenic pathways in neuroblastoma. *Int J Oncol* 2009; 34:401-407.
36. Huang J, Soffer SZ, Kim ES, et al. Vascular remodeling marks tumors that recur during chronic suppression of angiogenesis. *Mol Cancer Res* 2004; 2:36-42.
37. Fenton BM, Paoni SF, Ding I. Effect of VEGF receptor-2 antibody on vascular function and oxygenation in spontaneous and transplanted tumors. *Radiother Oncol* 2004; 72:221-230.
38. Tong RT, Boucher Y, Kozin SV, Winkler F, Hicklin DJ, Jain RK. Vascular normalization by vascular endothelial growth factor receptor 2 blockade

induces a pressure gradient across the vasculature and improves drug penetration in tumors. *Cancer Res* 2004; 64:3731-3736.

39. Winkler F, Kozin SV, Tong RT, et al. Kinetics of vascular normalization by VEGFR2 blockade governs brain tumor response to radiation: role of oxygenation, angiopoietin-1, and matrix metalloproteinases. *Cancer Cell* 2004; 6:553-563.
40. Jain RK. The Eugene M. Landis Award Lecture 1996. Delivery of molecular and cellular medicine to solid tumors. *Microcirculation* 1997; 4:1-23.
41. Ebied OM, Federle MP, Carr BI, et al. Evaluation of responses to chemoembolization in patients with unresectable hepatocellular carcinoma. *Cancer* 2003; 97:1042-1050.
42. Czabanka M, Vinci M, Heppner F, Ullrich A, Vajkoczy P. Effects of sunitinib on tumor hemodynamics and delivery of chemotherapy. *Int J Cancer* 2009; 124:1293-1300.
43. Vaupel P, Kallinowski F, Okunieff P. Blood flow, oxygen and nutrient supply, and metabolic microenvironment of human tumors: a review. *Cancer Res* 1989; 49:6449-6465.
44. Stewart EE, Chen X, Hadway J, Lee TY. Correlation between hepatic tumor blood flow and glucose utilization in a rabbit liver tumor model. *Radiology* 2006; 239:740-750.
45. Brizel DM, Scully SP, Harrelson JM, et al. Tumor oxygenation predicts for the likelihood of distant metastases in human soft tissue sarcoma. *Cancer Res* 1996; 56:941-943.
46. Willett CG, Boucher Y, di Tomaso E, et al. Direct evidence that the VEGF-specific antibody bevacizumab has antivascular effects in human rectal cancer. *Nat Med* 2004; 10:145-147.
47. Kidd JG, Rous P. A transplantable rabbit carcinoma originating in a virus - induced papilloma and containing the virus in masked or altered form. *J Exp Med* 1940; 71:813-838.
48. Tsukuma H, Hiyama T, Tanaka S, et al. Risk factors for hepatocellular carcinoma among patients with chronic liver disease. *N Engl J Med* 1993; 328:1797-1801.
49. Kan Z, Phongkitkarun S, Kobayashi S, et al. Functional CT for quantifying tumor perfusion in antiangiogenic therapy in a rat model. *Radiology* 2005; 237:151-158.

CHAPTER 5: CONCLUSION

5.1 THESIS OVERVIEW

The prognosis for hepatocellular carcinoma (HCC) cancer patients is poor due to the late discovery of the tumor. Potential curative liver transplantation is limited to patients with a single HCC smaller than 5 cm or up to three nodules smaller than 3 cm (1). Considerable efforts have been spent in the development of non-invasive imaging tools that can aid in the early diagnosis and treatment evaluation of HCC patients. Chapter 1 presented a summary of the relevant literature pertaining to liver cancer, with an emphasis on HCC. Additionally, it outlined imaging methods for diagnosis, selection of treatment options and emerging concepts such as the involvement of sinusoid capillarization and tumor angiogenesis in HCC vascularity. The progression from cirrhosis to dysplastic nodules and HCC is characterized by abnormal vascularization and by a shift from a venous to an arterial blood supply. Changes in tissue vascularity are believed to manifest as alterations in blood flow, which can be exploited in the development of new diagnostic tools. This thesis describes an *in vivo* method of measuring hepatic blood flow (HBF) using dynamic contrast enhanced computed tomography (DCE-CT) and modeling of the kinetics of contrast distribution in the liver.

The accuracy of hepatic perfusion measured with DCE-CT was validated against the gold standard of radioactive microspheres and the precision was determined by repeated measurements in the same subject and Monte Carlo simulations. Once validated the utility of hepatic perfusion measurements were demonstrated in two sets of experiments: i) first, to show that DCE-CT perfusion can augment the functional imaging capabilities of hybrid positron emission tomography (PET)/CT scanners by providing

perfusion information without the need to have a cyclotron on-site for the production of short-lived radio-isotopes; and, ii) to show that DCE-CT perfusion can be used to evaluate the efficacy of angiogenesis inhibitor therapy.

To summarize the work described in this thesis, the final chapter will highlight the major findings from each experiment, followed by a discussion of their experimental and clinical relevance. The future directions for this research will be discussed in the final section.

5.2 VALIDATION OF DYNAMIC CONTRAST ENHANCED COMPUTED TOMOGRAPHY MEASUREMENT OF HEPATIC PERFUSION

Validation studies were performed in order to justify the use of DCE-CT perfusion measurements in either diagnostic or treatment evaluation of liver cancer patients. Chapter 2 presents an analysis of the accuracy of hepatic perfusion in the liver of rabbits implanted with VX2 carcinoma. To achieve a range in blood flow three arterial partial carbon dioxide tension (P_aCO_2) levels: normo-, hyper- and hypo-capnia were used. The DCE-CT derived hepatic arterial blood flow (H_ABF) measurements were compared against the gold standard of radioactive microspheres. Under normo-capnia the microsphere- H_ABF were: 51.9 ± 4.2 , 40.7 ± 4.9 and 99.7 ± 6.0 $ml \cdot min^{-1} \cdot (100 g)^{-1}$ while DCE-CT- H_ABF were: 50.0 ± 5.7 , 37.1 ± 4.5 and 99.8 ± 6.8 $ml \cdot min^{-1} \cdot (100 g)^{-1}$ in normal tissue, tumor core and rim respectively. The study showed no significant differences between H_ABF measurements obtained with both techniques ($P > 0.05$). Furthermore,

there was a strong correlation between H_A BF values from both techniques with $R^2 = 0.81 \pm 0.05$ ($P < 0.05$).

The precision was determined through repeated measurements in the same rabbit and the use of Monte Carlo simulations. The precision of the DCE-CT H_A BF was determined to have a coefficient of variation of 5.7, 24.9, and 1.4 % in the normal tissue, tumor core and rim respectively.

5.3 RELATIONSHIP BETWEEN HEPATIC TUMOR BLOOD FLOW AND GLUCOSE UTILIZATION

Imbalance between oxygen supply and glucose utilization (metabolic demand) may lead to tumor hypoxia; which in turn, may trigger more aggressive behavior in tumors or compromised therapy. Chapter 3 presents a study designed to test the ability of hybrid PET/CT scanners to determine the relationship between tumor blood flow and glucose utilization. The tumor blood flow was determined using DCE-CT perfusion, while glucose utilization was determined with fluorine-18 fluoro-2-deoxy-D-glucose (FDG) PET. The glucose utilization was estimated by the standardised uptake value (SUV) of FDG. The study demonstrated the ability of DCE-CT perfusion to non-invasively monitor the growth of hepatic tumors and to categorize their pre-vascular and vascular growth phase. It also showed an increase in the tumor's hepatic arterial fraction, which is the fraction of liver blood flow that is supplied by the hepatic artery, from a normal value of 34 ± 5 to 67 ± 10 % in the VX2 tumor at the end of the study. This suggests that the

implanted VX2 carcinoma derived most of its blood from the arterial rather than the portal circulation.

A linear regression analysis showed an inverse correlation between tumor glucose utilization (SUV) and HBF, with an R^2 of 0.727 ($P < 0.05$). The uncoupling between glucose utilization and blood flow suggests limited supply of oxygen (possibly hypoxia) and that the tumor cells were surviving via anaerobic glycolysis. These results suggest that DCE-CT perfusion has the potential to enhance the diagnostic ability of hybrid PET/CT scanners by allowing HBF measurement to be performed without the need of a on-site cyclotron for the production of short lived radiotracers which are used for blood flow measurement.

5.4 THE EFFECT OF THALIDOMIDE ON HEPATIC PERFUSION AND VASCULAR REMODELING

Vascular endothelial growth factor (VEGF) inhibitors such as thalidomide have been shown to prevent the formation of new tumor blood vessels and inhibit tumor growth (2). Recent preclinical studies support the concept of a transient normalization of the tumor vasculature improving perfusion and sensitizing tumor to adjuvant chemo- and radiation therapy during the early stage of treatment (3). Chapter 4 presents a study investigating whether DCE-CT hepatic perfusion measurements can be used to identify vascular normalization. DCE-CT scans were performed to measure hepatic perfusion in implanted VX2 carcinoma tumors. Animals treated with thalidomide were divided in to those that survive for more than 24 days without lung metastasis (responder group), and those that survive for less than 24 (partial responder group). The results suggest that

thalidomide induced a differential perfusion response in the therapy group during the first 8 days after the start of therapy. HBF in the responder group decreased by $40 \pm 12\%$ relative to day 0, $P < 0.05$; whereas, those in the partial responder remained unchanged. Immunohistochemical analyses suggest improved pericyte coverage of vessels in the responder group along with a marked reduction in tumor hemorrhage, MVD and lung metastases.

The study demonstrated that tumor response to thalidomide is heterogeneous, even when studying the same antagonist in the same tumor model. It also suggests that DCE-CT perfusion, with its ability to assess tumor perfusion response, may be used to optimize the timing of adjuvant chemo- or radiation therapy.

5.5 EXPERIMENTAL AND CLINICAL RELEVANCE

5.5.1 Experimental Relevance of VX2 Carcinoma as a Model for Hepatocellular Carcinoma

The studies described in this thesis used a rabbit VX2 carcinoma model of HCC. The animal model allowed for greater control over the experiments, repeated measurements in the same subject and the performance of invasive procedures such as immunohistochemical staining and the invasive microsphere blood flow measurements. VX2 carcinoma cells grown in a donor rabbit were implanted directly into the liver of another rabbit. VX2 carcinoma was first described by Kidd *et al.*, and is believed to have originated from a papilloma virus (4). The tumors are of epithelial cell origin and are extremely metastatic, with high affinity for the lung (5). The VX2 carcinoma model was initially used to test the efficacy of hyperthermia, radiotherapy and later regional

chemotherapy through drug delivery with intra-arterial catheterization for the treatment of liver cancer (6-8). VX2 carcinoma resembles most solid human tumors; it has a rapid growth rate, an ischemic center and well vascularized periphery (5). Moreover, it has been shown that VX2 carcinoma grown in the liver of rabbits had similar vascularity to HCC; with tumor blood vessels arising predominately from the hepatic artery (9, 10). Ko *et al.* showed that VX2 carcinoma tumors had similar glycolytic metabolic properties to human hepatomas (11). The tumors were shown to exhibit a high glycolic and high hexokinase phenotype after implantation and growth in rabbits (11). These similarities in both the metabolic and vascular development have lead to several researcher groups using VX2 carcinoma as a model for HCC (5, 9-11).

The VX2 carcinoma model allowed us to validate our perfusion measurements against the gold standard of radioactive microsphere. The microsphere technique requires the sacrifice of the animal. Results from those experiments are summarized above and demonstrates the validity of our technique. Using DCE-CT perfusion and FDG-PET we were able show a mismatch between the tumor glucose utilization and HBF. This mismatch suggests that there was limited supply of oxygen and that tumor cells were surviving via anaerobic glycolysis. Furthermore, we were able to show that the tumors develop a necrotic core with no glucose uptake by the end of the study.

5.5.2 Limitations of the VX2 Carcinoma Model

One of the major goals of an animal model is that it should display a similar course and microenvironment as those seen in humans. Unfortunately, the VX2 carcinoma model used in this thesis does not recapitulate all the features of HCC; it lacks

the background hepatitis infection and consequent cirrhosis that usually accompany the disease. More than 80% of patients with HCC have infection with either hepatitis B (HBV) or C (HCV) virus or both (12). HBV and HCV infection leads to the development of liver cirrhosis, which is present in about 80 – 90% of autopsied HCC patients (13). Recently, several transgenic mouse models have been developed that involved an integrated HBV DNA fragment coding for the HBV large envelope polypeptides on a C57BL/6 genetic background (14). Other researchers use the injection of HBV DNA containing the HBx gene into single-cell embryos from CD1-mice (15). Another model generates transgenic mice that carried the HCV core gene (16). Similarly, Murakami *et al.* combined two transgenic mice model for HCC, the c-myc and TGF- α model into a rapid progressing double transgenic model that develops HCC from preneoplastic focal lesions within 8 months (17). However, unlike VX2 carcinoma which grows within three weeks after implantation, the HCC developed in the transgenic model begins to emerge 8 to 16 months after birth (14-16). Another drawback to the use of these mouse models is the relative size of the mouse compared to humans. Mice are about 2500 times smaller than humans, whereas rabbits are only 20 times smaller. Smaller animal would require a higher spatial resolution CT scanner to resolve the aorta and the portal vein required for the kinetic analysis of the liver time-enhancement curves. The protocol of DCE-CT perfusion scans done on rabbits with a clinical CT scanner are much easier to translate to patients than from studies on mice using a dedicated small animal CT scanner.

5.5.3 Clinical Relevance of Dynamic Contrast Enhanced Computed Tomography Perfusion

The DCE-CT perfusion technique described in the thesis was specifically designed for *in vivo* non-invasive measurement of hepatic perfusion. The measurement of hepatic perfusion is clinically relevant for several reasons, the most important of which is the non-invasive ability to get perfusion information that reflects: the delivery of oxygen, nutrients to hepatic tissue, and density of functioning blood vessels. Another implication of DCE-CT perfusion is that the technique is ideally suited for combination with other diagnostic methods such as conventional CT and hybrid PET/CT scanning. Conventional CT scanning is now the most commonly used imaging modality in diagnosing HCC in the United States (18). The addition of DCE-CT will have very little impact on patient preparation and setup. The added perfusion scan is inexpensive, non-invasive except for intravenous injection of contrast, and permits both perfusion and anatomical information of liver tumors or disease to be obtained in the same examination. DCE-CT technique also has the potential to enhance the diagnostic ability of hybrid PET/CT scanners by allowing perfusion measurement to be performed without the need of a on-site cyclotron for the production of short lived radiotracers which are used for blood flow measurement.

As mentioned, DCE-CT perfusion technique is accurate, validated against the gold standard of radioactive microsphere and is highly precise as determined with repeated measurements on the same subject and Monte Carlo simulations. The accuracy of the technique suggests that DCE-CT perfusion can be used to monitor the blood supply of HCC as it shifts from the portal vein to the hepatic artery (i.e. increase in H_ABF). Blood flow monitoring would be ideal for diagnosing patients with HCC, monitoring the

response to therapy and monitoring the progress of patients who are waiting for liver transplant or resection. Moreover, this thesis demonstrates that DCE-CT perfusion can be used to determine the efficacy of treatment with anti-angiogenesis drugs. The results showed that identifying the time window during which tumor blood vessels become normalized could be meaningful in optimizing treatment with anti-angiogenesis drugs and adjuvant chemo- or radiation therapy.

5.6 FUTURE WORK

This thesis has demonstrated the accuracy and precision of a new DCE-CT perfusion technique to measure hepatic blood flow along with other physiological measurements. It has also suggested a number of experiments which may benefit a wide variety of patient with HCC or other hepatic diseases. The following subsections outlined potential new directions of research.

5.6.1 Optimizing Angiogenesis Inhibitor Therapy and Adjuvant Radiotherapy

In Chapter 4 we demonstrated the ability of DCE-CT perfusion to identify animals that may benefit from combined angiogenesis inhibitor therapy and adjuvant radiotherapy. The results showed a differential perfusion response to the VEGF antagonist thalidomide. Animals in the responder group showed a reduction in vessel density and hepatic perfusion; while, animals in the partial responder group showed a transient normalization of tumor vasculature, along with improved hepatic perfusion. The improvement in hepatic perfusion may lead to improve drug delivery, trans-vascular gradients in oncotic and hydrostatic pressure and possibly improve delivery of oxygen to

the tumor. These improvements may have potentiated the tumor for the induction of cytotoxic cancer therapies such as chemo- and radiotherapy. To test this hypothesis another study need to be performed that uses DCE-CT perfusion to select animals that has improved perfusion after angiogenesis inhibitor therapy for the administration of either chemo or radiotherapy and evaluate whether the outcome is better than just anti-angiogenesis, chemo- or radio-therapy.

Other studies using a variety of VEGF inhibitors have shown disparate results about the efficacy of adjuvant chemo- or radiation therapy (19-23). The disagreement may be due to the differential perfusion response to angiogenesis inhibitors, hence non-invasive measurement of perfusion or oxygen level is required. It would be beneficial to retest these drugs while monitoring the tumor perfusion to determine which drug would elicit the vascular normalization effect.

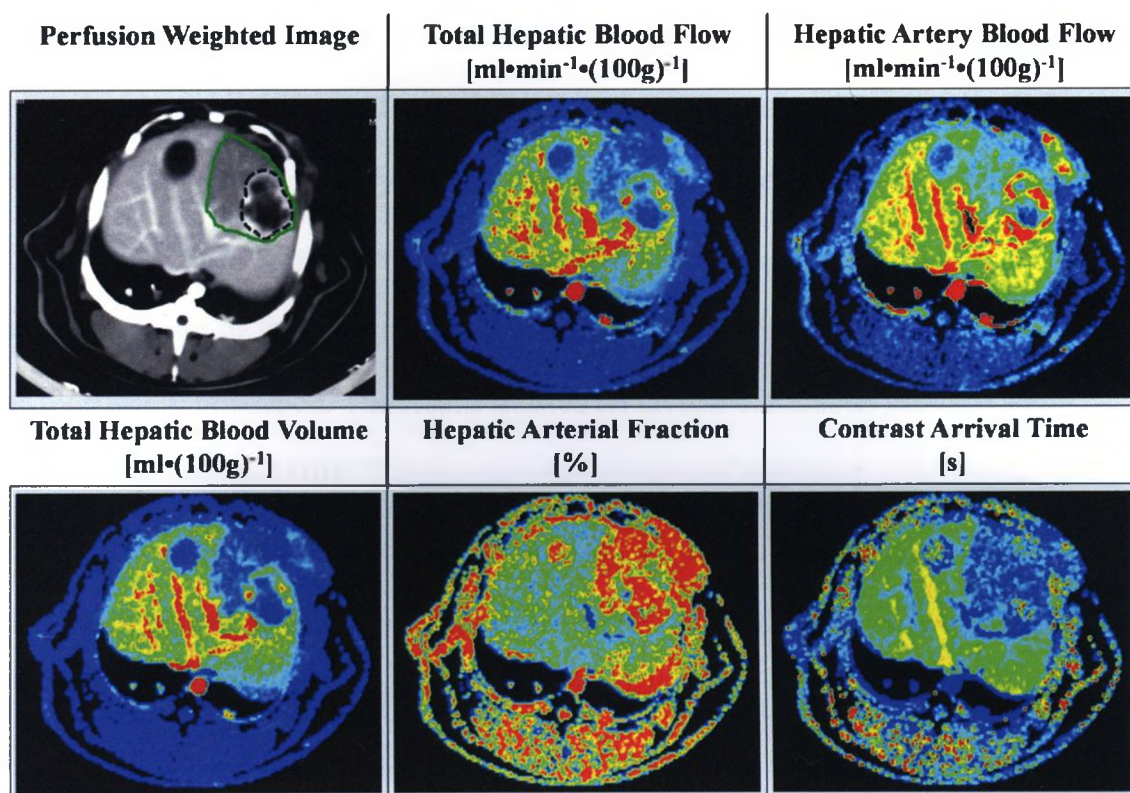
5.6.2 Evaluating Radiation Therapy of Hepatocellular Carcinoma

Historically, radiation therapy has not played a significant role in the treatment of liver cancer, because of the liver's low tolerance to radiation and the frequent development of radiation-induced liver disease (RILD) following irradiation. RILD results from radiation damage to the hepatic vascular system and the pathology includes veno-occlusive disease, which is characterized by thrombosis within the central veins of the liver producing portal hypertension (24). Portal hypertension is a leading predictor of poor outcome following RILD. RILD may affect the entire liver (rarely), a lobe, or a fraction of a lobe. The clinical outcome from RILD ranges from mild, reversible damage to death. The risk of developing RILD is greater than 5% for uniform whole-liver

radiation therapy of 28 to 35 gray (Gy) delivered over 3 weeks (24). Unfortunately, radiation doses greater than 35 Gy are required for effective radiotherapy.

Technological advances, such as intensity modulated radiation therapy (IMRT) and conformal radiation therapy (CRT) have provided the means to deliver high radiation dose that highly conforms to the tumor and avoid critical normal tissue. With IMRT the radiation is delivered with multiple small fields within each beam, producing a modulated fluence pattern for each beam angle. With CRT multiple fields from different angles and different beam weight are used to treat the tumor. In IMRT and CRT individualized treatment for a patient is planned from anatomical CT or magnetic resonance images. Unfortunately, anatomical images provide limited information about the physiological state of the liver and tumor. Cao *et al.* showed that knowledge of the hepatic venous flow can be used to predict radiation induce dysfunction and can be used to optimize the delivery high dose to the tumor, while avoiding RILD (25). In preliminary experiments we have shown that DCE-CT perfusion can be used to measure the severity of portal hypertension in the VX2 carcinoma model, Figure 5.1. Portal hypertension in a single lobe occurred from the growth of the tumor in close proximity to the portal vessels. As the tumor grew the pressure on the vessels caused the vessel to collapse, which led to a reduction in HBF and hepatic blood volume (HBV) in the lobe containing the tumor, Figure 5.1. However, our results showed that H_A BF in the lobe was diminished to a much less extent relative to normal tissue than HBF, which suggests that the involved hepatic tissue may remain viable, Figure 5.1.

Figure 5.1: Measurement of Portal Hypertension with DCE-CT Perfusion



Preliminary result which shows that DCE-CT perfusion can quantify liver function during portal hypertension. Regions of interest (ROIs) were drawn on the perfusion weighted image to outline the tumor (dotted in black); while another ROI was drawn to outline (green) the lobe experiencing portal hypertension. HBF and HBV were lower in the affected lobe, while H_ABF was maintained. The increase in hepatic arterial fraction in the affected lobe suggested the reduction of portal venous blood flow and the maintenance of H_ABF close to the normal level. The contrast arrival time map shows that the affected lobe was supplied mainly by the hepatic artery, which normally supplies about 50% of the oxygen need by the liver. The maintenance of the H_ABF close to the normal level suggested that the affected lobe may be viable.

5.6.3 Relationship between Hepatic Arterial Blood Flow and Glucose Utilization

Tumor cells that have low levels of oxygen (hypoxic) have been known to exhibit strong resistance to the effects of ionizing radiation (26). Studies have shown that

hypoxia varies heterogeneously between tumors, even amongst those indistinguishable by the clinical classification such as stage, grade and histology (27). It is therefore important to develop a reliable method of measuring oxygen levels or a substitute marker in human tumors, so that the effects of hypoxia on the radio-sensitivity of tumors can be evaluated in order to design more effective treatment. In chapter 3, we attempted to develop such a substitute marker by determining the relationship between the total hepatic blood flow and the glucose utilization. The results showed an inverse correlation between tumor glucose utilization and HBF. The inverse relationship was attributed to the limited supply of oxygen and that the tumor cells were surviving via anaerobic glycolysis. However, Fujita *et al.* demonstrated that a decrease in the rate of oxygen delivery to the normal liver correlates more with a reduction in H_ABF but not HBF, which remained unchanged (28). This suggests that the measurement of H_ABF is a more reliable predictor of hepatic oxygenation than HBF. Moreover, as we and others have demonstrated, hepatic tumors derive a higher portion of its new blood vessels (through angiogenesis) from the hepatic artery rather than from the portal vein. This suggests that the inverse correlation shown between HBF and glucose utilization in chapter 3 may not fully reflect the relationship between oxygen supply and demand in the tumor. To address these concerns a series of experiments is required to compare the relationship between HBF, H_ABF and glucose utilization. Also, direct measurement of tissue oxygenation, for example, by a Eppendorf pO_2 needle probe, is required to determine if the relationship between blood flow (HBF or H_ABF) and SUV could be used a predictor of tumor hypoxia (low tissue oxygen concentration).

5.7 REFERENCES

1. Mazzaferro V, Regalia E, Doci R, et al. Liver transplantation for the treatment of small hepatocellular carcinomas in patients with cirrhosis. *N Engl J Med* 1996; 334:693-699.
2. D'Amato RJ, Loughnan MS, Flynn E, Folkman J. Thalidomide is an inhibitor of angiogenesis. *Proc Natl Acad Sci U S A* 1994; 91:4082-4085.
3. Ansiaux R, Baudelet C, Jordan BF, et al. Thalidomide radiosensitizes tumors through early changes in the tumor microenvironment. *Clin Cancer Res* 2005; 11:743-750.
4. Kidd JG, Rous P. A transplantable rabbit carcinoma originating in a virus - induced papilloma and containing the virus in masked or altered form. *J Exp Med* 1940; 71:813-838.
5. Geschwind JF, Ko YH, Torbenson MS, Magee C, Pedersen PL. Novel therapy for liver cancer: direct intraarterial injection of a potent inhibitor of ATP production. *Cancer Res* 2002; 62:3909-3913.
6. Bookstein JJ. Thermotherapy of VX2 rabbit carcinoma. I. Augmentation by irradiation. *Radiat Res* 1983; 93:395-405.
7. Burgener FA, Barbaric ZL. Treatment of VX2 carcinomas in rabbits by percutaneous intratumoral injection of heated 0.9% NaCl solutions. *Cancer Res* 1979; 39:3429-3434.
8. Davidson T, Wallace J, Carnochan P. The rabbit as an experimental model for regional chemotherapy. 1. Intra-arterial hindlimb infusion. *Lab Anim* 1986; 20:343-346.
9. Geschwind JF, Artemov D, Abraham S, et al. Chemoembolization of liver tumor in a rabbit model: assessment of tumor cell death with diffusion-weighted MR imaging and histologic analysis. *J Vasc Interv Radiol* 2000; 11:1245-1255.
10. Pauser S, Wagner S, Lippmann M, et al. Evaluation of efficient chemoembolization mixtures by magnetic resonance imaging therapy monitoring: an experimental study on the VX2 tumor in the rabbit liver. *Cancer Res* 1996; 56:1863-1867.
11. Ko YH, Pedersen PL, Geschwind JF. Glucose catabolism in the rabbit VX2 tumor model for liver cancer: characterization and targeting hexokinase. *Cancer Lett* 2001; 173:83-91.
12. Parkin DM. The global health burden of infection-associated cancers in the year 2002. *Int J Cancer* 2006; 118:3030-3044.

13. Fattovich G, Stroffolini T, Zagni I, Donato F. Hepatocellular carcinoma in cirrhosis: incidence and risk factors. *Gastroenterology* 2004; 127:S35-S50.
14. Chisari FV, Klopchin K, Moriyama T, et al. Molecular pathogenesis of hepatocellular carcinoma in hepatitis B virus transgenic mice. *Cell* 1989; 59:1145-1156.
15. Reifenberg K, Lohler J, Pudollek HP, et al. Long-term expression of the hepatitis B virus core-e- and X-proteins does not cause pathologic changes in transgenic mice. *J Hepatol* 1997; 26:119-130.
16. Moriya K, Yotsuyanagi H, Shintani Y, et al. Hepatitis C virus core protein induces hepatic steatosis in transgenic mice. *J Gen Virol* 1997; 78 (Pt 7):1527-1531.
17. Murakami H, Sanderson ND, Nagy P, Marino PA, Merlino G, Thorgeirsson SS. Transgenic mouse model for synergistic effects of nuclear oncogenes and growth factors in tumorigenesis: interaction of c-myc and transforming growth factor alpha in hepatic oncogenesis. *Cancer Res* 1993; 53:1719-1723.
18. Bhosale P, Szklaruk J, Silverman PM. Current staging of hepatocellular carcinoma: imaging implications. *Cancer Imaging* 2006; 6:83-94.
19. Fenton BM, Paoni SF, Ding I. Effect of VEGF receptor-2 antibody on vascular function and oxygenation in spontaneous and transplanted tumors. *Radiother Oncol* 2004; 72:221-230.
20. Franco M, Man S, Chen L, et al. Targeted anti-vascular endothelial growth factor receptor-2 therapy leads to short-term and long-term impairment of vascular function and increase in tumor hypoxia. *Cancer Res* 2006; 66:3639-3648.
21. Riesterer O, Honer M, Jochum W, Oehler C, Ametamey S, Pruschy M. Ionizing radiation antagonizes tumor hypoxia induced by antiangiogenic treatment. *Clin Cancer Res* 2006; 12:3518-3524.
22. Tong RT, Boucher Y, Kozin SV, Winkler F, Hicklin DJ, Jain RK. Vascular normalization by vascular endothelial growth factor receptor 2 blockade induces a pressure gradient across the vasculature and improves drug penetration in tumors. *Cancer Res* 2004; 64:3731-3736.
23. Winkler F, Kozin SV, Tong RT, et al. Kinetics of vascular normalization by VEGFR2 blockade governs brain tumor response to radiation: role of oxygenation, angiopoietin-1, and matrix metalloproteinases. *Cancer Cell* 2004; 6:553-563.
24. Lawrence TS, Robertson JM, Anscher MS, Jirtle RL, Ensminger WD, Fajardo LF. Hepatic toxicity resulting from cancer treatment. *Int J Radiat Oncol Biol Phys* 1995; 31:1237-1248.

25. Cao Y, Platt JF, Francis IR, et al. The prediction of radiation-induced liver dysfunction using a local dose and regional venous perfusion model. *Med Phys* 2007; 34:604-612.
26. Hockel M, Schlenger K, Mitze M, Schaffer U, Vaupel P. Hypoxia and Radiation Response in Human Tumors. *Semin Radiat Oncol* 1996; 6:3-9.
27. Hockel M, Vaupel P. Tumor hypoxia: definitions and current clinical, biologic, and molecular aspects. *J Natl Cancer Inst* 2001; 93:266-276.
28. Fujita Y, Sakai T, Ohsumi A, Takaori M. Effects of hypocapnia and hypercapnia on splanchnic circulation and hepatic function in the beagle. *Anesth Analg* 1989; 69:152-157.

APPENDIX A



Oct. 3, 2006

This is the Original Approval for this protocol
 A Full Protocol submission will be required in 2010

Dear Dr. Lee:

Your Animal Use Protocol form entitled:
 CT Perfusion as a Method for Monitoring the Growth of Liver Tumors
 Funding Agency Internal Funding

has been approved by the University Council on Animal Care. This approval is valid from **Oct. 3, 2006 to Oct. 31, 2007**. The protocol number for this project is 2006-078-10 and replaces 2002-079-07.

1. This number must be indicated when ordering animals for this project.
2. Animals for other projects may not be ordered under this number.
3. If no number appears please contact this office when grant approval is received.
 If the application for funding is not successful and you wish to proceed with the project, request that an internal scientific peer review be performed by the Animal Use Subcommittee office.
4. Purchases of animals other than through this system must be cleared through the ACVS office. Health certificates will be required.

ANIMALS APPROVED FOR 1 YR.

Species	Strain	Other Detail	Pain Level	Animal # Total for 1 Year
Rabbit	NZW SPF	2.5-3.0 kg Male	D	30

STANDARD OPERATING PROCEDURES

Procedures in this protocol should be carried out according to the following SOPs. Please contact the Animal Use Subcommittee office (661-2111 ext. 86770) in case of difficulties or if you require copies.

SOP's are also available at <http://www.uwo.ca/animal/acvs>

310 Holding Period Post-Admission

320 Euthanasia

321 Criteria for Early Euthanasia/Rodents

332 Post-Operative/Post-Anaesthetic Care-L2

360 Blood Collection/Volumes/Multiple Species

REQUIREMENTS/COMMENTS

Please ensure that individual(s) performing procedures on live animals, as described in this protocol, are familiar with the contents of this document.

c.c. Approved Protocol - T. Lee, J. Hadway, D. Forder
 Approval Letter - J. Hadway, D. Forder

APPENDIX B

B.1 TRACER KINETIC MODELING

Liver perfusion maps were calculated by means of the tracer kinetic model first described by Johnson and Wilson (1). St Lawrence and Lee derived the adiabatic approximation solution which simplifies the calculation of perfusion maps for the liver (2). Since capillaries in the liver are permeable to contrast, the model divides the liver into two principal spaces; the intravascular space (IVS) and the extra-vascular space (EVS), which are separated by the permeable capillary endothelium (1). The model uses three basic assumptions to arrive at a solution. First, the permeable capillary endothelium allows bidirectional diffusion of contrast between EVS and IVS. Second, in the capillaries there is an axial concentration gradient of contrast but the radial concentration gradient is assumed to be negligible. Third, within the EVS the tracer concentration is assumed to have a homogeneous spatial distribution (i.e. EVS is a compartment). The adiabatic approximation, as discussed by St. Lawrence and Lee (2), assumes that the EVS contrast concentration is changing slowly (i.e. in a quasi-steady state) relative to the rate of change of concentration in the IVS (capillaries). Using the adiabatic approximation, the impulse residue function (2), $H(t)$, can be represented simply as:

$$H(t) = \begin{cases} 1 & | 0 \leq t \leq T_c \\ Ee^{-k(t-T_c)} & | t > T_c \end{cases} \quad (\text{B.1})$$

where T_c is the capillary transit time, k is the rate constant of the washout of contrast from the liver parenchyma or tumor and E is the extraction fraction (3) of contrast by the liver.

E is related to the capillary permeability surface area product (PS) and blood flow (F) of liver sinusoids via the following equation (3):

$$E = 1 - e^{-\left(\frac{PS}{F}\right)} \quad (\text{B.2})$$

The liver has a dual blood supply, one from the hepatic artery and the other from the portal vein. However, the use of the hepatic artery as a viable input is limited, because of its close proximity to the portal vein. The high contrast concentration in the portal vein leads to beam hardening artefacts which can affect the contrast enhancement curve from the hepatic artery (4). Also, the relatively small size of the hepatic artery may result in partial volume averaging and the underestimation of contrast enhancement in the hepatic artery (5). To a close approximation, the enhancement of the aorta can represent that of the hepatic artery input. Therefore, I (t) can be expressed as:

$$I(t) = \alpha A(t) + (1 - \alpha)V(t) \quad (\text{B.3})$$

where A (t) and V (t) are the contrast concentration (enhancement) in the hepatic artery (i.e. the aorta) and the portal vein respectively and α is the fraction of liver blood flow contributed by the hepatic artery.

If the concentration (enhancement) of contrast input to the liver, I(t), is known, then the measured liver parenchymal time enhancement curve, Q (t), can be calculated as the convolution of I (t) and H (t):

$$\begin{aligned} Q(t) &= F \cdot I(t - T_0) * H(t) \\ &= F \cdot I(t) * H(t - T_0) \end{aligned} \quad (\text{B.4})$$

where * is the convolution operator, F is $H_T \text{BF}$ and T_0 is the start time of the liver parenchyma time enhancement curve relative to that of $I(t)$.

The validity of equation (B.4) assumes that liver blood flow is constant and $Q(t)$ is linear with respect to $I(t)$. With $A(t)$ and $V(t)$ measured, the estimated values of α (eq. B.3), F (eq. B.4), E , T_c and k (eq. B.1) are changed iteratively in the deconvolution process to achieve an optimum fit by (eq. B.4) to the measured parenchymal time enhancement curve.

B.2 REFERENCES

1. Johnson JA, Wilson TA. A model for capillary exchange. *Am J Physiol* 1966; 210:1299-1303.
2. St Lawrence KS, Lee TY. An adiabatic approximation to the tissue homogeneity model for water exchange in the brain: I. Theoretical derivation. *J Cereb Blood Flow Metab* 1998; 18:1365-1377.
3. Crone C. The Permeability of Capillaries in various Organs as determined by use of the 'indicator diffusion' Method. *Acta Physiol Scand* 1963; 58:292-305.
4. Joseph PM, Ruth C. A method for simultaneous correction of spectrum hardening artifacts in CT images containing both bone and iodine. *Med Phys* 1997; 24:1629-1634.
5. Cenic A, Nabavi DG, Craen RA, Gelb AW, Lee TY. Dynamic CT measurement of cerebral blood flow: a validation study. *AJNR Am J Neuroradiol* 1999; 20:63-73.